Modelling, Design Optimization, and Experimental Characterization of Miniaturized Pneumatic Artificial Muscles

Shakila Zabihollah

A Thesis

In

The Department

Of

Mechanical, Industrial and Aerospace Engineering

Presented in Partial Fulfillment of the Requirements for The Degree of

Master of Mechanical Engineering

Concordia University

Montreal, Quebec, Canada

August 2023

CONCORDIA UNIVERSITY

School of Graduate Studies

This is to certify that the thesis prepared

By: Shakila Zabihollah

Entitled: Modelling, Design Optimization, and Experimental Characterization of Miniaturized Pneumatic Artificial Muscles

and submitted in partial fulfillment of the requirements for the degree of

Master of Mechanical Engineering

complies with the regulations of the University and meets the accepted standards with respect to originality and quality.

Signed by the final examining committee:

_____ Chair

Dr. Farjad Shadmehri

_____ Examiner

Dr. Farjad Shadmehri

_____ Examiner

Dr. Khaled. E. Galal

_____ Thesis Supervisor

Dr. Ramin Sedaghati

Approved by _____

Dr. Sivakumar Narayanswamy, Graduate Program Director

_____

Dr. Mourad Debbabi, Dean
Gina Cody School of Engineering and Computer Science

ABSTRACT

Modelling, Design Optimization, and Experimental Characterization of Miniaturized Pneumatic Artificial Muscles By

Shakila Zabihollah

Miniaturized pneumatic artificial muscles (MPAMs) are actuators designed to replicate the actuation behaviour of natural muscles. Their unique characteristics, including a high power-to-weight ratio, flexibility, compatibility with the human environment, and compact size, make them widely used in diverse applications. However, MPAMs face a significant challenge in terms of their low force output, which hinders their overall performance. Enhancing their force generation capability while maintaining their compact dimensions is crucial for improving their efficiency.

The present thesis focuses on the design optimization, fabrication, and modelling of an MPAM to maximize its force output while ensuring compatibility with small-scale applications. To this end, a formal design optimization problem is formulated to determine the optimal sizes of MPAMs, with the objective of maximizing their blocked force under geometrical constraints. A comprehensive force model is derived, considering key parameters that influence the response behaviour of MPAMs, which serves as the objective function for maximization. To investigate the importance of various correction terms added to the simple force model of the MPAMs, two optimization formulations varying in their objective functions and vectors of design variables have been defined. One formulation considers the effects of energy stored in the braided sleeving and optimizes the parameters related to braid strands, while the other excludes these factors. To identify the optimal design, a hybrid optimization algorithm is employed, combining a stochastic-based algorithm with gradient-based algorithms. This approach allows for the identification of the global optimum while also examining the effects of different optimization algorithms on the results.

Next, two MPAMs are fabricated using the dimensions obtained from the optimization procedure. The first sample utilizes Ecoflex-50 as the bladder material, while the second sample incorporates a mixture of PDMS and Ecoflex-30. The aim is to compare the performance of the MPAMs

fabricated with different materials for their bladders. An experimental setup is subsequently designed to conduct quasi-static tests on each sample to measure their generated blocked force and contraction under various pressures as well as validate the theoretical results obtained from the optimization process.

Finally, the hysteresis loops obtained from loading and unloading each sample under specific pressures are analyzed to derive correction terms that account for the nonlinear behaviour of MPAMs and the friction between their components. Different theoretical and empirical approaches are assessed to determine the most accurate correction terms. The resulting force model enables accurate predictions of force and contraction outputs under various inlet pressures.

Overall, this study contributes significantly to the design optimization of MPAMs, offering potential applications in diverse fields, including soft robotics and medical devices. The combination of theoretical modelling, optimization techniques, fabrication, and experimental tests provides essential guide for the comprehensive understanding of MPAM's performance and its potential for practical implementation.

Acknowledgments

I would like to begin by expressing my sincere gratitude and appreciation to my supervisor, Professor Ramin Sedaghati. His unwavering support, patience, and exceptional guidance have been invaluable throughout my research journey. I am truly grateful for the opportunity to join his research team and for the vast knowledge and skills I have gained under his diligent supervision.

I would also like to extend my gratitude to Seyed Alireza Moezi for his invaluable suggestions and collaborative efforts in conducting the experiments.

My deepest gratitude goes to my parents, whose endless support and unwavering belief in my abilities have served as an unyielding pillar of strength during the challenges I faced. Their constant encouragement and inspiration have been instrumental in shaping my academic and professional life.

In addition, I would like to extend a special thanks to my uncle, Dr. Abolghassem Zabihollah, for his invaluable suggestions and guidance in both my academic and personal life. His wealth of knowledge and wisdom have been a constant source of inspiration for me.

Lastly, I would like to express my profound appreciation to my close friends, particularly Sina Safaee Sadegh and AmirReza Pasaeian, for their support and friendship.

Table of contents

List of Figures

List of Tables

Nomenclature

α_0	Initial braid angle, (°)
α	Instantaneous braid angle, (°)
γ	Contraction ratio
ε	Strain
v_s	Poisson's ratio of the braid strands
σ	Stress, $(\frac{\mathrm{N}}{\mathrm{m}^2})$
A_{bl}	Area of the bladder, (m^2)
A_{br}	Cross-sectional area of one braid strand, (m^2)
B	Length of one braid strand before being woven around the bladder, (m)
D_0	Initial outer diameter of the bladder, (m)
D	Instantaneous outer diameter of the bladder, (m)
E_{br}	Young's modulus of the braided sleeving, (Pa)
E_k	Modulus of elasticity, (Pa)
F	Force, (N)
F_b	Blocked force, (N)
F_{th}	Theoretical force, (N)
f_s	Friction coefficient between the braid strands
f_{s-bl}	Friction coefficient between the braid strands and the bladder
K_f	Empirical friction factor
L_0	Initial length of the bladder, (m)
L	Instantaneous length of the bladder, (m)
N	Number of turns the braid strand makes from one end of the bladder to the other end
n	Number of braid strands in a braided sleeving

P	Inlet pressure, (Pa)
P_{DB}	Dead-band pressure, (Pa)
R_0	Initial outer radius of the bladder, (m)
R	Instantaneous outer radius of the bladder, (m)
R_{br}	Radius of one braid strand, (m)
$S_{contact}$	Contact area between the braid strands and the bladder, (m^2)
T	Tension, (N)
t_0	Initial thickness of the bladder, (m)
t	Instantaneous thickness of the bladder, (m)
U	Potential Energy, (J)
V	Velocity of the MPAM, (m^2)
V_{br}	Volume of one braid strand, (m^3)
V_{bl}	Volume of the bladder, (m^3)

Chapter 1: Introduction, Literature Review, and Objectives

1.1 Introduction

Actuators, serving as mechanisms to convert energy from diverse sources into mechanical motion, are vital components in all robotic systems. The rapid progress in robotics has expanded its application areas to encompass human welfare, medical services, entertainment, and agriculture [1]. Surgical robots, in particular, operate in dynamic and unpredictable environments where contact stability is essential. As a result, these state-of-the-art robotic systems necessitate actuation systems that are safe, reliable, self-repairing, bonding, and physically flexible. Moreover, there is a growing demand for small-scale mechanical systems in robotic applications, requiring compact, lightweight, and power-efficient actuators capable of generating significant forces and strains while fitting within miniaturized systems [2].

Conventional actuators like electric motors exhibit limitations, including safety concerns, high costs, friction losses, impedance mismatch, and design complexity when applied to millimeter-scale designs. Hence, there is a need for novel actuators that can emulate organic characteristics, securely interact with humans, regulate conformity, and tolerate rotational or lateral misalignments while still preserving the advantages of traditional engineering actuators (i.e. high power-to-weight ratio, high force-to-weight ratio, and good positional and force control) [3]. One promising type of actuator meeting these requirements is the pneumatic artificial muscle (PAM), which replaces the cylinder/piston structure with a compliant braided shell drive while maintaining excellent power-to-weight performance and simplicity [1]. PAMs are designed to closely mimic the actuation behaviour of natural muscles, which are biological actuators with remarkable driving power. Different types of PAMs have emerged based on distinct design principles and applications, which can be categorized into four primary groups: braided muscles (also known as McKibben muscles), pleated muscles, netted muscles, and embedded muscles [4].

The earliest example of a braided pneumatic actuator can be traced back to Pierce's patent application in 1936 [5-6], employed in the coal mining business as an alternative to dynamite. When the air was supplied to the device, the expansion in diameter and the radial expansion of the cover exerted force on the coal. In 1949, De Haven [7] invented a device comprising a double

helically woven tube with an inflatable inner tube, capable of generating a maximum force of approximately 7 kN and contracting by 30% when pressurized to 3 MPa. By 1958, Gaylord [8] had patented an externally powered "Fluid Actuated Motor System and Stroking Device". He also performed a mathematical analysis of the system and presented the first equations describing the force produced by PAMs. Schulte [9] published an article outlining the applications and mathematical analysis of PAMs, while Joseph McKibben [10] suggested using this actuation approach in prosthetics and orthotics. Irrespective of the great potential of this new actuation system, it was not extensively explored due to control difficulties, the absence of suitable power sources for prosthetics, and the complexity of required electrical systems. However, Bridgestone later worked on a commercial version of the braided pneumatic actuators, named Rubbertuators [11]. Finally, in 2002, Festo® patented a fluidic muscle featuring a braided double helix material encased in a rubber bladder [12], which functioned similarly to the other actuators of this type but with enhanced durability. Presently, several corporations (namely Shadow Robot Company, Merlin Systems Corporation, Hitachi Medical Corporation, and Festo) manufacture and market McKibben muscles [13]. They have become essential components in biologically inspired robots, rehabilitation devices, exoskeletons, and various other applications [14–18].

With the growing significance of PAMs in small-scaled bio-robotic applications, numerous researchers have attempted to address the challenges associated with miniaturized PAMs and enhance their performance. However, there still remains a substantial gap in designing a miniaturized PAM with compact dimensions capable of delivering substantial force and contraction outputs. Thus, the principal objective of this thesis is to formulate a design optimization method for maximizing the force output of a small-scaled PAM. The results are experimentally validated through quasi-static tests conducted on PAM prototypes fabricated based on the optimal parameters. Furthermore, an accurate force model is derived from hysteresis test results to minimize discrepancies between predicted and actual force generated by the PAM. In this chapter, the fabrication, modelling, characteristics, and applications of the PAMs are first reviewed. Subsequently, various methodologies for enhancing their design and performance are discussed. Lastly, the motivation and objectives behind the present work are presented, followed by a description of the organization of this thesis.

1.2 Characteristics and Applications of PAMs

PAMs serve as indispensable components of a variety of robotic applications. Particularly intriguing are the smaller versions of PAMs, known as MPAMs (Miniaturized Pneumatic Artificial Muscles), with diameters of less than 10 mm. Owing to their compact size, these actuators find application in wearable hand exoskeletons [19], cardiac compression devices, tool manipulation in surgical equipment [20-22], and haptic force sensing for laparoscopic surgery [23]. PAMs have been extensively studied in robotic research as actuators for arms, legs, and hands [1-2,24-26], primarily due to their ability to imitate the properties and functionalities of human muscles. The distinctive and advantageous characteristics of PAMs that position them as the preferred choice among other actuating mechanisms are outlined below [25]:

- High power to weight ratio: When activated, PAMs can contract by 40-50% and may generate significant forces. The 6 kg 'Rubbertuator", one of the firstly designed PAMs, could move a mass of almost 2 kg [11,27]. The output force and weight of the newly commercialized PAMs by Festo [28] are up to 6 kN and around 800 g, respectively. This is much more effective than electric drives which typically provide roughly 100 W/kg.
- Flexibility and compliance: PAMs have similar flexibility to a bladder when unpressurized, but when pressured, they stiffen while maintaining a high degree of compliance. This characteristic is essential for developing medical equipment such as minimally invasive surgical tools [22,29-30] and rehabilitation robots [11,31-32].
- Compatibility with the human environment: PAMs are safer than other actuators because they employ pressured air instead of electricity, heat, or chemically active substances. The only relevant safety concern with PAM is the risk of an inner bladder rupture at high pressure, which can be prevented by adjusting the volume flow rate of air into PAMs.
- Reduced fabrication cost: PAMs might be made using low-cost prefabricated materials, making them more cost-effective than other actuators with comparable functions. Moreover, although PAMs necessitate pneumatic circuitry which may raise the initial cost, they can handle lateral and rotational misalignments, allowing for a quick production process.

- Widely accessible, low-cost, and light working fluids: PAMs can be powered by a range of fluids, including gaseous and liquid options, without the risk of explosion or fire associated with hydraulics [33].
- Diversity of sizes: PAMs come in a variety of lengths and diameters, with larger diameter muscles generating more contractile force.
- Comparable displacement to biological muscles: Displacement (contraction) varies depending on the structure but is usually 30–35% of the initial length, which is comparable to biological muscles [34].
- The ability to function in an antagonist mode: Both biological muscles and PAMs possess this ability, which is not common in traditional actuators, making them capable of controlling stiffness and compliance [34].

1.3 Fabrication and Functioning of PAMs

Elastic tubes and structural constraints make up the majority of the structure of PAMs. A flexible inner cylindrical containment layer is surrounded by an outside cylindrical braided woven layer and two end-caps, with one being sealed to close the cylinder and the other serving as an air intake channel (Fig. (1.1)). The sealed chamber of the inner layer contains pressurized gas required to power the muscle. The flexible nature of this structure allows for stretching or compression without causing damage. The outer braided layer acts as a critical component that defines many of the actuator's characteristics. It serves as a restraint layer, preventing the compressed muscle from over-inflating and rupturing. Additionally, it converts radial expansion into axial contraction, generating the necessary force for actuation. Moreover, the limits of extension and contraction are established by the braid angle. On the other hand, the friction between the braid fibers introduces energy loss, resulting in hysteresis, which reduces the contractile force and increases control complexity [24].

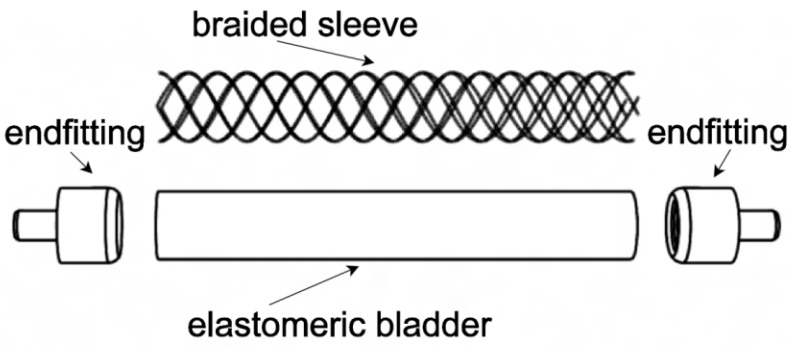

Figure 1.1: Various components of a PAM [35]

The elastomeric chamber and structural constraints can be made out of a variety of materials. While woven and knitted fabrics can be utilized as the braid in PAMs, nylon is the common material for braided sleeving because fabrics have a significant delay and friction loss despite withstanding hundreds of kilopascals and producing more than 100% strains. The bladder, on the other hand, is mainly made from latex or silicone. For example, the actuators developed by Davis et al. [1] featured an inner layer made of butyl rubber tubing, with two end-caps serving as terminal connectors to close the muscle cylinder. The end-caps could be composed of nylon, aluminum, brass, steel, or any material suited to the specific operational needs.

PAM can have several sizes, with variable force potential and displacement ranges. Muscle lengths range from under 10 cm up to 400 cm and diameters vary from less than 10 mm up to 70 mm [1]. It is worthwhile to note that for reducing energy loss resulting from the initial expansion of the rubber liner, the rubber layer is designed with a diameter comparable to the rest diameter of the flexible wall.

This combined rubber–braided nylon actuator exactly replicates the same actuation behaviour as biological muscles, working as a transmission mechanism to convert radial expanding forces to axial forces. Natural muscles are biological actuators with exceptional driving powers. Skeletal muscles, for instance, are made up of myofibrils, which are composed of myosin and actin filaments (Fig. (1.2)). When the neurons deliver an electrical signal to the muscle from the brain (controller), the release of Ca^{2+} triggers the hydrolysis of ATP (adenosine triphosphate) (rise in the inlet pressure), which energizes the movement of actin filaments along the myosin filaments (radial expansion of the bladder). Myosin is a protein that is a prototype of a molecular motor that

converts the chemical energy (ATP) to mechanical energy producing force and movement by contracting the myofibrils (axial contraction of the braid). This movement is transmitted to the bones through the tendons at the end of the skeletal muscles. When the concentration of Ca^{2+} falls (drop in the inlet pressure), the interaction between the actin and myosin filaments stops, resulting in a relaxation process [37]. In the same manner, the radial expansion of the elastic bladder causes a radial expansion of the surrounding braided sleeve as the pressure inside it changes. However, since the braided sleeve fibers are stiffer than the bladder material, they are unable to extend like the bladder and instead contract axially, allowing for an increase in diameter. The structural constraints restrict the deflection of the actuator to a single dimension to create extension, contraction, bending, or torsion under control. Contractile and extensile PAMs are two of the most common types of artificial muscles, which are differentiated based on the initial braid angle; if the initial braid angle is higher than 54.74°, a compressive force would be created, while in the braid angles lower than 54.74°, the PAM would be extensile [9]. In contractile PAMs, the constrained bladder radially expands, leading to axial shortening and the generation of compressive forces. A pulling force is created when an axial contraction occurs [2]. Conversely, in extensile PAMs, the constrained bladder radially contracts to generate an axial elongation and tensile force. Pillsbury et al. [36] fabricated and tested contractile and extensile PAMs in order to make a comparison between their performance. The results revealed that contractile PAMs with the same initial outer diameter produce more work and are more efficient. However, they have a lower stroke than the same extensile PAMs. When large strokes are needed in an application, such as continuum robotics, extensile PAMs would be chosen. On the other hand, contractile PAMs are mostly used in prosthetics, like robotic arms and legs due to their crucial characteristics, namely a high power-to-weight ratio, adjustable compliance, and a straightforward design. Since the main focus of this thesis is to design a miniaturized PAM suitable for bio-mechanical applications, the investigations are conducted on a contractile PAM.

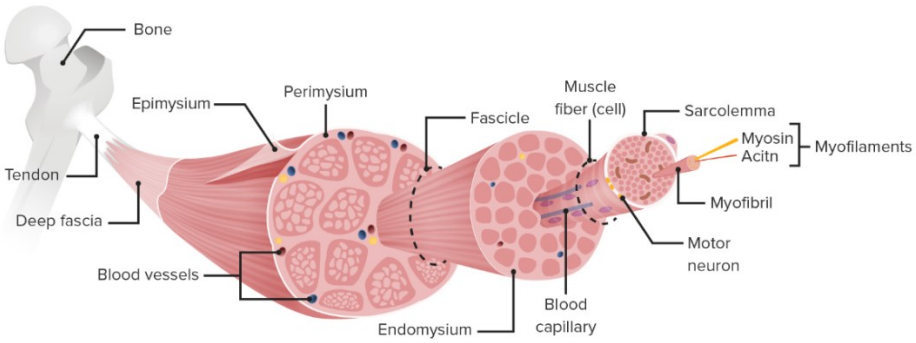

Figure 1.2: Structure of skeletal muscles [37]

1.4 Mathematical Modelling of PAMs

The extensive use and fast-speed advancements of PAMs and MPAMs in robotics have necessitated a precise mathematical description of their underlying mechanics. Such models with sufficient parameters enable the efficient selection or construction of an actuator with optimized properties for certain purposes. Various force models, ranging in sophistication, have been developed to find out how to improve PAMs. These models are either based on the virtual work theorem or the force balance equations. Additional correction terms can also be included to improve the accuracy of the ideal force models by considering the effects of non-cylindrical tips, friction, the elasticity of the bladder, and the properties of the braid. The necessity of using each correction term is dependent on the application of the PAM.

The first and simplest force model was proposed by Gaylord [8] and did not consider any of the correction terms or even the thickness of the bladder. This model was further modified by various researchers in order to improve its preciseness and make the estimated forces closer to the real results. Hocking et al. [2] proposed an analytical modelling and experimental characterization of MPAMs, which identified three main nonlinear behaviours: nonlinear PAM stiffness as a result of stiffening in the bladder at high strains, hysteresis due to friction between the actuator components, and a pressure dead-band. The stiffening and hysteresis are both functions of actuation pressure. To address each of the nonlinearities mentioned, a nonlinear elastic model expressing the stress as a quadratic polynomial of strain was added to the Gaylord model. Additionally, an empirical friction factor, which was linearly dependent on pressure, was used to model the hysteresis, while a pressure offset term accounted for the pressure dead-band. Finally, a length correction term was introduced to account for the non-cylindrical tip shape of the PAM. Experimental results showed

that the length correction term had no considerable impact on the accuracy of the force model. A comparison between theoretical and experimental force values revealed that while the nonlinear model proposed for the behaviour of the bladder was perfectly accurate with an approximate error of 0.17%, the linear elastic model over-predicted the force produced by the PAM due to considering a linear relationship between the stress and the strain over the full range of motion in the bladder. The same results were derived through the experiments carried out by Wang et al. [38], who developed a hyper-elastic model to predict the force-contraction response at different pressures. The findings of the experiments by Kothera et al. [39] again showed that the corrected term considering the elastic energy in the bladder and the braid improves the model. This term did not affect the blocked force, while it influenced the calculation of the free contraction. Using the correction term regarding the nonlinearity of the bladder, the error in calculating the free contraction was reduced by more than 40%.

It is worthwhile to mention that the extent of the improvements in the predictions of the amounts of force after adding the correction terms is dependent on the size and the geometry of the PAMs. When considering the elastic energy of the rubber bladder, smaller PAMs benefit more due to the elastic energy being dependent on the volume percent of the rubber. On the other hand, the elasticity of the braid is more significant at higher pressures and for larger actuators. The results of the experiments by Kothera et al. [39] revealed that the correction term for the non-cylindrical tips did not affect the blocked force, but improved the free contraction calculations by almost 20%.

Li et al. [40] compared three models in terms of their error and accuracy. These models were 1. the force model by Chou and Hannaford [41] which was the basic force model; 2. the model by Davis and Caldwell [1], in which the contact area of strands was calculated to consider the friction between them, and 3. the model by Ganguly et al. [42] which used a fourth-degree polynomial obtained by the least-square fitting of the experimental data. The least accuracy was related to the model proposed by Chou and Hannaford [41] due to neglecting friction. Their results revealed that adding the correction term addressing the nonlinearity of the bladder material to the ideal force model results in an adequately accurate force model, especially when the hysteresis is neglected. For high-precision calculations, the friction terms and the elastic energy stored in the braid can also be considered. Fig. (1.3) compares the importance of all compensatory terms in the force model.

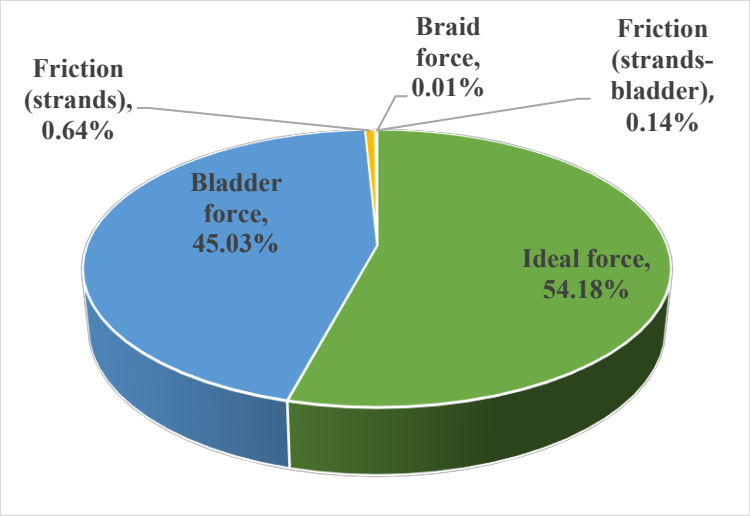

Figure 1.3: Percentage of various force terms constituting the whole force produced by a PAM

1.5 Design Improvement and Miniaturization of PAMs

The increasing demand for small-scale bio-robotic systems has led to a need for compact and efficient actuation systems capable of generating significant forces. Researchers have been focusing on improving the design and efficiency of PAMs to meet these requirements.

To reduce the size and weight of conventional PAMs, various strategies have been explored. For example, Park et al. [43] developed a PAM that detects its contraction length through hyper-elastic strain sensing with embedded microchannels containing a liquid conductor, eliminating the need for external measurement devices. Another approach by Wakimoto et al. [44] involved integrating a pressure sensor into a smart McKibben actuator using a conductive material in one of the braid fibers, allowing for pressure monitoring and control. Kanno et al. [45] designed a self-sensing PAM that measured capacitance to determine the actuator length and deformation using a dielectric elastomer sensor (DES). Fu et al. [46] introduced a multi-sensory yarn capable of detecting force, displacement, and vertical pressure variations in PAMs. Carvalho et al.[47] focused on innovative end-fittings to reduce overall length and weight while maintaining optimal muscle contraction.

Miniaturized pneumatic artificial muscles (MPAMs) possess the same benefits as PAMs but come in a significantly reduced size and weight, which is why they have found applications in various bio-robotic systems. Lathrop et al. [48] investigated the use of MPAMs in flexible instruments for minimally invasive surgery (MIS), while Markus et al. [49] utilized MPAMs to actuate fingers in a robotic hand prosthesis. Ashwin and Ghosal [50] developed an endoscopic end-effector actuated

by three MPAMs to manipulate the catheter tip. However, the fabrication and modelling difficulties are heightened for MPAMs due to their small size. Studies have indicated that these actuators exhibit lower force and contraction outputs [51,52]. Considering the wide range of applications for MPAMs, it is critical to improve their design and efficiency.

To enhance the design and efficiency of MPAMs, it is essential to quantify their performance using two key parameters: blocked force and free contraction. Blocked force refers to the force generated by a PAM when its length is held constant at its initial free length, while free contraction represents the state in which the PAM is pressured while not being constrained, thus producing no actuation force. These parameters are also significantly influenced by the geometric and material properties of these actuators. Researchers have conducted experimental studies and developed models to understand the behaviour of PAMs. Doumit and Leclair [53] developed a stiffness model which can accurately interpret the nonlinear behaviour of PAMs, considering elasticity and friction factors. Salahuddin et al. [54] proposed a characterization approach for measuring force, displacement, and free contraction for hydraulic McKibben muscles. Pillsbury et al. [55] investigated the effects of bladder thickness and material performance characteristics of PAMs, revealing that the blocked force and free contraction both decrease when the thickness of the bladder is increased. Subsequently, they conducted a comparison of three different bladder materials and observed that the PAM with a V-330 bladder exhibited the least amount of dead-band pressure while generating higher levels of force [55]. Kothera et al. [39] examined how different geometrical parameters affect the generation of blocked force, demonstrating that the length of the PAM does not impact the blocked force significantly, but increasing the braid angle and bladder diameter leads to higher force output. Similar findings were reported by Gentry et al. [33] and Joe et al. [56]. Sangrian et al. [57] proposed corrected force models for studying the effects of bladder stiffness, pressure, and length of a small hydraulic McKibben muscle, which used water or oil as the working fluid. They concluded that as the bladder stiffness increases, the blocked force and contraction decrease. Therefore, it is crucial to develop an accurate force model that allows for a comprehensive investigation of the effects of all key parameters on the force and contraction outputs of MPAMs.

In addition to understanding performance characteristics, researchers have focused on designing MPAMs with improved performance. It has been reported that small-scale hydraulic actuators

produce greater free contraction ratios [58] but at the expense of substantially higher actuation pressures, which could be hazardous in close proximity to humans. Sangrian et al. [57] used a finite element model to design an ultralight hybrid PAM with a high contraction ratio, blocked force, and axial stiffness. Yang et al. [59] developed a high displacement PAM using soft materials. Tomori et al. [60] explored extending the lifetime of straight-fiber artificial muscles (SFPAM) and emphasized the repairability of rubber bladder. Xiao et al. [61] optimized bending pneumatic artificial muscles (BPAMs) for finding the optimized parameters resulting in the maximized bending angle and force production. Diteesawat et al. [62] proposed optimal bubble artificial muscles (BAMs) to assist patients with mobility issues. The BAM's contraction was improved by optimizing the length and radius of the actuator. The produced torsion was also increased by utilizing high strength materials. Lathrop et al. [63] designed an MPAM with a concentric dual chamber to deliver greater force and contraction for applications in MIS. However, the maximum force produced by their proposed actuator is only 15.25 N, representing an improvement of approximately 2 N over prior MPAMs. Kwon et al. [64] developed a flat PAM with rigid planes as external constraints for a larger force and contraction ratio. Kim et al. [65] introduced a flat fabric PAM (ffPAM) with a maximum force of 118 N at 172 kPa and a maximum contraction ratio of 23% to be used in wearable applications. Nevertheless, the ffPAM exhibited a nonlinear force-contraction relationship, resulting in challenging length controls, and lacked a significant free contraction. Thin McKibben muscles with diameters in ranges between 1-3 mm have been also proposed to be utilized in miniaturized applications. Kurumaya et al. [66] introduced a novel approach to overcome the limitations of conventional PAMs by presenting a multifilament muscle composed of a bundle of thin McKibben muscles with outer diameters of 1.8 mm. This alternative system aims to address the stiffness issues and improve the deformation capabilities observed in traditional PAMs. In a subsequent study [67], they used 60 thin McKibben muscles to create a multifilament muscle for a musculoskeletal robot capable of mimicking the function of lower limb muscles. However, despite finding applications in various fields, thin McKibben muscles exhibit certain drawbacks compared to MPAMs, including lower force output, reduced life span, reduced reliability, reduced range of motion, and increased sensitivity to external forces. Therefore, ongoing research and further developments are necessary to overcome these challenges and further enhance the design and efficiency of MPAMs.

1.6 Current Study and Contributions

The motivation behind this thesis stems from the importance of MPAMs in various applications, particularly in bio-robotics. Previous research has identified limitations in the force and contraction capabilities of MPAMs, prompting the need for further investigation. The objective of this thesis is thus to develop an accurate design optimization strategy and conduct experiments to identify an MPAM that can generate higher blocked force and free contraction compared to other PAMs of similar size. While previous research has focused on the design optimization of full-sized PAMs, such as SFPAM, BPAM, and BAM, no study has been found on the design optimization of MPAMs within the millimeter scale to address their low force outputs. Consequently, existing attempts have resulted in bulky actuators that are unsuitable for small-scale applications. The present thesis attempts to fill this gap by formulating a formal design optimization problem to maximize the generated blocked force of MPAMs within a given volume.

To achieve this, a force equation is first derived based on the force balance equations, and correction terms are subsequently introduced to account for the bladder thickness and braided sleeving properties. The force model is used as the objective function when formulating a standard optimization formulation to maximize the blocked force of the MPAM under volume constraints. Two cases of optimization formulation are compared, providing insights into the importance of the braid correction and optimizing the braid strand parameters. The optimized MPAM is fabricated using commercially available materials and the dimensions identified through the optimization process. Customized bladders are created using a 3D-printed mold, and two different materials are used to investigate the effect of bladder material on the performance of the MPAM. The fabricated MPAMs are then tested to evaluate their force actuation performance under varying inlet pressure. The tests are conducted quasi-statically using an MTS servo-hydraulic machine, measuring the blocked force at different inlet pressures (ranging from 0 kPa to 300 kPa, with 20 kPa increments). The performance of the optimized MPAMs are compared with other MPAMs proposed in the literature to demonstrate their superior performance. Additionally, contraction tests are conducted on each MPAM under various pressures to measure their force-contraction output. The resulting data is used to derive the correction terms considering the nonlinearities of the MPAMs and the friction between their components.

1.7 Thesis Organization

This research dissertation is structured into five chapters, which systematically detail the research process and findings. Chapter 1 provides an introduction to the thesis, covering the historical background of PAMs, their properties, and their significant applications across various fields. It also discusses different modelling approaches and conducts a literature review of previous attempts to enhance the design and performance of PAMs. The motivations behind the present thesis are also included in this chapter.

Chapter 2 focuses on the mathematical modelling of PAMs, presenting a detailed description of various methods proposed for deriving correction terms. These correction terms are incorporated into the force equation to enhance its accuracy. The refined force equation serves as the objective function used in the standard optimization formulation developed in Chapter 3, which compares two distinct optimization cases in order to identify a simplified and optimized design for MPAMs. Furthermore, the optimization results are presented, along with a comparison of various optimization algorithms and a sensitivity analysis.

Chapter 4 outlines the fabrication process and test setup designed for conducting quasi-static tests on the MPAM. The results obtained from the blocked force experiments conducted on both MPAM samples are used to validate the optimization results and determine the dead-band pressure of each sample. Additionally, different empirical and theoretical methods are presented for deriving correction terms to account for the nonlinearity of the MPAMs and the friction between their components. The accuracy of the refined force model, incorporating various correction terms, is investigated by comparing the theoretically calculated force and contraction values with the experimental data under different pressures. Furthermore, a comparison is made between the outputs and the behaviour of each sample fabricated with different bladder materials.

Finally, Chapter 5 provides a summary of the major findings and contributions of this thesis, along with future remarks for potential research studies.

Chapter 2: Mathematical Modelling of PAMs

2.1 Introduction

Developing a precise force model plays an important role in the accurate prediction of the actuation behaviour of the PAMs. The force model should incorporate all geometrical parameters of the bladder and the braid that can greatly influence the performance of the PAMs. This is of great importance, particularly when aiming to optimize the design of these actuators and improve their performance. Various force models were proposed in previous studies to relate the geometrical parameters of PAMs to their outputs. These models are either based on the force balance equilibrium or the energy balance principle and can be enhanced by introducing a number of correction terms to yield more accurate results. These correction terms account for the nonlinearity of the bladder, friction between the actuator components, dead-band pressure, energy stored in the braid, and changes in length caused by the non-cylindrical tips of the PAM [39, 68-72].

In this thesis, the force balance equilibrium is used to derive the force equation of the PAM as proposed by Ferrasi et al. [70] and Kothera et al. [39]. Then, a nonlinear term is presented using two different approaches to take the elasticity of the bladder's material into account. The braid strand parameters are also integrated into the force model through a refining term regarding the energy stored in the braid. Furthermore, while the PAM is mostly considered a cylinder, it is known that it does not have cylindrical tips close to the end-fittings, therefore, another correction term is also defined to consider the effect of these non-cylindrical tips. Finally, the static friction between the strands of the braided sleeving is studied, which causes hysteresis in the force loops of the PAM. The final force equation including the mentioned refining terms can predict the behaviour and outputs of a PAM with high accuracy.

2.2 Mathematical Formulation of the Output Force

The hollow elastomeric cylinder used as the bladder has some important properties, which are its initial outer radius ($R_0 = D_0/2$), initial length (L_0), and initial thickness (t_0) as illustrated in Fig. (2.1). The braided sleeving is also characterized by its initial braid angle (α_o), the length of one of its strands before being woven around the bladder (B), and the number of turns this strand makes

from one end of the bladder to another (N) [73]. As depicted in Fig. (2.2), these parameters are related to each other as follows:

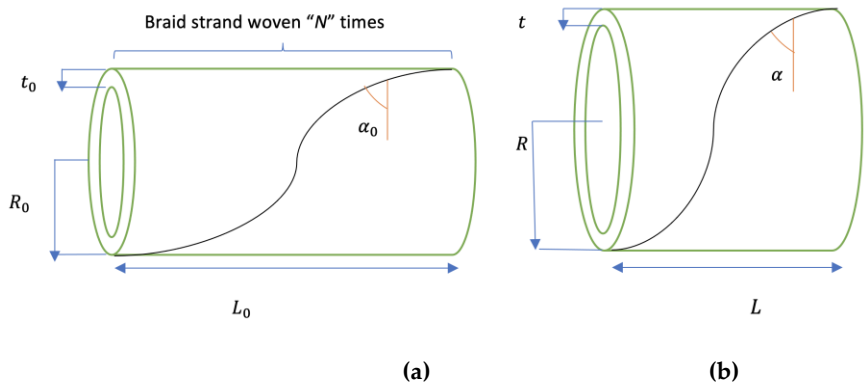

Figure 2.1: The geometry of the bladder and the braided strand woven around it at (a) initial state (b) instantaneous state

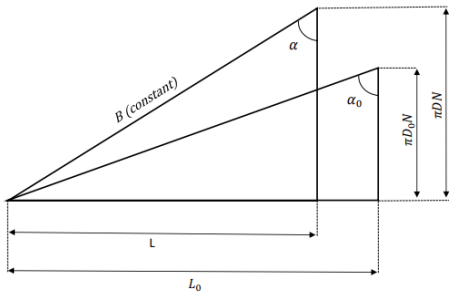

Figure 2.2: Geometrical characterization of the braid at the initial and instantaneous states

$$B = \frac{L_o}{\sin(\alpha_o)} = \frac{L}{\sin(\alpha)} \tag{2.1}$$

$$N = \frac{B\cos(\alpha_o)}{\pi D_o} = \frac{B\cos(\alpha)}{\pi D} \tag{2.2}$$

$$\tan(\alpha_o) = \frac{L_0}{\pi D_o N} \quad \text{and} \quad \tan(\alpha) = \frac{L}{\pi D N} \tag{2.3}$$

In which R, L, and t represent the instantaneous outer radius, length, and thickness of the bladder respectively, and α is the instantaneous angle of the braid. Referring to the free body diagram

illustrated in Fig. (2.3), the geometrical parameters are related to the force output of the PAM using the force balance principle. The force equilibrium in *x* and *z* directions yield:

x-direction:

$$P(R-t)L = \sigma_x tL + NTcos\alpha \tag{2.4}$$

z-direction:

$$F + P(R-t)^2\pi = \sigma_z A_{bl} + Tsin\alpha \tag{2.5}$$

where σ denotes the stress in the bladder, T is the tension in the braid, F is the generated force by the actuator, and A_{bl} is the cross-sectional area of the annular bladder. Assuming that the bladder has a constant volume, V_{bl}, one can write:

$$V_{bl} = \pi L\left({R_0}^2 - (R_0 - t_0)^2\right) = \pi L(R^2 - (R-t)^2) = \pi L(2Rt - t^2) \tag{2.6}$$

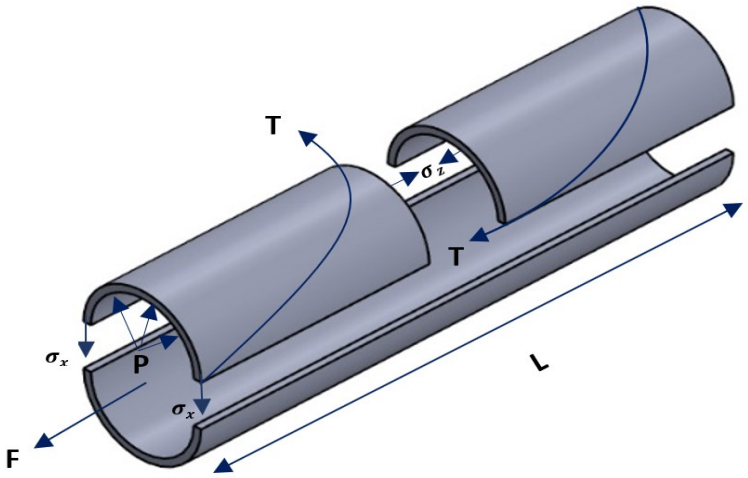

Figure 2.3: Free-body diagram of the MPAM (representing only one braid fiber)

Also, the bladder cross-sectional area, A_{bl}, is related to the bladder volume as:

$$A_{bl} = \frac{V_{bl}}{L} \tag{2.7}$$

Substituting tension *T* from Eq. (2.4) in Eq. (2.5) yields:

$$F = -P(R-t)^2\pi + \sigma_z A_{bl} + \frac{P(R-t)L - \sigma_x tL}{N}\tan(\alpha) \tag{2.8}$$

Substituting for $\tan(\alpha)$ and A_{bl} from Eqs. (2.3) and (2.7) into Eq. (2.8) yield:

$$F = P\left(\frac{L^2}{2\pi N^2} - \pi R^2\right) + P\left(\frac{V_{bl}}{L} - \frac{tL^2}{2\pi N^2 R}\right) + \sigma_z \frac{V_{bl}}{L} - \frac{\sigma_x tL^2}{2\pi N^2 R} \tag{2.9}$$

Considering Eqs. (2.1) and (2.2), one can obtain the following relation:

$$(\frac{2N\pi R}{B})^2 + (\frac{L}{B})^2 = 1 \tag{2.10}$$

Finally, substituting for R^2 from Eq. (2.10) into (2.9) yields:

$$F = \frac{P}{4N^2\pi}(3L^2 - B^2) + P\left(\frac{V_{bl}}{L} - \frac{tL^2}{2\pi N^2 R}\right) + \sigma_z \frac{V_{bl}}{L} - \frac{\sigma_x tL^2}{2\pi N^2 R} \tag{2.11}$$

It should be emphasized that the first term in Eq. (2.11) corresponds to the renowned Gaylord force model [8], which neglects the impact of nonlinearity and thickness of the bladder. The second term in Eq. (2.11) introduces a correction factor that considers the effect of the bladder thickness on the produced force and the last two terms represent the nonlinear behaviour of the PAM when the length and radius of the bladder change after contraction or extension.

2.3 Refined Force Equation for the PAM

As previously indicated, to enhance the accuracy of the anticipated amounts of force, it is necessary to refine the equation obtained in Eq. (2.11) by incorporating additional correction terms. These correction terms account for various factors, including the nonlinearity of the bladder's material, non-cylindrical tips, energy stored in the braid, pressure dead-band, and friction. In this section, the derivation of the aforementioned correction terms is discussed.

2.3.1 Nonlinearity of the Bladder

As outlined in section 1.4, previous studies have shown that the stiffening effect that occurs within the bladder during higher levels of contractions is one of the primary causes of the nonlinear behaviour of the PAM. This behaviour results in a rapid decrease in force with increased

contraction under constant pressure. This effect is particularly prominent in miniaturized PAMs, where the bladder's volume is relatively large compared to the internal volume of the actuator. Consequently, the bladder constitutes a significant portion of the whole PAM and its elasticity has a profound impact on the overall performance of the actuator. To incorporate the nonlinearity of the PAM, stress values can be substituted into the force model derived in Eq. (2.11) by employing force balance equations based on the free-body diagram of the actuator. To achieve this, the bladder is assumed to exhibit nonlinear elastic behaviour, where stress is a polynomial function of strain, as described in Eq. (2.12) [2]:

$$\sigma = \sum_{k=1}^{M} E_k \varepsilon^k \tag{2.12}$$

Where "*M*" denotes the order of the material and is selected to ensure the robustness of the model to capture the full behaviour of the actuator, and the modulus values (E_k) are empirically identified from the tensile tests of the material at each operating pressure. Considering the free-body diagram of the PAM depicted in Fig. (2.3), the circumferential and axial strains are defined as follows:

$$\varepsilon_x = \frac{\Delta R}{R_0} \tag{2.13}$$

$$\varepsilon_z = \frac{\Delta L}{L_0} \tag{2.14}$$

The circumferential and axial stresses can be subsequently obtained by substituting Eqs. (2.13), and (2.14) into Eq. (2.12):

$$\sigma_x = \sum_{k=1}^{M} E_k \left(\frac{\Delta R}{R_0}\right)^k \tag{2.15}$$

$$\sigma_z = \sum_{k=1}^{M} E_k \left(\frac{\Delta L}{L_0}\right)^k \tag{2.16}$$

Substituting Eqs. (2.15) and (2.16) into the force equation derived for PAMs based on the force balance equilibrium in Eq. (2.11) yields a more precise force model, enabling a better representation of the elasticity of the bladder and the nonlinear behaviour of the PAM as:

$$F = \frac{P}{4N^2\pi}(3L^2 - B^2) + P(\frac{V_{bl}}{L} - \frac{tL^2}{2\pi N^2 R}) + \frac{V_{bl}}{L}\sum_{k=1}^{M} E_k(\frac{L}{L_0} - 1)^k - \frac{tL^2}{2\pi N^2 R}\sum_{k=1}^{M} E_k(\frac{R}{R_0} - 1)^k \quad (2.17)$$

In the case where the bladder is assumed to be a linear elastic material (*M=1*), Eq. (2.17) can be simplified by utilizing the modulus of elasticity specific to the material of the bladder. However, as indicated previously, having an accurate prediction of the outputs of a PAM necessitates considering higher orders for the bladder material. This enhanced model improves the calculation of free contraction; however, it does not have any impact on the blocked force predictions as no contraction takes place at this condition.

2.3.2 Energy Stored in the Braided Sleeving

To account for the small amounts of strain that may be present in the braid, which contribute to smaller blocked force measurements, the elastic energy storage in the braid can be verified using the virtual work theorem based on the energy balance. This method involves calculating the tensile force generated by the MPAM by getting the derivative of the potential energy of the pressurized air (U) with respect to the length of the actuator [74]. In order to derive the correction term regarding the braid strand parameters, it is assumed that the generated force by the MPAM can be represented solely by the Gaylord term. Considering that the potential energy of the air depends on its pressure and volume, the tensile force of the actuator (Gaylord force term) can be calculated as:

$$F = \frac{dU}{dL} = P\frac{dV}{dL} \quad (2.18)$$

Assuming that the PAM is a cylinder with a volume of $V = AL$, we can write:

$$F = \frac{dU}{dL} = P\frac{dV}{dL} = PA + PL\frac{dA}{dL} \quad (2.19)$$

Under the assumption that no load is taken by the bladder, the first term in Eq. (2.19) denotes the force taken by the air, leaving the remaining force (second term) to be supported by the braid. If the braid consists of n fibers, the load carried by each individual fiber can then be expressed as follows:

$$F_{br} = \frac{PL}{nsin\alpha}\frac{dA}{dL} = \frac{PB}{n}\frac{dA}{dL} = \frac{2\pi\ PB}{n}R\frac{dR}{dL} \tag{2.20}$$

in which $A = \pi R^2$. Finally, the strain energy per unit volume in the braid can be formulated as:

$$W_{br} = \frac{1}{2}\sigma_{br}\ \varepsilon_{br} = \frac{1}{2}\frac{F_{br}}{A_{br}}\frac{F_{br}}{E_{br}A_{br}} = \frac{F_{br}^2}{2E_{br}A_{br}^2} \tag{2.21}$$

with "E_{br}" representing the Young's modulus of the braid and "A_{br}" denoting its cross-sectional area. The elastic force term associated with the braid can also be determined by applying Castigliano's theorem and Eq. (2.21), yielding:

$$F_{br} = V_{br}\frac{dW_{br}}{dL} = V_{br}\frac{2F_{br}}{2E_{br}A_{br}^2}\frac{dF_{br}}{dL} = V_{br}\frac{(2\pi)^2}{E_{br}A_{br}^2}\left(\frac{PB}{n}\right)^2 R\frac{dR}{dL}\left[\left(\frac{dR}{dL}\right)^2 + R\frac{dR^2}{dL^2}\right] \tag{2.22}$$

Considering Eq. (2.10), the radius, R, can be obtained as:

$$R^2 = \frac{(B^2 - L^2)}{(2\pi N)^2} \tag{2.23}$$

Getting first and second derivatives from both sides of Eq. (2.23) yields:

$$R\frac{dR}{dL} = \frac{-L}{(2\pi N)^2} \quad ; \quad \left(\frac{dR}{dL}\right)^2 + R\frac{dR^2}{dL^2} = \frac{-1}{(2\pi N)^2} \tag{2.24}$$

Finally substituting the relations in Eq. (2.24) into Eq. (2.22) and considering that $V_{br} = BnA_{br}$, yields:

$$F_{br} = \frac{L}{E_{br}A_{br}n}\frac{4\pi^2P^2B^3}{(2\pi N)^4} \tag{2.25}$$

By subtracting the force in the braid (Eq. (2.25)) from the force equation derived in Eq. (2.17), the modified blocked force incorporating the effect of the nonlinearity of the bladder and stored energy in the braid can be obtained as:

$$F = \frac{P}{4N^2\pi}(3L^2 - B^2) + P(\frac{V_{bl}}{L} - \frac{tL^2}{2\pi N^2 R}) + \frac{V_{bl}}{L}\sum_{k=1}^{M} E_k(\frac{L}{L_0} - 1)^k \\ - \frac{tL^2}{2\pi N^2 R}\sum_{k=1}^{M} E_k(\frac{R}{R_0} - 1)^k - \frac{L}{E_{br}A_{br}n}\frac{4\pi^2 P^2 B^3}{(2\pi N)^4} \quad (2.26)$$

2.3.3 Friction Between the Components

2.3.3.1 Theoretically Driven Friction Force

The total static friction in the PAM can be determined using the following equation, where f_s represents the friction coefficient between the strands of the braided sleeving, and f_{s-bl} denotes the friction coefficient between the braid strands and the bladder [68, 73].

$$|F_f| = (f_s + f_{s-bl}).S_{contact}.P \quad (2.27)$$

The PET nylon strands can slip against each other due to the force transmitted to them by the inner tube, but they cannot slip against the inner tube since there are no other acting forces. As stated in various references, the braid strands in contact with the inner tube remain tightly locked with it to effectively transfer the pressure from the inner tube to the braided shell. Hence, there is no movement or friction between the braid and the inner tube. Additionally, the friction coefficient between the strands and the inner tube is greater than that between the strands themselves, and as a result, due to the high static rubber friction coefficient, the strands stick against the inner tube while slipping against each other. Consequently, it can be assumed that static friction only consists of strand-on-strand friction as [73].

$$|F_f| = f_s.S_{contact}.P \quad (2.28)$$

The typical range of f_s for nylon-on-nylon contact is usually between 0.15 to 0.25 [71]. To determine the contact surface between the strands, it is assumed that the contact surface is flat, and the surface of the cylindrical bladder is entirely covered by the braid. Therefore, at the initial state

when the muscle is not contracted, the total contact surface would be equal to the lateral surface area of the bladder, which is $2\pi R_0 L_0$. Fig. (2.4) illustrates one braid crossover point using the geometrical characteristics of the pantograph network structure of the braided sleeving. It can be seen that:

$$sin\alpha = \frac{D_s}{2x} \rightarrow x = \frac{D_s}{2sin\alpha} \tag{2.29}$$

$$tan\alpha = \frac{y}{x} = \frac{sin\alpha}{cos\alpha} \rightarrow y = \frac{D_s}{2cos\alpha} \tag{2.30}$$

Using Eqs. (2.29) and (2.30), the initial contact surface of one crossover point is calculated as:

$$S_0 = 2xy = \frac{D_s^2}{2cos\alpha_0 sin\alpha_0} = 2\pi R_0 L_0 \tag{2.31}$$

When the actuator is contracted and the braid angle changes from α_0 to α, the contact surface decreases and is calculated as:

$$S_{contact} = \frac{D_s^2}{2cos\alpha sin\alpha} \tag{2.32}$$

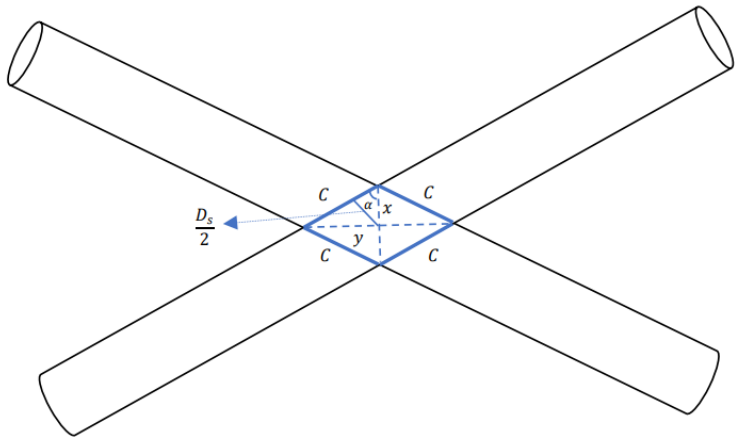

Figure 2.4: Contact surface between the braid strands

Considering that side *c* remains constant after the contraction, using Eqs. (2.31) and (2.32), the contact surface can be calculated as:

$$S_{contact} = 2\pi R_0 L_0 \frac{cos\alpha_0 sin\alpha_0}{cos\alpha sin\alpha} \tag{2.33}$$

Using Eqs. (2.1) and (2.2), we can write:

$$cos\alpha = \frac{\pi DN}{B} = \frac{2\pi RN}{B};\ cos\alpha_0 = \frac{\pi D_0 N}{B} = \frac{2\pi R_0 N}{B}\ ;\ sin\alpha = \frac{L}{B}\ ;\ sin\alpha_0 = \frac{L_0}{B} \tag{2.34}$$

Therefore, Eq. (2.33) can be written as:

$$S_{contact} = 2\pi R_0 L_0 \frac{cos\alpha_0 sin\alpha_0}{cos\alpha sin\alpha} = 2\pi R_0 L_0 \frac{R_0}{R}\frac{L_0}{L} \tag{2.35}$$

Substituting for contraction ratio ($\gamma = \frac{\Delta L}{L_0}$) in $\frac{R_0}{R}$ and $\frac{L_0}{L}$ in Eq. (2.35) yields:

$$\frac{L_0}{L} = \frac{L_0}{L_0 - \Delta L} = \frac{L_0}{L_0 - \gamma L_0} = \frac{1}{1-\gamma} \tag{2.36}$$

$$\frac{R_0}{R} = \frac{2\pi BNcos\alpha_0}{2\pi BNcos\alpha} = \frac{cos\alpha_0}{\sqrt{1 - sin^2\alpha}} \tag{2.37}$$

Knowing that $\frac{L}{sin\alpha} = \frac{L_0}{sin\alpha_0}$, one can write $sin\alpha = \frac{Lsin\alpha_0}{L_0}$, hence:

$$\frac{R_0}{R} = \frac{cos\alpha_0}{\sqrt{1 - (\frac{L^2 sin^2\alpha_0}{L_0^2})}} = \frac{cos\alpha_0}{\sqrt{1 - sin^2\alpha_0(1-\gamma)^2}} \tag{2.38}$$

Substituting Eqs. (2.36) and (2.38) into Eq. (2.35) yields:

$$S_{contact} = 2\pi R_0 L_0 \frac{R_0}{R}\frac{L_0}{L} = 2\pi R_0 L_0 \frac{cos\alpha_0}{\sqrt{1 - sin^2\alpha_0(1-\gamma)^2}} \times \frac{1}{1-\gamma} \tag{2.39}$$

Eq. (2.39) is obtained under the assumption that the contact surface is completely flat. However, the braid is comprised of cylindrical strands, the elastic deformation of which is the result of the fact that only a limited portion of the apparent contact surface is really in contact. Hence, a correction factor is introduced to take the actual strand-on-strand contact surface into account:

$$|F_f| = f_s.\frac{S_{contact}}{S_{scale}}.P \tag{2.40}$$

Various approaches have been suggested to obtain the scale factor, which are mostly empirically driven factors based on the results of the experiments conducted on a particular PAM [72]. Davis et al [24] proposed an approach based on the Hertz's contact theory to determine the actual contact area between two elastic spheres, as shown in Fig. (2.5). Based on this theory, when two spheres are in contact, their deformation depends on the modulus of elasticity of their materials. Furthermore, the contact surface is a function of the normal contact force, the radius of both spheres, and the modulus of elasticity of the material of each sphere. By applying this hypothesis, the contact force is represented as $F_{contact} = PD_s^2$, in which D_s is the diameter of the braid strands and P is the contact pressure. Utilizing the standard Hertz formula, the radius of the real contact area, which is considered a circle of radius $r_{contact}$, is calculated as [75]:

$$r_{contact} = (\frac{3}{8})^{1/3}(\frac{F_{contact}(\frac{D_s}{2})}{E^*})^{1/3} \quad ; \quad E^* = \frac{E_{br}}{2(1-{\nu_s}^2)} \tag{2.41}$$

Where E_{br} represents the modulus of elasticity of the braid strands, and ν_s denotes their Poisson's ratio. Finally, the scale factor is defined as [73]:

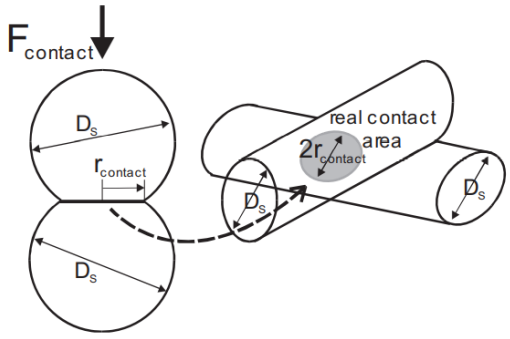

Figure 2.5: Finding the contact area between two spheres using the Hertz theory [73]

$$S_{scale} = \frac{D_s}{2r_{contact}} = (D_s/2)/\left(\frac{3}{8}\right)^{\frac{1}{3}}\left(\frac{PD_s^2\left(\frac{D_s}{2}\right)}{\frac{E_{br}}{2(1-\nu_s{}^2)}}\right)^{\frac{1}{3}} \approx 0.69 \times \left(\frac{E_{br}}{P(1-\nu_s{}^2)}\right)^{1/3} \quad (2.42)$$

Finally, substituting the scale factor from Eq. (2.42) and the contact surface from Eq. (2.39) into Eq. (2.40), the friction force which should be included in the force equation of the PAM to anticipate the hysteresis can be calculated as:

$$|F_f| = P \times (f_s) \times 2\pi R_0 L_0 \frac{cos\alpha_0}{\sqrt{1-sin^2\alpha_0(1-\gamma)^2}} \times \frac{1}{1-\gamma} \times \frac{1}{0.69} \times \left(\frac{P(1-\nu_s{}^2)}{E_{br}}\right)^{1/3} \quad (2.43)$$

2.3.3.2 Experimentally Driven Friction Force

An alternative to the previously defined theoretical friction term is the Coulomb friction term, which can be evaluated based on the experimental data obtained for a PAM contracted under a specific pressure. Since friction always opposes the motion of the actuator, this term should be subtracted from the calculated force of the PAM during contraction, and it should be added to the force equation during extension. The experimental results in the literature have shown that the magnitude of the friction is proportional to the magnitude of the axial force, hence the Coulomb friction term can be described as [2]:

$$F_f = -K_f F sgn(V) \quad (2.44)$$

The friction factor, K_f, which relates the friction force to the nominal force calculated using Eq. (2.26), is not constant and must be obtained through an empirical fit to the hysteresis loops of each specific PAM while it is being loaded (or unloaded) under a specific pressure. The term *Sgn (V)*, where *V* is the velocity of the PAM, incorporates the direction of the motion of the PAM into the friction term.

2.3.4 Pressure Dead-band

Pressure dead-band refers to the minimum pressure required for the bladder to come into contact with the surrounding braid and initiate inflation of the PAM. As a result, the PAM does not start

producing force immediately when the inlet pressure is increased. To take this effect into account, the pressure should be corrected in all force equations using the following formula [2]:

$$\acute{P} = P - P_{DB} \tag{2.45}$$

P_{DB} represents the dead-band pressure, which is generally related to the material utilized for fabricating the bladder and the braid, hence it is determined through experimental tests conducted on each particular PAM.

2.3.5 Non-cylindrical Tips

When deriving the force models for a PAM, an assumption is made that its entire length is cylindrical, which may not be valid. As illustrated in Fig. (2.6), the regions near the end fittings of a real PAM are rounded, leading to a reduction in the effective length.

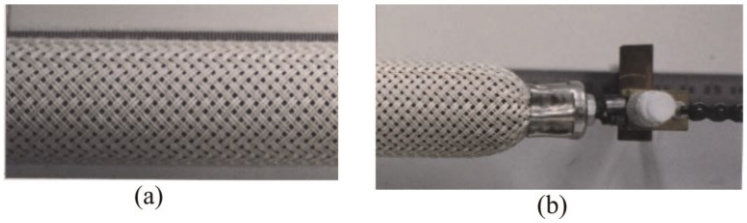

Figure 2.6: a) PAM in the middle part b) and at the endings [73]

Studies have demonstrated that the reduction in diameter near each end-fitting decreases the force response of the PAM. One of the simple approaches to correct the force model considering the non-cylindrical tips of a PAM into account is to consider the shape of the endings as a 90° circular arc [73]. Hence, the length reduction term is acquired as:

$$\Delta L = (\frac{\pi}{2} - 1)(R - R_0) \tag{2.46}$$

As a result, L should be replaced with $\acute{L}$ to correct the length in the force equation as:

$$\acute{L} = L - 2\Delta L = L - 2(\frac{\pi}{2} - 1)(R - R_0) \tag{2.47}$$

2.4 Summary and Conclusion

This chapter presents a comprehensive force model for PAMs, incorporating various terms to accurately capture their behaviour. The force model considers the effects of the elasticity of the PAM, energy stored in the braid, friction between the components, non-cylindrical tips, and dead-band pressure. First, an ideal force equation is derived based on the force balance equilibrium, known as the Gaylord model. To refine this model, a term regarding the effects of the thickness of the bladder is added, enhancing its accuracy. Then, the derivation of various correction terms is described. To investigate the nonlinearity of the PAM, a polynomial stress-strain function with the empirically determined moduli of elasticity is defined. For the effects of friction, a theoretical term is derived based on the static friction between the braid strands, which can be included in the force equation of any PAM. Alternatively, an experimental friction term proportional to the calculated force can be obtained using a friction factor determined through empirical fitting to the force-contraction graph of the PAM. This friction factor is not constant and must be determined for each specific PAM under various pressures.

Once the preferred method for addressing the effects of friction is selected, the force model including all the correction terms defined for a PAM can be expressed as follows:

$$F = \begin{cases} |F_{ideal}| - |F_{braid}| - |F_{nonlinearity}| - |F_f|, contraction \\ |F_{ideal}| - |F_{braid}| - |F_{nonlinarity}| + |F_f|, extension \end{cases} \tag{2.48}$$

Chapter 3: Design Optimization of MPAMs

3.1 Introduction

The increasing demand for compact actuators capable of generating high forces and contraction has prompted extensive efforts to improve the performance of PAMs and MPAMs. However, previous research has predominantly focused on the development of full-sized PAMs, leaving a gap in the design of miniaturized PAMs that offer enhanced force and contraction outputs. This thesis aims to address this gap specifically for MPAMs, given their expanding applications in various fields, particularly in the bio-medical domain.

Parametric studies conducted in previous research studies have revealed that the force output and contraction of MPAMs are significantly affected by their dimensional parameters and the material of their components [2,25,38-40]. As a result, optimizing these parameters can directly impact the performance of MPAMs. In this chapter, a design optimization methodology has been formulated to determine the optimal dimensional parameters of an MPAM, with the objective of maximizing the blocked force under geometrical and volume constraints. The objective function is basically the force model derived in Chapter 2, which has been modified to accurately represent the blocked force generated by the MPAM. The optimization problem incorporates geometric constraints, including a nonlinear constraint and a set of side constraints, defining the allowable ranges for the design variables. These constraints are based on the characteristics and dimensions of previously designed MPAMs.

Two optimization formulations are presented, varying in their objective functions and design variables. The first formulation employs an objective function that includes the correction term regarding the energy stored in the braid and the braid strand parameters are considered as design variables. However, the second optimization formulation employs a simplified objective function, neglecting the braid strand parameters and braid correction term. A comparison between the optimized variables obtained from the two formulations enables an assessment of the importance of optimizing braid strand parameters in maximizing the output force of the MPAM, as well as the influence of considering the energy stored in the braid on the accuracy of the force equation. The optimization problems are solved in MATLAB®, employing a hybrid optimization method that combines a genetic algorithm (GA) with either the sequential quadratic programming (SQP) or the

interior-point (IP) algorithms. By comparing the optimized values obtained from various algorithms, the most efficient algorithm is identified, and the consistency of the optimum values is determined across different cases. Finally, a post-optimality analysis is conducted on the optimal blocked force to evaluate its sensitivity to each optimization variable.

3.2 Optimization Formulation

In this section, two distinct optimization problems are formulated in the formal optimization format to maximize the blocked force of an MPAM. Some assumptions can be made to simplify the complete force equation (Eq. (2.48)) derived in Chapter 2, while still accounting for all important dimensional variables that influence the performance of the MPAM. These assumptions are based on the definition of the blocked force, being the generated force when the actuator is maintained at its initial length, and are as follows:

1. There are no changes in the length and radius of the rubber tube, implying that no strain is generated in the bladder:

   $$\varepsilon_z = \varepsilon_x = 0 \tag{3.1}$$

   Therefore, the terms representing the nonlinear behaviour of the PAM are neglected, being the third term in Eq. (2.48).
2. In the absence of any changes in the shape of the actuator, there are no frictional or hysteretic losses being the last term in Eq. (2.48).
3. Due to a constant length, the length correction term does not affect the calculations and would be omitted from the force equation.
4. The dead-band pressure term can only be determined experimentally for each MPAM with the specific materials used in its fabrication. Hence, although the force output of the actuator is affected by this term, it is neglected in the objective function.
5. The only correction term that may improve the predictions of the blocked force is the elastic energy stored in the braid. Despite the constant length of the actuator, small amounts of strain may exist in the braid, contributing to smaller blocked force measurements.

The derivation of each design optimization formulation is presented in the subsequent sections.

3.2.1 Design Optimization Formulation: Case I

The present study aims at optimizing all geometrical parameters that affect the force output of an MPAM. To achieve this goal, the objective function must establish a direct correlation between the generated force and the geometric parameters of the MPAM that are being optimized (optimization variables). For that purpose, first, Eq. (2.1) is substituted in Eq. (2.2) as:

$$N = \frac{B\cos(\alpha_o)}{\pi D_o} = \frac{L_o}{\sin(\alpha_o)} \times \frac{\cos(\alpha_o)}{\pi D_o} = \frac{L_o \cot(\alpha_o)}{\pi D_o} = \frac{L\cot(\alpha)}{\pi D} \tag{3.2}$$

Knowing that $D = 2R$:

$$N = \frac{L_o \cot(\alpha_o)}{2\pi R_o} = \frac{L\cot(\alpha)}{2\pi R} \tag{3.3}$$

Moreover, assuming a cylindrical shape for the MPAM, the following formulations can be used for the volume of the bladder and the cross-sectional area of the braid strands:

$$V_{bl} = \pi L\left({R_0}^2 - (R_0 - t_0)^2\right) = \pi L(R^2 - (R-t)^2) = \pi L(2Rt - t^2) \tag{3.4}$$

$$A_{br} = \pi R_{br}^2 \tag{3.5}$$

Considering the list of assumptions that are made based on the blocked force state, we can conclude that the force equation of the MPAM is simplified as follows:

$$\sum_{k=1}^{M} E_k\left(\frac{L}{L_0} - 1\right)^k = \sum_{k=1}^{M} E_k\left(\frac{R}{R_0} - 1\right)^k = 0 \text{ ; hence: } \left|F_{nonlinearity}\right| = 0 \tag{3.6}$$

$$\left|F_f\right| = 0 \tag{3.7}$$

$$\Delta L = 0 \;;\; \acute{L} = L - 2\Delta L = L \tag{3.8}$$

$$P_{DB} = 0 \;;\; \acute{P} = P - P_{DB} = P \tag{3.9}$$

Hence, the final blocked force equation formulated in Chapter 2 can be written as:

$$F_b = |F_{ideal}| - |F_{braid}| = \frac{P}{4N^2\pi}(3L^2 - B^2) + P\left(\frac{V_{bl}}{L} - \frac{tL^2}{2\pi N^2 R}\right) - \frac{L}{E_{br}A_{br}n}\frac{4\pi^2P^2B^3}{(2\pi N)^4} \tag{3.10}$$

Substituting B, N, and V_{bl} from Eqs. (2.1), (3.3) and (3.4) in Eq. (3.10) yields:

$$F_b = \frac{P}{4(\frac{L\cot(\alpha)}{2\pi R})^2\pi}\left(3L^2 - (\frac{L}{\sin(\alpha)})^2\right) + P\left(\frac{\pi L(R^2-(R-t)^2)}{L} - \frac{tL^2}{2\pi(\frac{L\cot(\alpha)}{2\pi R})^2 R}\right) \quad (3.11)$$

$$- \frac{L}{E_{br}\pi R_{br}^2 n}\frac{4\pi^2 P^2(\frac{L}{\sin(\alpha)})^3}{\left(2\pi\frac{L\cot(\alpha)}{2\pi R}\right)^4}$$

$$= \frac{P\pi R^2}{cot^2(\alpha)}\left(3 - (\frac{1}{\sin(\alpha)})^2\right) + P\left(\pi(R^2-(R-t)^2) - \frac{2\pi Rt}{cot^2(\alpha)}\right)$$

$$- \frac{sin(\alpha)}{E_{br}R_{br}^2 n}\frac{4\pi P^2 R^4}{cos^4(\alpha)}$$

As expected, the blocked force equation does not incorporate the length of the actuator, given that the length is fixed in this state. Finally, knowing that $\cot(\alpha) = \frac{\cos(\alpha)}{\sin(\alpha)}$ and $\tan(\alpha) = \frac{\sin(\alpha)}{\cos(\alpha)}$, the objective function in Eq. (3.11) can be expressed as:

$$F_b = P\pi\left[R^2(2tan^2(\alpha)-1) + (2Rt - t^2) - 2tR(tan^2(\alpha)) - \frac{4PR^4 sin\alpha}{E_{br}nR_{br}^2(cos\alpha)^4}\right] \quad (3.12)$$

The blocked force equation takes into account several geometric parameters that have a significant impact on the performance of the MPAM. These parameters include the radius and thickness of the bladder (R and t), the braid angle (α), the radius of the braid strands (R_{br}), and the number of the braid fibres used to make the braided sleeving (n). Other independent parameters are assumed to remain constant throughout the optimization process. The air pressure inside the bladder is maintained constant for each optimization run, and the braid is selected from the commonly used PET (polyethylene terephthalate) braids with a specific modulus of elasticity ($E_{br} = 2.1$ GPa). Therefore, the vector of design variables comprises five elements:

$$X = [R, t, \alpha, R_{br}, n]^T \quad (3.13)$$

The identified design variables are subjected to certain geometrical constraints (side constraints) and a nonlinear constraint associated with the bladder's thickness-to-radius ratio. In order to ensure a uniform pressure distribution throughout the length of the actuator, the ratio between the volume of the bladder and the volume of the entire structure of the actuator must fall within a certain range.

Assuming that the radius of the actuator is equal to the outer radius of the bladder, the mentioned ratio is calculated as below:

$$\frac{V_{bl}}{V} = \frac{\pi L(R^2 - (R-t)^2)}{\pi L R^2} = \frac{\pi L(2Rt - t^2)}{\pi L R^2} = \frac{t}{R}(2 - \frac{t}{R}) \tag{3.14}$$

Eq. (3.14) demonstrates that the ratio of the bladder volume to the actuator volume is directly proportional to the ratio of the wall thickness of the bladder to its outer radius. In miniaturized PAMs, this ratio is often significant since the bladder constitutes a much larger portion of the actuator's cross-sectional area. Therefore, the recommended range for this ratio is typically between 0.4 and 2 for MPAMs [55].

Geometrical side constraints are limitations on the dimensions of the MPAM based on its intended application and the typical dimensions of the previously designed and commercialized MPAMs. The optimization problem is formally formulated by incorporating the aforementioned constraints as below:

Find the vector of design variables: X

To maximize: $F_b(X)$

Subject to the following constraints:

$$X_{min} \leq X \leq X_{max} \tag{3.15}$$

$$\frac{V_{bl}}{V} - 2 \leq 0$$

$$0.4 - \frac{V_{bl}}{V} \leq 0$$

The lower and upper bounds of each design variable are provided in Table (3.1).

Table 3.1: Lower and upper bounds of the design variables

Design variable	Lower bound	Upper bound
$R\ (mm)$	0.45	3
$t\ (mm)$	0.16	1.5
$\alpha\ (°)$	36	72
$R_{br}(mm)$	0.005	2.5
n	30	100

3.2.2 Design Optimization Formulation: Case II

The objective function for the second optimization problem excludes the term associated with the energy stored in the braid from the blocked force equation. This is conducted to investigate how significant this effect is on the force output of an MPAM and to assess the impacts of optimizing braid parameters on maximizing the blocked force. Consequently, neglecting the elastic energy stored in the braid (the last term in Eq. (3.12)) yields:

$$F_b = P\pi\ [R^2(2tan^2(\alpha) - 1) + (2Rt - t^2) - 2tR(tan^2(\alpha))] \tag{3.16}$$

The braid parameters are thus omitted, reducing the number of design variables to three. The new vector of design variables is as follows:

$$Y = [R, t, \alpha]^T \tag{3.17}$$

Neglecting the impacts of the stored energy in the braided sleeving does not affect the constraints of the optimization problem. The ratio defined between the thickness and outer radius of the bladder, which ensures pressure consistency, remains independent of the braid characteristics and should still be within the predetermined range. Additionally, the side constraints remain unchanged as they pertain to the required dimensions of the actuator designed for specific small-scale applications. Based on the modified objective function and design variables, the second optimization problem can be formally expressed as:

Find the vector of design variables: Y

To maximize: $F_b(Y)$

Subject to the following constraints:

$$Y_{min} \leq Y \leq Y_{max} \tag{3.18}$$

$$\frac{V_{bl}}{V} - 2 \leq 0$$

$$0.4 - \frac{V_{bl}}{V} \leq 0$$

3.3 Optimization Methodology

The optimization problem discussed in this study involves a nonlinear objective function and a nonlinear inequality constraint, making it a nonlinear optimization problem, which can be solved using various direct and indirect optimization techniques. However, direct techniques are generally preferred due to their accuracy. Selecting an appropriate optimization method is crucial for achieving a fast and accurate optimization procedure. In this thesis, a hybrid optimization approach, in which a gradient-based optimization technique has been combined with a stochastic-based algorithm, is implemented in the MATLAB® environment to assure the convergence to a global optimum solution. The hybrid optimization method used in this thesis combines the Genetic algorithm (GA) with either Sequential Quadratic Programming (SQP) or Interior Point (IP). Both SQP and IP are gradient based optimization algorithms that require gradients of the objective and constraint functions to search design space starting from an initial point and usually converge to a local optimum point without a mechanism to search for a global solution. GA, on the other hand, is a non-gradient, search-based optimizer that can stochastically converge to a near-global solution. Therefore, the optimization procedure is initiated with GA, and the optimal results from GA are then used as the initial points for the local optimizer (IP or SQP) to obtain the "true" global optimal values.

Further descriptions of each of the employed optimization algorithms can be found in the subsequent sections.

3.3.1 Genetic Algorithm (GA)

A genetic algorithm is a search-based method that emulates the process of natural selection and genetics in order to evolve the optimization problem toward the best solution. This evolutionary algorithm commences by generating a population of prospective solutions for a given problem, with each solution represented as an individual. The population size, referred to as generations, is randomly determined and varies based on each problem. In each generation, the fitness of each individual is assessed based on their ability to solve the problem, typically measured by the objective function value. The fittest individuals are then randomly selected and used to form the subsequent generation.

The genetic algorithm applies biologically inspired operators such as crossover, selection, and mutation to the population in order to produce a new generation in each iteration. The selection operator favors the fittest individuals, while the crossover and mutation operators introduce genetic diversity and variability to the population. This process of evaluating fitness, selecting the fittest individuals, and applying genetic operators is repeated for multiple generations until a satisfactory solution is found or a termination criterion is reached. The termination criterion can be the maximum number of generations produced or a satisfactory fitness level.

Genetic algorithm has been widely used in optimization problems, especially in engineering design. It is particularly useful in situations where the search space is extensive and complex, and traditional optimization methods may be too slow or infeasible [77].

3.3.2 Sequential Quadratic Programming (SQP)

SQP is a powerful gradient-based optimization technique that can numerically determine an accurate solution for nonlinear optimization problems with linear or nonlinear equality and inequality constraints. SQP is a suitable and efficient algorithm for real-world problems due to its capability to handle any degree of nonlinearity, including nonlinearity in the constraints. This iterative algorithm approximates the objective function and constraints by solving a quadratic model at each iteration to obtain a search direction, which is then used to update the current solution. The step size is determined using a line search method. Finally, SQP converges to a local optimum point near the initial point faster than stochastic approaches searching for local minima

of a function. However, the resulting optimum point depends on the starting point, which is why accurate initial points must be chosen.

An active set method and Quasi-Newton's method are combined in SQP. The active set method solves the KKT (Karush-Kuhn-Tucker) conditions using guesses and checks to find the critical points. In the first step, it is assumed that every inequality constraint is inactive, and after solving the problem, feasibility is checked. If any constraints are violated, they are active, and on the other hand, if any of the multipliers of a constraint are negative, the constraint is considered inactive. A limitation of the active set method is that many of the derivatives in the KKT conditions are highly nonlinear and difficult to solve. This is resolved by SQP which incorporates Quasi-Newton's method [77].

The SQP is more efficient for small to medium-sized problems, while for large problems, the algorithm may become computationally expensive due to the need to solve a quadratic programming subproblem and incorporate several derivatives at each iteration [77].

3.3.3 Interior Point (IP)

The IP algorithm, which shares a similar background with SQP, has gained widespread popularity over the past 15 years and has become the default optimization algorithm in MATLAB ®. Similar to SQP, IP is a local optimizer that requires an initial point to start its iterations, and the objective function and constraints must be twice differentiable for the algorithm to be employed. IP can handle all types of optimization problems, including linear, nonlinear, convex, and nonconvex, and as opposed to SQP, it is particularly useful for large-scale problems. The IP method is named after its iterative movement along a path of strictly feasible solutions in the interior of the feasible set.

IP works by solving a sequence of barrier subproblems that involve adding a barrier function to the objective function of the original optimization problem. The barrier function, which is convex, becomes increasingly steep as the iterations approach the boundary of the feasible set, effectively bypassing infeasible solutions. At each iteration, the KKT conditions, i.e. the Hessian and gradient, of the barrier subproblem are used to compute a search direction. The algorithm then takes a step in the search direction by adjusting the step length to satisfy the feasibility and optimality conditions of the barrier subproblem, using either a line search or a trust-region method. The IP

algorithm terminates when a stopping criterion is satisfied, such as reaching a desired level of optimality or approaching the boundary of the feasible set within a desired tolerance [77].

IP offers several advantages over other optimization algorithms, including faster convergence rates and the ability to handle a wider range of optimization problems, including those with inequality constraints and problems with non-smooth objective functions. However, it can be computationally expensive for large-scale problems due to the need to solve a sequence of barrier subproblems.

3.4 Optimization Results

3.4.1 Comparison Between the Proposed Optimization Formulations

The optimization formulations presented in section 3.2 aimed to investigate the impact of braid geometry on the maximized blocked force and optimal dimensions of an MPAM. Two different formulations, referred to as Case I and Case II, are proposed and optimized, and their results are compared in Table (3.2). It is important to note that the data provided in Table (3.2) corresponds to a 200 kPa inlet pressure, but similar results were obtained for a range of different pressures. The results presented in Table (3.2) demonstrate that the optimal values of $R, t,$ and α, which are the design variables that are present in both formulations, remain constant regardless of the braid term added in Case I. The insignificant decrease (0.00647 N) in the maximized blocked force obtained from the first formulation, which optimizes the properties of the braid strands, is attributed to subtracting the energy stored in the braid from the total amount of force. This indicates that including the properties of the braid strands as optimization variables does not significantly impact the maximization of the force output of an MPAM. Consequently, the second formulation (Case II) is preferred for the remainder analysis in this thesis. Case II not only yields the same optimized dimensions for the MPAM but also offers the advantage of a simpler and more cost-effective design. This is because Case II allows for the utilization of commercially available braided sleeving without the need to customize a braid with optimized dimensions.

Fig. (3.1) illustrates the iteration history for both optimization cases. The iteration number represents the number of times the optimization algorithm is run before converging to the optimum values. Despite Case I having 5 design variables and Case II having three, the initial values of the

design variables that are common in both cases are equal to ensure similar initial conditions for the optimization algorithm in both cases. It can be observed that the value of the objective function converges to the same optimum blocked force for both cases, confirming that they lead to the same optimized dimensions for the MPAM.

Table 3.2: Optimum values obtained using different optimization formulations (P=200 kPa)

	Optimum values					Cost function
	R (mm)	t (mm)	α (°)	R_{br} (mm)	n	
Case I	3	0.67621	72	0.0025	50	79.58108
Case II	3	0.67621	72	---	---	79.58755

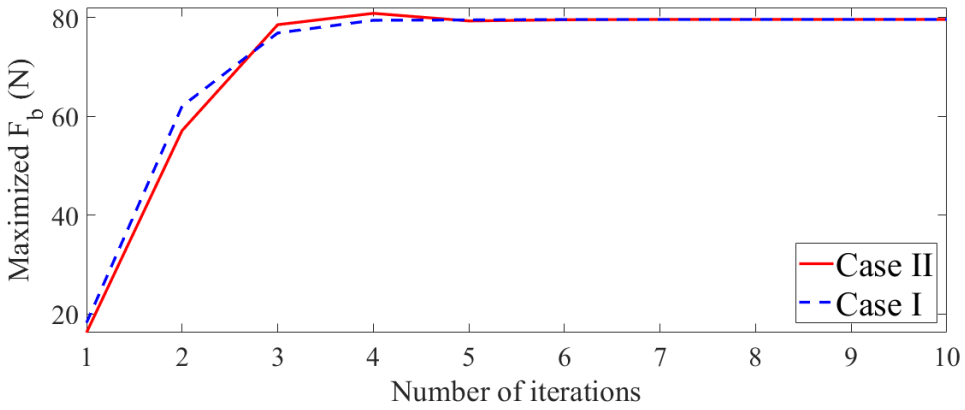

Figure 3.1: Variation of the optimal blocked force with the number of iterations for two different optimization formulations using the IP algorithm (P = 200 kPa)

As a complement to the aforementioned results, the optimal parameters obtained from the previous optimization problems were fed into three different force models proposed for the PAMs as input values to compare their results: 1. The basic Gaylord model; 2. The Gaylord model incorporating the effects of the thickness of the bladder; and 3. The Gaylord model including the effects of the bladder's thickness and energy stored in the braid. The blocked force values calculated using each force model are compared in Fig. (3.2) for a range of air pressures. It is clear that the simple Gaylord model overestimates the blocked force, specifically at higher pressures. This discrepancy arises from the model's failure to account for the thickness of the bladder, which plays a crucial

role in a precise calculation of the generated force by an MPAM. On the other hand, the insignificant discrepancies between the amounts of force predicted using the other two equations prove that the term regarding the effects of the braided sleeving does not contribute to more accurate force anticipation.

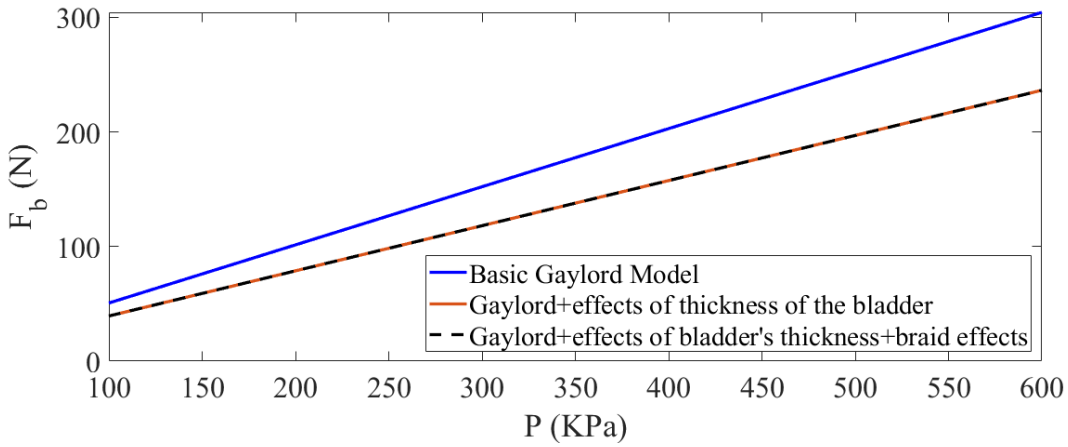

Figure 3.2: Comparison between the anticipated amounts of force using three various force equations

3.4.2 Comparison Between the Optimization Algorithms

As mentioned in Section 3.3, a hybrid optimization algorithm combining a global stochastic-based algorithm (i.e. GA) with a gradient-based algorithm (i.e. IP or SQP) is effectively utilized to find the true global optimum. GA yields near-global optimum solutions which are then fed into IP and SQP as the initial points to catch accurate global optimum solutions.

Table (3.3) presents three optimum points obtained from the GA, indicating that this algorithm does not converge to the same optimal points when different random initial points are used. This implies that the GA is unable to find the exact global optima. To obtain the true global solution, the results from the GA are further processed using the SQP or IP algorithms. Fig. (3.3) and Fig. (3.4) illustrate the iteration history utilizing GA+ IP and GA+SQP algorithms, respectively. Both algorithms converge to the same true global optimum, regardless of the three different optimum points obtained from the GA used as their initial points. Table (3.4) represents the average values of the optimal points acquired from 10 repetitions of the GA, as well as the true global optimum points obtained from the IP and SQP algorithms using the average results from the GA as their

starting values. It is observed that both the IP and SQP algorithms converge to the same global optima, although they require a different number of iterations. The SQP algorithm, which is known for its fast speed convergence to the optimum points, reaches the true maximum value of the cost function after only 4 iterations, while the IP method requires 9 iterations, more than twice the number required by the SQP algorithm. It is noteworthy that all algorithms, including multiple attempts of the GA, converge to the same optimal values for the radius of the bladder and the braid angle. On the other hand, the true optimum value for the thickness of the bladder is obtained using combined GA and SQP or IP.

Table 3.3: Optimization results from the GA using randomly generated initial points

	Optimum values			**Optimized Cost function from GA**
	$\boldsymbol{R}$ $(\boldsymbol{mm})$	$\boldsymbol{t}$ $(\boldsymbol{mm})$	$\boldsymbol{\alpha}$ (°)	
$\boldsymbol{X_1}$	3	0.8639	72	72.7868
$\boldsymbol{X_2}$	3	0.6751	72	79.4214
$\boldsymbol{X_3}$	3	0.8638	72	72.7911

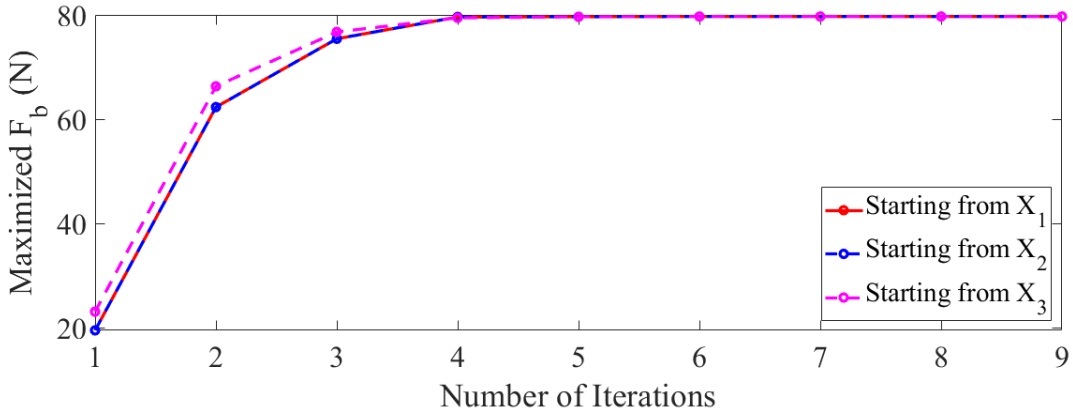

Figure 3.3: Convergence of GA+IP to the true global optimum

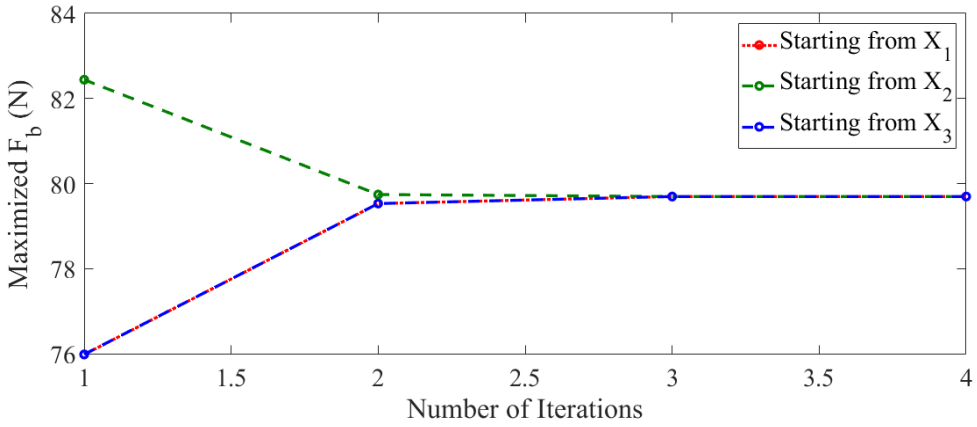

Figure 3.4: Convergence of GA+SQP to true optimum

Table 3.4: Optimum points from different optimization algorithms (P = 200 kPa)

	Optimum values			**Optimized Cost function**	**No. of iterations**
	$\boldsymbol{R}$ $(\boldsymbol{mm})$	$\boldsymbol{t}$ $(\boldsymbol{mm})$	$\boldsymbol{\alpha}$ (°)		
GA	3	0.75092	72	77.1344	3
GA+SQP	3	0.67621	72	79.5875	4
GA+IP	3	0.67621	72	79.5875	9

3.4.3 Analysis of the Optimal Points

The results presented in Table (3.4) indicate that the optimal values for the radius of the bladder and the braid angle have converged to their respective upper bounds. This observation is consistent with previous parametric studies that have reported an increase in the force output of an MPAM with an increase in these parameters (R and α) [2,39,55,76].

The presence of accurately defined constraints that are active at the optimum points has also a considerable impact on the optimization outcomes. In the absence of such a constraint, the optimization results can vary. It can be observed that at optimal solutions, the nonlinear constraint V_{bl}/V becomes active on its lower bound (0.4) in optimization formulations in Cases I and II as shown below:

$$\frac{V_{bl}}{V} - 2 = \frac{t}{R}\left(2 - \frac{t}{R}\right) - 2 = \frac{0.67621}{3}\left(2 - \frac{0.67621}{3}\right) - 2 = -1.6 \leq 0 \tag{3.19}$$

$$0.4 - \frac{t}{R}\left(2 - \frac{t}{R}\right) = 0.4 - \left(\frac{0.67621}{3}\left(2 - \frac{0.67621}{3}\right)\right) = 0 \leq 0 \tag{3.20}$$

The impacts of varying the inlet pressure on the optimized values are investigated by repeating the optimization procedure for a range of pressures. Optimal results for the various inlet pressure are presented in Table (3.5). Variation of the optimal blocked force versus inlet pressure is also shown in Fig. (3.5). Results reveal that although the maximized blocked force increases linearly with pressure, the global optimum values of the geometrical parameters for an MPAM remain constant. It is clear that the inlet pressure does not affect the optimization results, and the observed increase in the optimum blocked force is solely due to the positive correlation between the force output of PAMs and the pressure inside their bladder [55,39]. The results demonstrate that increasing the inlet pressure of an MPAM with the optimized dimensions obtained in this work from 50 kPa to 600 kPa results in a blocked force approximately 12 times higher than the initial amount. Results show that an MPAM comprising a bladder with a radius of 6 mm and wall thickness of 0.67621 mm, along with a braided sleeving with a braid angle of 72 degrees can have a force output of almost 238 N if the bladder is pressured up to 600 kPa.

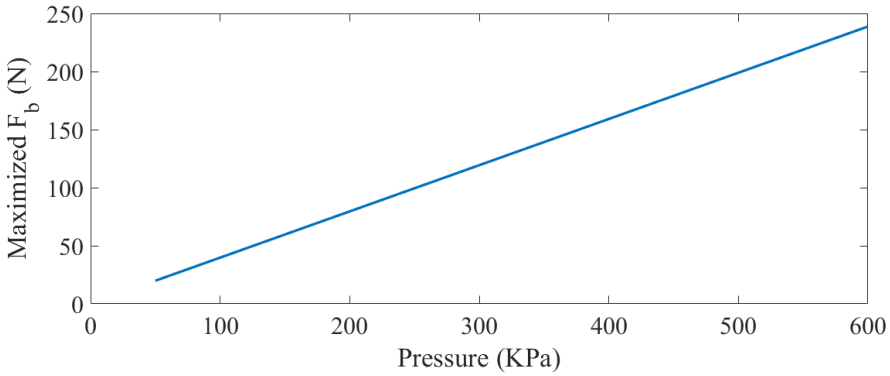

Figure 3.5: Maximized amounts of blocked force under various inlet pressures

Table 3.5: Optimal points using various inlet pressures

P (kPa)	R (mm)	t (mm)	α (°)	Cost function (Case I)	Cost function (Case II)
50	3	0.67621	72	19.89648	19.89689
100	3	0.67621	72	39.70377	39.79216
200	3	0.67621	72	79.58109	79.58755
300	3	0.67621	72	119.3668	119.3813
400	3	0.67621	72	159.1492	159.1751
500	3	0.67621	72	198.9487	198.9689
600	3	0.67621	72	238.7335	238.7627

To further investigate the impacts of the braid strand parameters on the optimization results and to determine whether these effects are dependent on the inlet pressure, the optimization procedure is also conducted using the optimization formulation including the braid term (Case II). Eq. (2.26) reveals that the force associated with the braided sleeving has a direct relationship with the inlet pressure. Nevertheless, the error between the maximized blocked force in Cases I and II at different pressures is nearly less than 0.01%. These findings are consistent with the results obtained from various force models in Fig. (3.2).

3.4.5 Post-Optimality Analysis

The effect of variation in the optimal parameters on the maximized blocked force is investigated in this section. The study considers variations in the design parameters (R, t, α), with one parameter being perturbed $\pm 5\%$ around its optimum value while the other design variables remain constant. Fig. (3.6) illustrates the magnitude of the blocked force concerning variations in each design parameter.

Fig. (3.6a) demonstrates a linear rise in the blocked force with increasing the bladder's outer radius. Since the optimum value of R converges to the upper bound of this parameter, the optimal point falls in the middle of the range of the sensitivity analysis. Based on the direct relationship between R and F_b, if the upper bound of this optimization variable is relaxed, the optimization converges

to a higher blocked force. However, due to the goal of this work to maximize the force output of a ”miniaturized” PAM within specific dimensional ranges, higher upper bounds cannot be used for its dimensional parameters.

As mentioned in section 3.2, a specific ratio exists between the volume of the bladder and the volume of the entire structure (V_{bl}/V) of the PAM, which is directly related to the ratio between the thickness and the radius of its bladder $\frac{t}{R}\left(2-\frac{t}{R}\right)$. Hence, when altering the optimal thickness of the bladder to investigate its effect on the blocked force, the mentioned ratio and thus the value of R should also be considered. This is why variations in the lower boundaries of V_{bl}/V ratio which are active at the optimum solution are studied to determine the effects of the thickness of the bladder on the optimization results. As indicated in Fig. (3.6b), if the lower boundary for V_{bl}/V is relaxed, a linear increase can be observed in the blocked force. However, for a given thickness, this leads to a larger R and thus bigger MPAM.

Finally, post-optimality on the braid angle (Fig. (3.6c)) yields a significant rise in the magnitude of the blocked force with higher values for the braid angle. Increasing the braid angle to 75 ° results in a nearly 50% increase in the amount of the blocked force compared to an MPAM with α=72°. On the other hand, apart from the existing dimensional constraints for an MPAM, there is a practical limit for the maximum braid angle. The braid angle 72° is selected, since it can be readily found in commercialized braided sleeving available in the market.

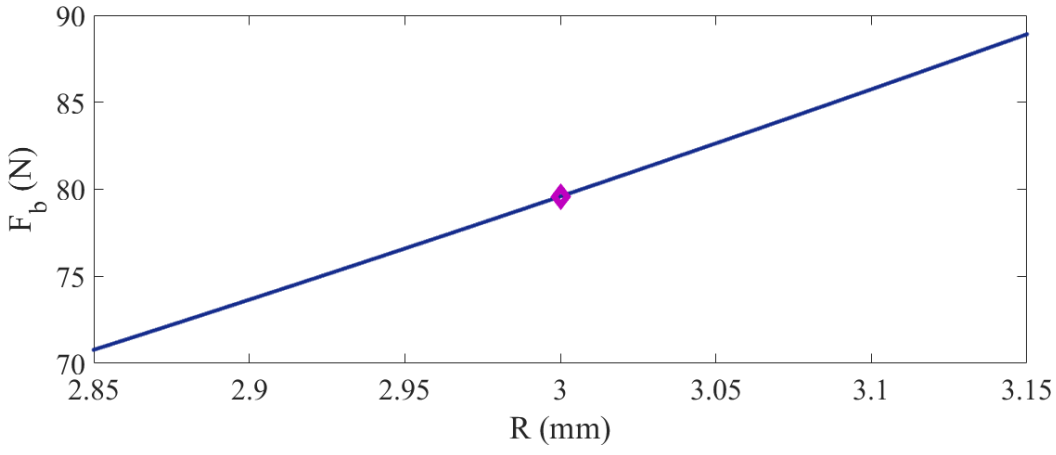

(a)

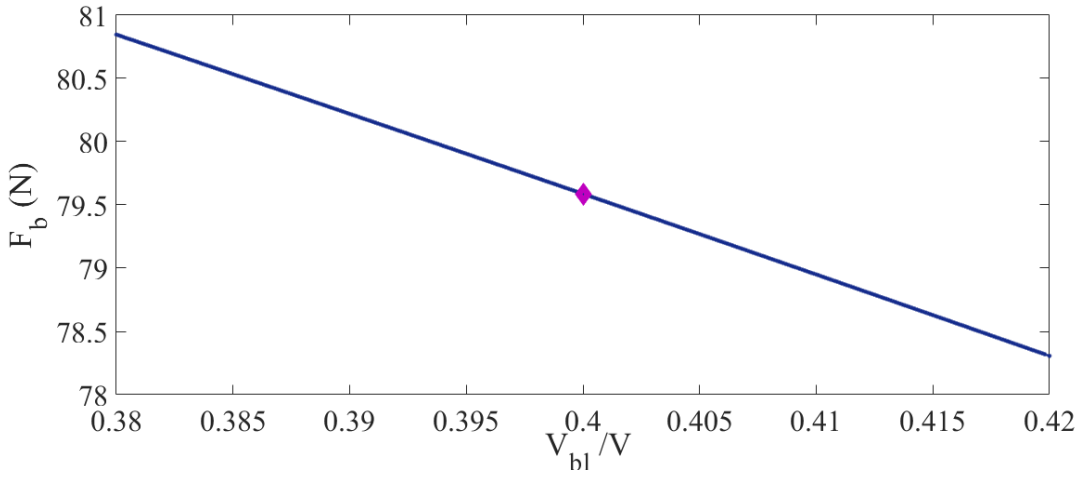

(b)

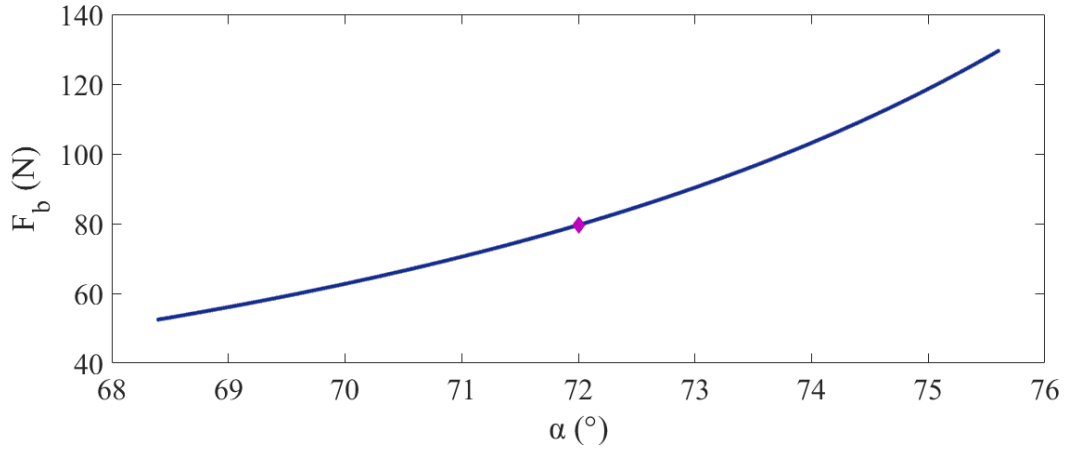

(c)

Figure 3.6: Sensitivity analysis with respect to the (a) bladder's outer radius (b) thickness of the bladder (c) braid angle (P = 200 kPa)

3.5 Summary and Conclusion

In this chapter, formal design optimization problems were formulated and then implemented in the MATLAB® optimization toolbox to obtain the optimum dimensional parameters of an MPAM to maximize the blocked force. Two optimization formulations, Case I and Case II, were developed with different objective functions and vectors of design variables. Case I included a term representing the energy stored in the braided sleeving, and thus the parameters related to the

properties of the strands used in the braided sleeving were included as the optimization variables. On the other hand, Case II neglected this term, resulting in a simpler optimization problem with a reduced number of design variables. A comparison between the results of these two cases revealed that Case II was accurate enough to find the optimal dimensions of an MPAM, leading to a more straightforward and cost-effective design for the optimized actuator. A hybrid optimization approach, combining the GA with either SQP or IP algorithms was employed to find the exact global optimum results and to make a comparison between the various algorithms and their effects on the optimization results. Finally, a post-optimality analysis was conducted to investigate the dependence of the maximized blocked force on the variation of each optimal design variable. Results show that within the dimensional constraints defined for a miniaturized PAM, the optimization procedure successfully converged to the true global optimum.

Chapter 4: Experimental Validation

4.1 Introduction

In Chapter 3, we presented an optimization framework to determine the optimal dimensions of MPAMs for achieving maximum force output. To validate the accuracy of the model and optimization results, MPAMs using the optimal dimensions obtained in Chapter 3 are fabricated and experimentally tested to evaluate their blocked force and free contraction under varied inlet pressures. In this chapter, the fabrication process of the MPAMs is described in detail, including the selection of the materials, manufacturing techniques, and assembly procedures.

A critical aspect of the fabrication process is the choice of the bladder material, as it significantly affects the stiffness, strength, and overall performance of the actuator. Two samples of MPAM are fabricated, each with a different bladder material, allowing us to investigate the effect of bladder material and the differences between their performances. Following the fabrication process, the MPAM samples are tested under quasi-static conditions using an MTS machine and a customized test setup. The test procedure involves measuring the blocked force and free contraction of the MPAMs and obtaining their hysteresis loops. The hysteresis loop is a graphical representation of the force-contraction relationship of the actuator and is an important indicator of its repeatability and controllability. The experimental data are then utilized to determine the correction terms that should be added to the simplified force equation used as the objective function in the optimization process. By comparing the hysteresis loops of the fabricated MPAMs with the theoretical predictions obtained from the modified force equation, we can verify the accuracy of the force equation and its ability to anticipate the force and contraction outputs of the MPAMs under different inlet pressures.

4.2 Fabrication of the Optimized MPAM

4.2.1 Selection of the Main Components

The present study aims at developing a low-cost MPAM utilizing commercially available materials. The MPAM is mainly composed of three major components: 1. A cylindrical elastomeric bladder to contain the pressurized air that powers the muscle, 2. A braided sleeve to transform the radial expansion of the muscle into axial contraction, hence generating the actuation

force and, 3. Two end-fittings, one of which seals the muscle cylinder, while the other serves as an air intake channel. The aforementioned critical components of the MPAM are carefully chosen based on their material properties and cost-effectiveness to ensure the desired performance:

1. The dynamic nature of the actuation process requires the bladder material to possess both flexibility and durability to withstand repeated cycles of inflation and deflation. Ecoflex silicone rubbers are frequently utilized for PAM bladders owing to their distinctive properties, such as high elasticity, low deformation, and resistance to tearing under high mechanical stress. Additionally, their biocompatibility and chemical resistance make them suitable for applications in prosthetics and biomedical devices. The Ecoflex-50 silicone mixture is selected as the material of choice for the bladder in this study due to its availability, and it is formulated in a 1A:1B weight ratio and cured at room temperature to form a soft yet robust bladder that can expand and contract without tearing or distorting. To compare the performance of MPAMs fabricated with various bladder materials, a second bladder is also fabricated using a different silicone mixture, including polydimethylsiloxane (PDMS) and Ecoflex-30 (1:10). Although both PDMS and Ecoflex possess remarkable elasticity, Ecoflex has lower stretchability than PDMS, which can be stretched up to several times its original size before breaking. Ecoflex is also available in a range of hardness levels, while PDMS is known for its low hardness and flexibility. Although both materials are generally biocompatible and chemically resistant, PDMS may be more resistant to certain chemicals. Finally, Ecoflex is usually less expensive than PDMS. PDMS is not typically utilized in PAMs due to its inferior tensile strength in comparison to elastomers such as silicone. This deficiency results in its inability to endure the elevated forces and stresses that occur during actuation. Its low tear resistance is another significant issue, rendering it vulnerable to tearing under mechanical stress, which is not ideal for use in PAMs demanding high levels of durability and reliability. A limited temperature range also degrades its mechanical properties at higher temperatures. Additionally, PDMS exhibits inferior gas barrier properties, which can limit its applicability in PAMs that require air tightness and pressure control. In this work, PDMS is combined with Ecoflex-30, which has higher tensile strength and tear resistance, to enhance the overall mechanical properties of the resulting material, making it more durable

and able to tolerate repeated cycles of inflation and deflation without tearing or degrading [78,79].

2. The braided sleeving selected for the fabrication of the optimized MPAMs is composed of PET (polyethylene terephthalate) braided sleeves manufactured by the TechFlex® company. PET is frequently chosen as the braid material in PAMs due to its numerous advantageous properties. PET is a robust and long-lasting material that is resistant to wear and tear, as well as being able to endure high temperatures and UV radiation. Additionally, it is resistant to chemicals and abrasions, making it an ideal choice for PAMs. PET braid sleeves are lightweight and do not significantly increase the weight of MPAMs, which is of great importance in miniaturized biomedical applications. Furthermore, PET is affordable and widely accessible, making it a popular material for use in PAMs. Most importantly, PET braid sleeves are highly flexible, enabling them to expand and contract with the muscle as it moves, thus allowing for ease of installation on the muscle.
3. The selection of end-fittings is based on their compatibility with the geometry and material of the bladder to create a secure seal that does not cause damage to the thin bladder designed in this work. The fittings must also be easy to install and cost-effective.

4.2.2 Assembly of the MPAM Actuator

To assemble the actuator, a customized bladder is required to be fabricated with optimal dimensions found previously. Therefore, a tailored mold, which is shown in Fig. (4.2), is initially designed in SolidWorks (as illustrated in Fig. (4.1)) to be 3D-printed utilizing FormLabs, Form 3+ SLA printer with 25μ accuracy, and Clear B4 resin. Stereolithography (SLA) 3D printers utilize photopolymerization to create objects using liquid resins. To fabricate a bladder with a 6 mm outer diameter, the mold comprises two outer halves with a semi-circular groove with an inner diameter of 3 mm and one inner solid cylinder with a diameter of 4.6 mm. Since the equipment available for the experiment has limited accuracy, the optimal thickness of the bladder is set to 0.7 mm instead of 0.67621 mm, hence, the diameter of the inner cylinder, which matches the inner diameter of the bladder is set to 4.6 mm to yield a tube with the required thickness (0.7 mm). The embedded holes on each part of the mold are used to attach these parts using screws. The current design for the mold simplifies the assembly process and also contributes to the overall stability and precision

of the mold during printing and subsequent usage. The length of the bladder is set to 50 mm for miniaturization purposes, but the mold is fabricated with a length of approximately 60 mm to consider the overlapping of the bladder ends with the fittings. After the fabrication of the mold, the material of the bladder is prepared by thoroughly mixing parts A and B (1:1) of Ecoflex-50 silicone (Smooth-On, Inc) for 40 seconds inside a vacuum mixer (Thinky, ARV-200) with a speed of 2000 rpm and under 27 inHg of pressure to remove all air bubbles. After the injection of the silicone mixture into the mold (the cavity between the outer and inner cylinder), it is cured for 24 hours at room temperature to create a cylindrical tube for the bladder. Another bladder is also fabricated using the same mold and procedure, but a different silicone mixture (PDMS + Ecoflex-30 (1:10)). This silicone mixture is cured at 200°F in the oven for 24 hours. Fig. (4.3) depicts the process of fabricating the customized bladders.

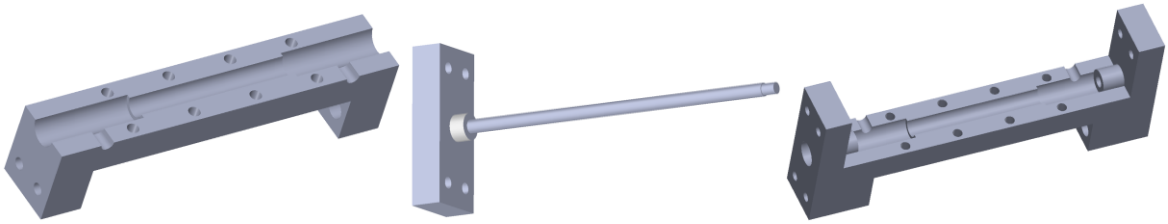

Figure 4.1: Sketch of the mold designed in SolidWorks

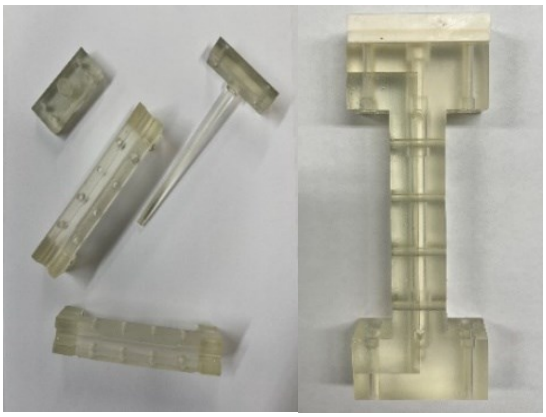

Figure 4.2: 3D-printed mold

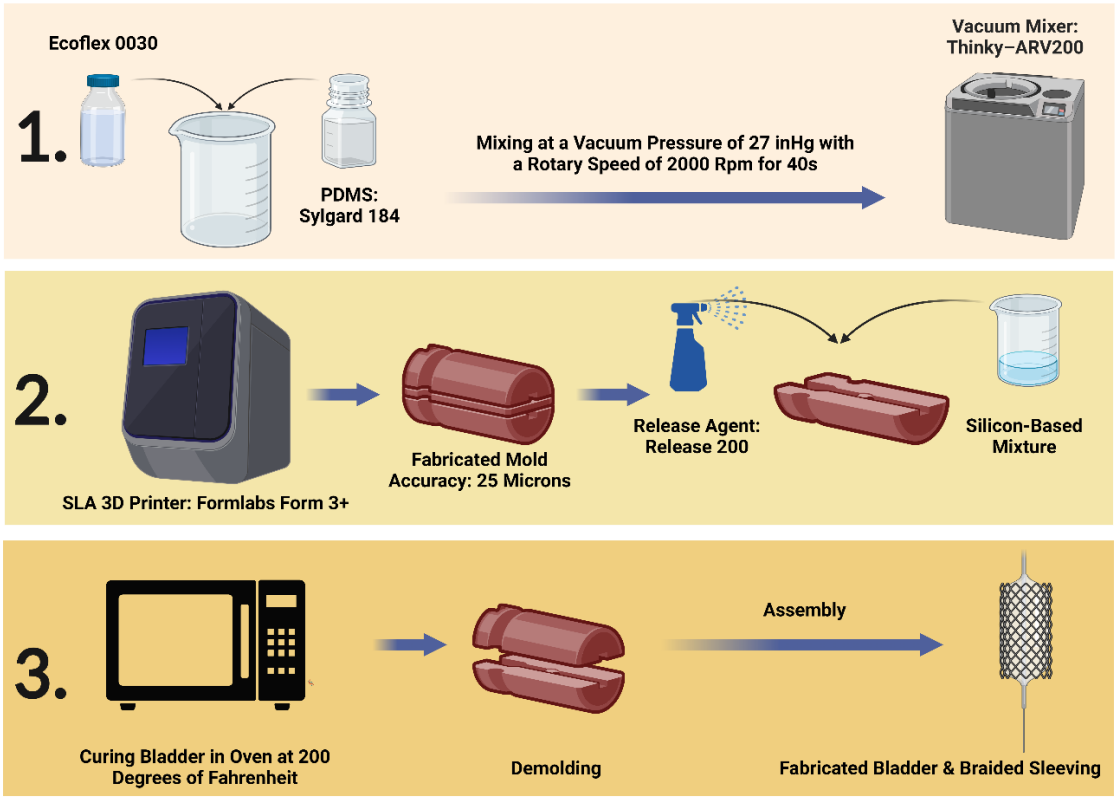

Figure 4.3: Process of fabricating the customized bladder (Ecoflex-30 + PDMS)

The braided sleeving with a nominal diameter of 6.35 mm and a braid angle of 72 degrees was selected after purchasing various PET braids from the supplier and measuring their respective braid angles (TechFlex® - Clean Cut (CCP0.25BK)). To completely cover the bladder, the braid is then cut to the same length as the silicone tube. The ending of the braided sleeving is burned to avoid fraying. Finally, two end fittings are tightly inserted into the bladder's inner diameter to seal the ends of the MPAM. The different components of the MPAM and its assembled configuration can be observed in Fig. (4.4) and Fig. (4.5), respectively.

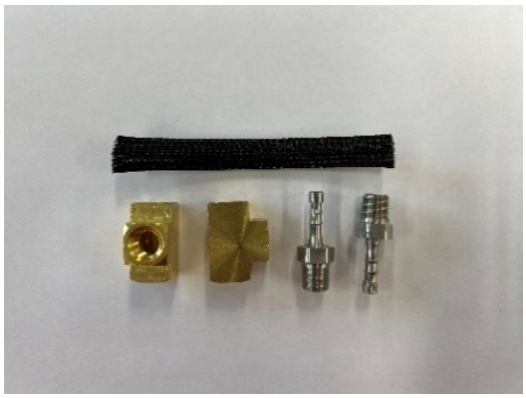

Figure 4.4: Various components of the MPAM

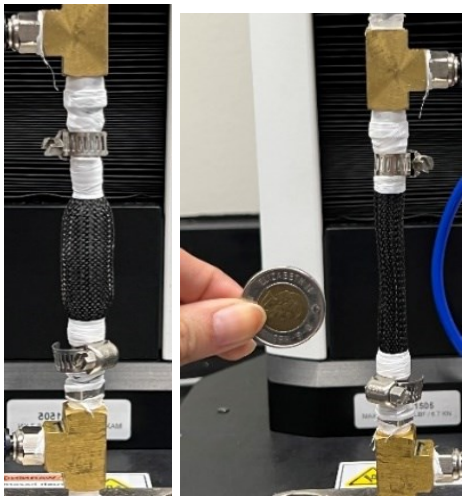

(a) (b)

Figure 4.5: (a) Contracted MPAM under the pressure of 200 kPa (b) MPAM at its initial state

4.3 Test Setup and Procedure

The aim of the experimental setup is to validate the model and optimization results while evaluating the performance of the fabricated MPAMs under varying inlet pressure. Additionally, the hysteresis loops obtained experimentally are effectively utilized to obtain the correction terms necessary for the precise force equation. The quasi-static tests are conducted using an MTS machine (F1505, maximum load of 6.7 kN), capable of measuring both force and displacement (sensor mark-10, model FS05-50, max load 250 N, accuracy $\pm 0.1\%$), along with a pressure sensor

(Festo®, SPAU-P10R-H-G18FD-L-PNLK-PNVBA-M12U, max load 1500 kPa, accuracy $\pm 1.5\%$ FS) to monitor the supplied pressure to the actuator. Fig. (4.6) depicts the MPAM installed within the test setup.

In the initial step, the aim is to measure the blocked force under various constant pressures to validate the theoretical results. For this purpose, both MTS grippers are fixed throughout the experiment to maintain the MPAM at its initial state. First, the inlet pressure is increased gradually from 0 kPa to the state where the MPAM starts producing force, referred to as the dead-band pressure, which is attributed to the nonlinearity of the bladder material that results in a discontinuity in the relationship between the pressure and the diameter, hence, a sudden inflation above a specific pressure [74]. Then, the tests are carried out at various pressures ranging from 20 kPa to 300 kPa with increments of 20 kPa to determine the blocked force as a function of pressure. In each case, the pressure is maintained constant and the readings from the force sensor are recorded as the magnitude of the blocked force. To evaluate the repeatability and reliability of the measurements, each test is performed three times and the average of the recorded data is then utilized to determine the relationship between the air pressure and the blocked force. The same procedure is repeated for each sample of the MPAM to compare the force output of both MPAMs and investigate the impact of the bladder material on the blocked force and the dead-band pressure.

Once the amounts of blocked force are recorded for each particular pressure, the upper MTS grips are unlocked to allow the MPAM to contract freely until it reaches its maximum contraction state, where it stops producing force. At this point, the variation in the initial length of the actuator is recorded as the amount of the free contraction for the MPAM. The free contraction of the MPAM is then measured under various pressures, ranging from 50 kPa to 250 kPa with increments of 50 kPa to determine the correlation between the free contraction and the inlet pressure. Additionally, the variations of the generated force during loading and unloading cycles with respect to the contraction of the actuator are recorded to obtain the hysteresis loops for each MPAM. The hysteresis loops are then used to determine the correction terms concerning the nonlinearity of the MPAM and friction between its components.

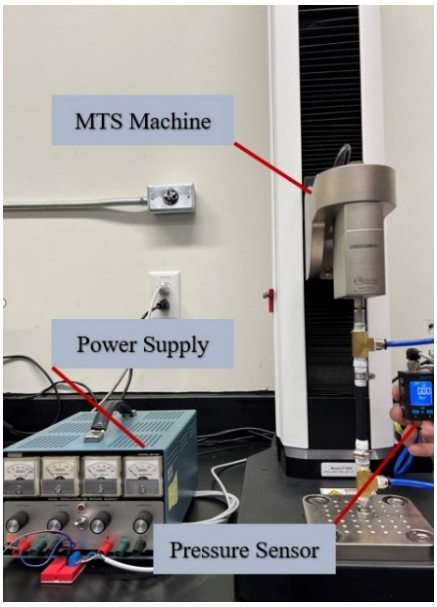

Figure 4.6: Experimental setup

4.4 Blocked Force Measurements

The findings from the quasi-static tests conducted on the two MPAMs under different internal pressures are presented in Fig. (4.7). MPAM_1, featuring the MPAM fabricated with Ecoflex-50 bladder, initiates force generation at an inlet pressure of 20 kPa whereas MPAM_2, which refers to the other MPAM fabricated with a bladder made of PDMS and Ecoflex-30, generates a negligible blocked force at this pressure. The minimum pressure required to initiate force generation in an MPAM is referred to as the dead-band pressure, which is dependent on the bladder's material as well as its thickness and diameter. Previous research by Pillsbury et al. [55] revealed that PAMs with higher volume ratios ($\frac{V_{bl}}{V}$) necessitate higher pressures (i.e., higher P_{DB}) to generate an equivalent amount of force as PAMs with lower volume ratios. The bladder-to-PAM volume ratio is directly proportional to the ratio between the thickness and radius of the bladder, implying that increased bladder thickness can result in higher dead-band pressure. This can be explained due to the fact that a greater force is required to overcome the elasticity of a thick bladder during its deformation. Both optimized MPAMs in this study feature extremely small thickness-to-radius ratios, resulting in significantly lower dead-band pressures and higher force outputs at lower pressures, thereby, reducing the required energy input. Nonetheless, a comparison of the blocked

force generated by both MPAMs at the initial pressure (20 kPa) demonstrates that $MPAM_2$ has a higher dead-band pressure, making $MPAM_1$ more suitable for applications that prioritize low pressure and energy input.

Results indicate that the blocked force exhibits a linear relationship with pressure, consistent with results in Chapter 3 and prior studies [2-5,39-42,55]. Both MPAMs exhibit almost identical force output, with $MPAM_2$ generating higher blocked force when the pressure is increased beyond 150 kPa. Due to the presence of imperfections in the tubular silicone and MTS machine limitations, the maximum pressure is limited to 300 kPa, yielding a maximum blocked force of 120 N and 136 N for $MPAM_1$ and $MPAM_2$, respectively. This pressure (i.e. 300 kPa) displays the largest deviation between the output of the MPAMs, with $MPAM_2$ achieving a blocked force approximately 16 % higher than $MPAM_1$. The optimal blocked force obtained from Eq. (3.16) agrees exceptionally well with the experimental data for both MPAMs, particularly at lower pressures, as shown in Fig. (4.7). Fig. (4.8) illustrates that the overall error between simulated and experimental blocked forces under different pressures remain below 10% for both MPAMs. It should be noted that the absence of dead-band pressure in the theoretical force equation results in the largest errors between the simulation and experiment occurring at the inlet pressure of 20 kPa, which is the starting point for force generation in $MPAM_1$. On the other hand, the significant deviation of almost 38% between the theoretical and experimental blocked forces generated by $MPAM_2$ at 20 kPa suggests the presence of a higher dead-band pressure for this actuator. Additionally, comparing the overall errors between the simulated and experimental results from both MPAMs indicates that the behaviour of $MPAM_1$ is better anticipated using the theoretical force equation derived in Eq. (3.16), which is likely due to the effects of neglecting dead-band pressure. The minor inconsistencies between the experimental and theoretical results can be attributed to the fabrication and testing limitations, as well as the assumptions made during the derivation of the optimization formulation.

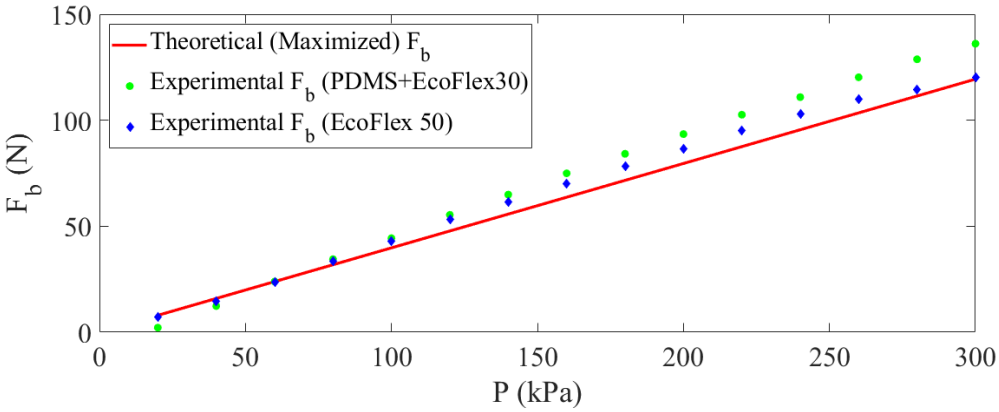

Figure 4.7: Comparison between the experimental and theoretical results

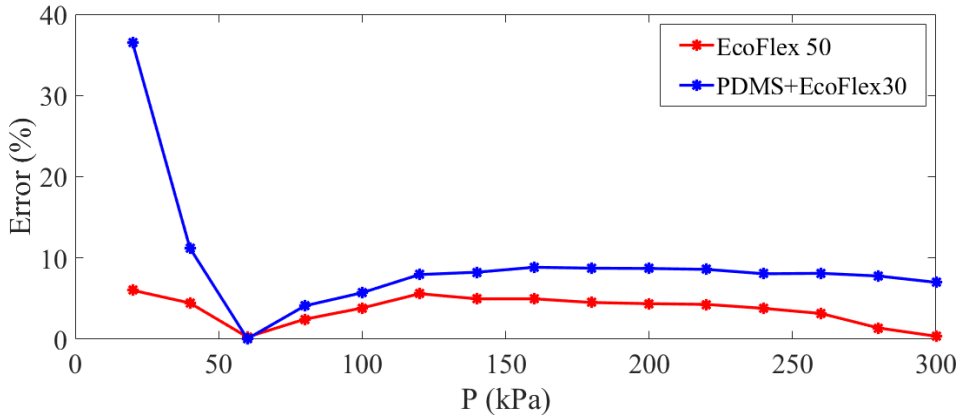

Figure 4.8: The error between the experimental data and the optimized blocked force

In order to further validate the conclusion drawn from Fig. (3.2), the optimized parameters are employed as inputs in three distinct force models (G: simple Gaylord, G + t: Gaylord including the effects of the thickness of the bladder, G + t + b: Gaylord including the effects of the thickness of the bladder and the energy stored in the braided sleeving). Fig. (4.9) compares the theoretical values of the blocked force obtained using the aforementioned force models with the experimental data. The results confirm that the Gaylord model overestimates the blocked force in comparison to the other two equations. This observation is consistent with the previous studies [2,25,38-40], which have highlighted the limitations of the simple Gaylord model in accurately predicting the force output of PAMs. Furthermore, the results support the conclusions drawn from Fig. (3.2)

regarding the negligible discrepancy between force estimations using the second and third force equations.

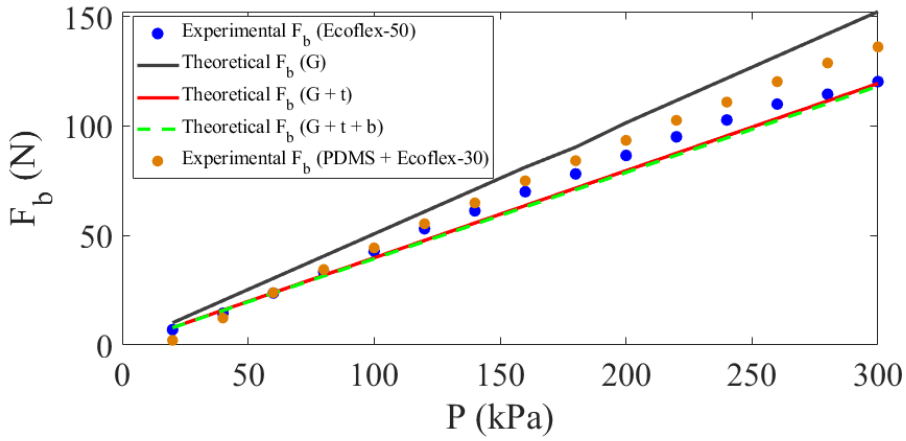

Figure 4.9: Comparison between the anticipated amounts of blocked force using various force models and experimental data

4.5 Free Contraction Measurements

In addition to the blocked force, the performance evaluation of an MPAM involves the free contraction which is also an important parameter. In order to investigate the influence of inlet pressure on the free contraction of the MPAM, a dimensionless parameter is defined as:

$$\text{Contraction ratio} = \gamma = \frac{\Delta L}{L_0} \tag{4.1}$$

where L_0 is the initial active length of the actuator and ΔL is the amount of change in length. Fig. (4.10) illustrates the variation of the free contraction ratio with respect to the inlet pressure for both MPAMs. The results demonstrate that the contraction ratio increases nonlinearly as the inlet pressure rises, consistent with the trends reported in prior studies [2, 39]. Notably, MPAM_1 exhibits significantly higher free contractions, nearly 1.5 times, than the other MPAM, particularly at lower pressures, making it a more desirable option for applications that require greater contractions. It is interesting to note that as the pressure increases, the contraction ratios increase at a slower rate, suggesting that the free contraction of both MPAMs reaches saturation at high inlet pressures. This trend is particularly significant for MPAM_1, which experiences a sharp rise in the contraction ratio as the pressure increases from 50 kPa to 100 kPa, but the rate of increase slows considerably

between 100 kPa and 250 kPa for this MPAM due to the fact that the diameter of the bladder cannot expand beyond a certain value.

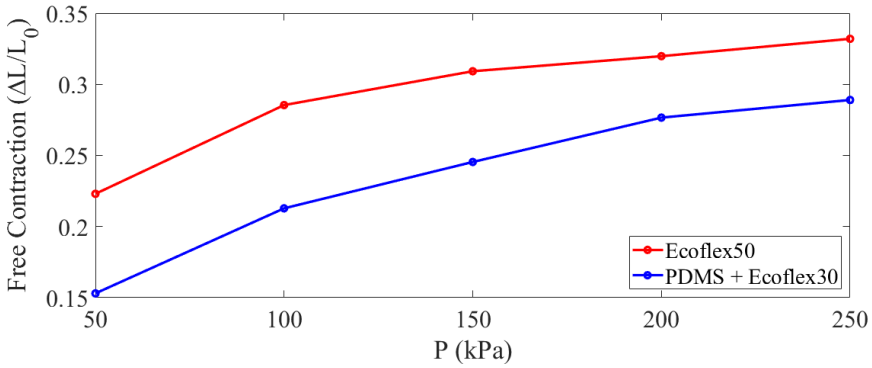

Figure 4.10: Free contraction as a function of pressure

4.6 Nonlinear Hysteresis Loops

The process of obtaining the hysteresis loops in this study involves using IntelliMESUR ®, which is a motion control and data acquisition software integrated within the MTS machine. As mentioned in section 4.3, the hysteresis loops for each MPAM are obtained by first unlocking the upper MTS grips and allowing the MPAM to contract up to its free contraction state. At this point, the variation in the length of the actuator is recorded and inputted into the software as the maximum contraction that the MPAM can have while it is being loaded. The MPAM is then subjected to loading and unloading cycles at a constant speed of 50 mm/min until it returns to its initial state, with the force and distance being recorded in increments of 0.01 seconds. The loading and unloading cycles are repeated at different inlet pressures to obtain the hysteresis loops at each pressure. The hysteresis loops provide valuable information regarding the behaviour of the MPAMs under various pressures, and their acquisition is critical to find the correction terms due to the nonlinearity of the bladder material and friction in the braiding sleeve required for the modified force model of the PAMs as discussed in Chapter 2. The use of the integrated IntelliMESUR ® enables precise control over the motion of the actuator, which ensures that the data is collected with a high degree of accuracy, thus ensuring their reliability.

By performing these experiments at various inlet pressures, we can obtain a comprehensive understanding of how the properties of the MPAMs change with variations in inlet pressure. The

hysteresis loops are then utilized to derive correction terms for the nonlinear stress-strain behaviour of the MPAMs and to find a friction term that enables the theoretical force equation to accurately predict the observed hysteresis in force-contraction relationships of the actuators. The derivation of each of these correction terms is explained in the following sections.

4.6.1 Nonlinear Behaviour of the MPAM

As explained in section 2.3.1, the bladder is modeled as a nonlinear elastic material, and its stress-strain relationship is represented by a polynomial function as given in Eq. (2.12). This polynomial function is then incorporated into a refined force model (Eq. (2.17)) to accurately capture the nonlinear behaviour of the MPAM. Here in this research study, two methods are presented to empirically obtain modulus values (E_k) and the degree of the polynomial relationship between the stress and strain (M) which are included in Eq. (2.12). The first method involves the stress-strain relationship defined using the tensile tests conducted on the bladder's material, while the second method defines the nonlinear term based on the force-contraction tests on the whole actuator. By making a comparison between these methods, an accurate correction term is found to take the nonlinear behaviour of the MPAM into account. Hence, more accurate and detailed information about the mechanical behaviour of the MPAM is obtained, which in turn enhances our understanding of the overall performance of the MPAM. Each of the proposed methods is described in the following sections.

4.6.1.1 Evaluation of Modulus Values by Testing the Bladder Material (Ecoflex-50):

This method involves conducting tensile tests on a sample of the bladder material utilizing an MTS machine which is equipped to record the force applied to the material and its corresponding deformation. The empirical data obtained from these tests are used to calculate the stress and strain of the material as:

$$\sigma = \frac{F}{A} \tag{4.2}$$

$$\varepsilon = \frac{\Delta L}{L} \tag{4.3}$$

where F and ΔL, representing the force and deformation respectively, are obtained from the tensile tests, while A and L, showing the area and the length, are known from the initial dimensions of the

Ecoflex-50 sample which is being tested. Fig. (4.11) illustrates the relationship between stress and strain during the tensile deformation process. A second-order polynomial function, as given in Eq. (4.4), provides an accurate representation of the relationship between stress and strain for the bladder material. The modulus values are obtained using error minimization between the function and experimental data and are listed in Table (4.1).

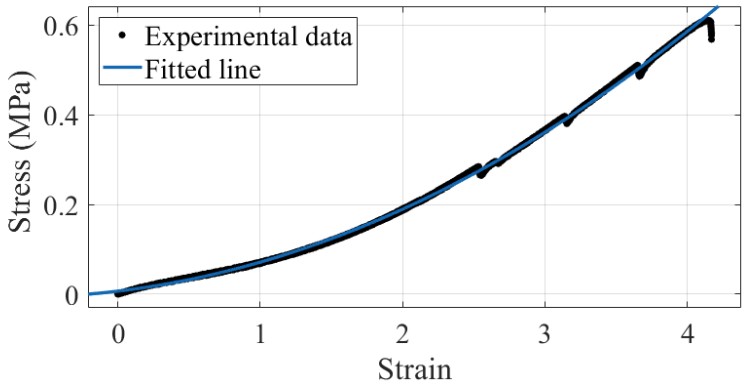

Figure 4.11: Stress vs. strain relationship for Ecoflex-50

$$\sigma = \sum_{k=1}^{2} E_k \varepsilon^k \tag{4.4}$$

Table 4.1: E_k obtained from the tensile tests conducted on Ecoflex-50

Modulus of elasticity (Pa)	
$\boldsymbol{E_1}$	3.769×10^4
$\boldsymbol{E_2}$	2.676×10^4

4.6.1.2 Evaluation of Modulus Values by Testing the MPAM:

The previous method for determining the elasticity moduli of the bladder material was limited to only one component of the MPAM, ignoring the potential influence of other components on the actuator's nonlinear behaviour. Therefore, a second method is developed to investigate the elastic moduli of the entire structure. To achieve this, the force-contraction loops during a loading and

unloading cycle for $MPAM_1$ are obtained (Fig. (4.12)). These loops represent the relationship between the force applied to the MPAM and the corresponding displacement of the actuator in loading and unloading.

The order of the material (M) and modulus values (E_k) are obtained by minimizing the least square error between the theoretical force obtained from Eq. (2.17) and the average experimental forces represented by the dashed lines in Fig. (4.12). The minimization process is conducted using the MATLAB® optimization toolbox, with a standard optimization formulation defined as Eq. (4.5). The minimization process initiates by assuming that M = 1 and iteratively increases the order of the polynomial function until the best-fit curve for the MPAM's nonlinear behaviour is achieved.

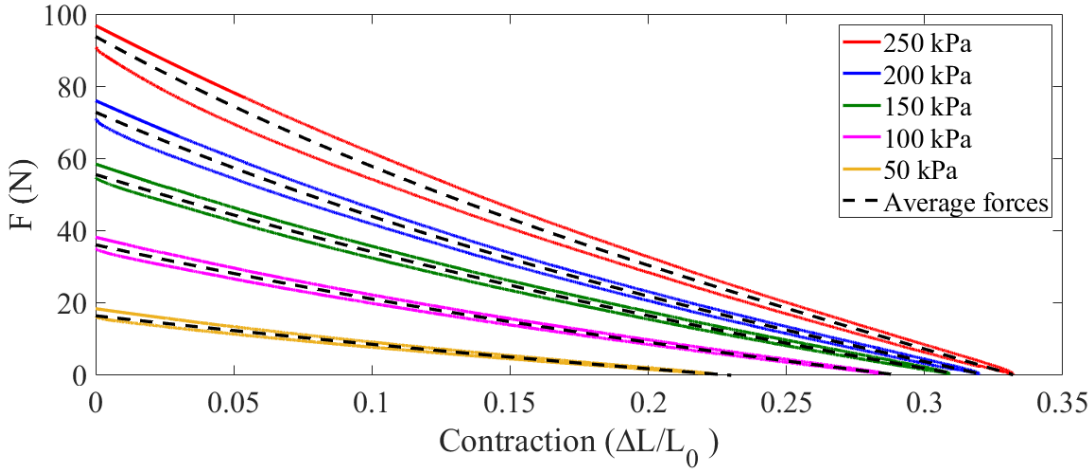

Figure 4.12: Force Vs. Contraction for $MPAM_1$

Knowing that:

$$F_{th} = \frac{P}{4N^2\pi}(3L^2 - B^2) + P(\frac{V_{bl}}{L} - \frac{tL^2}{2\pi N^2 R}) + \frac{V_{bl}}{L}\sum_{k=1}^{M} E_k(\frac{L}{L_0} - 1)^k$$
$$- \frac{tL^2}{2\pi N^2 R}\sum_{k=1}^{M} E_k(\frac{R}{R_0} - 1)^k \qquad (4.5)$$

Find E_k to Minimize:

$$\text{Least Sqare Error } = \sum_i (\frac{F_{th} - F_{avg}}{F_{avg}})^2 \ ;$$

Fig. (4.13) compares the theoretical force obtained from various force equations with the average amount of experimental force obtained from hysteresis tests conducted on MPAM_1 at 200 kPa. The results indicate that the simplified force equation, which considers only the effects of the bladder's thickness but neglects the nonlinearities, underestimates the force outputs. Additionally, correcting the force model based on the modulus values obtained from the first method is not sufficient to enhance the accuracy of the equation since it only accounts for the elastic moduli of the bladder, while the braided sleeving woven around the bladder also contributes to the nonlinearity observed in the force-contraction curves of an MPAM. Consequently, the empirical data obtained from the hysteresis of the MPAM are necessary to derive the modulus values and the order of the polynomial stress-strain relationship applicable to the MPAM. The polynomial order is increased until the error between the experimental and theoretical data is minimized. Fig. (4.13) illustrates that a fourth-degree polynomial stress-strain relationship accurately captures the MPAM's elasticity, and further increasing the order to 5 does not improve the results. The same conclusion can be derived from an analysis of the coefficient of determination for each equation, as presented in Table (4.2). The coefficients demonstrate that both the 4th-degree and 5th-degree polynomial functions exhibit equivalent precision in predicting the force generated by the MPAM. It is noteworthy that the values of E_k are dependent on the inlet pressure and have been determined for each specific inlet pressure, as reported in Table (4.3).

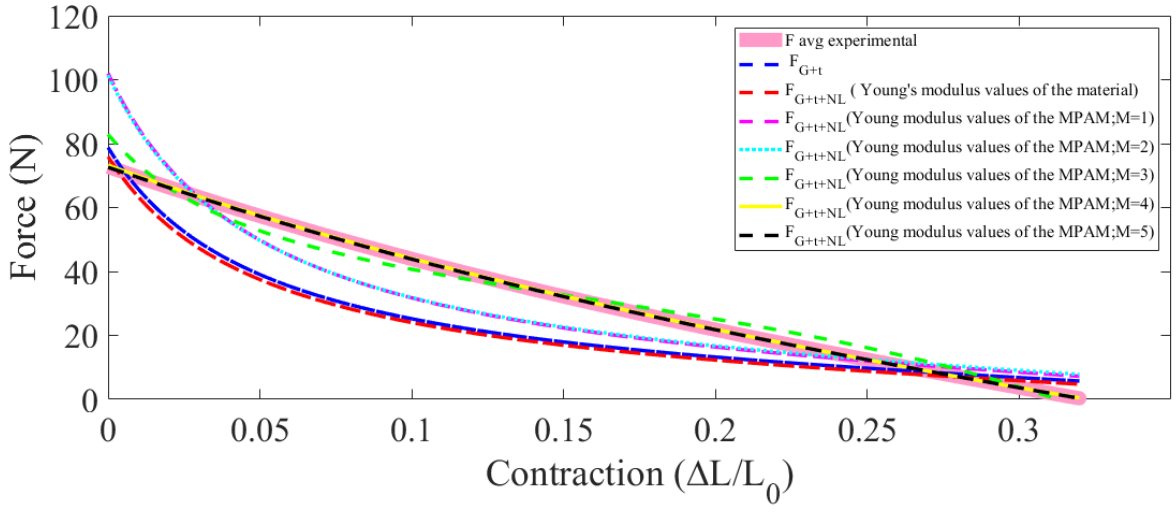

Figure 4.13: Comparison between the amounts of force calculated using different force equations and the average experimental force at 200 kPa (MPAM_1)

Table 4.2: Coefficient of determination (R^2) for each force equation at 200 kPa ($MPAM_1$)

Force model	F_{G+t}	F_{G+t+NL} (E_k of the material)	F_{G+t+NL} (E_k of the MPAM, M=1)	F_{G+t+NL} (E_k of the MPAM, M=2)	F_{G+t+NL} (E_k of the MPAM, M=3)	F_{G+t+NL} (E_k of the MPAM, M=4)	F_{G+t+NL} (E_k of the MPAM, M=5)
R^2	0.8838	0.8868	0.8784	0.8771	0.9780	0.9955	0.9955

Table 4.3: E_k at each inlet pressure for $MPAM_1$

P (kPa)	**E_1 (Pa)**	**E_2 (Pa)**	**E_3 (Pa)**	**E_4 (Pa)**
50	4.6791×10^7	-1.0822×10^8	7.8137×10^7	-1.0822×10^8
100	9.2886×10^7	-2.1444×10^8	1.5480×10^8	-3.3207×10^7
150	1.4356×10^8	-3.3089×10^8	2.3844×10^8	-5.1072×10^7
200	1.7603×10^8	-4.0556×10^8	2.9214×10^8	-6.2561×10^7
250	2.1824×10^8	-5.0125×10^8	3.5947×10^8	-7.6423×10^7

The E_k values obtained for each inlet pressure are used to derive the modified force equation, including the effects of nonlinearity of the MPAM as given in Eq. (4.6). The accuracy of the modified equation is then evaluated by comparing the force-contraction relationships predicted using Eq. (4.6) and the E_k values from Table (4.3) with the experimental force data as displayed in Fig. (4.14). The results illustrate that Eq. (4.6) accurately anticipates the average amount of force produced by the MPAM during loading and unloading between its initial and free contraction states.

$$F_{th} = P\pi\left[R^2(2tan^2(\alpha)-1) + (2Rt - t^2) - 2tR(tan^2(\alpha))\right] + \frac{V_{bl}}{L}\sum_{k=1}^{4} E_k\left(\frac{L}{L_0} - 1\right)^k - \frac{tL^2}{2\pi N^2 R}\sum_{k=1}^{4} E_k\left(\frac{R}{R_0} - 1\right)^k \quad (4.6)$$

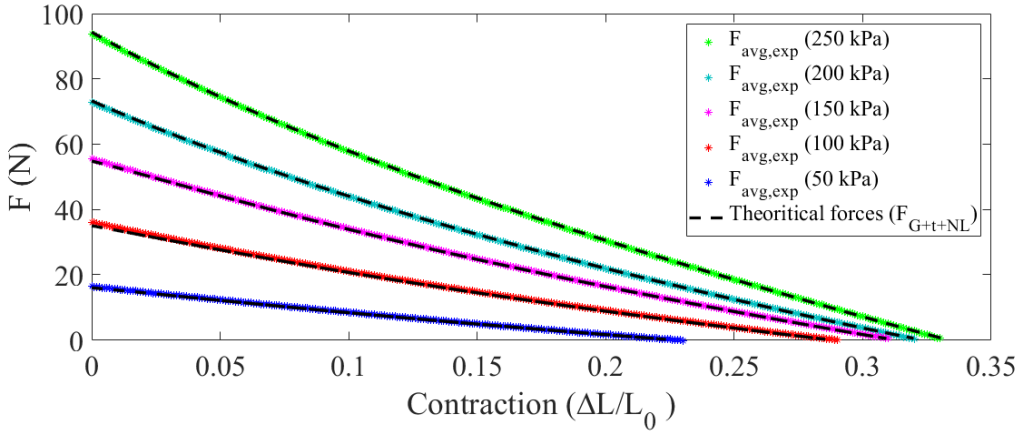

Figure 4.14: Average experimental force compared to the theoretical forces using the equation including the elasticity of $MPAM_1$

The variations in the E_k values with respect to an increase in the inlet pressure are further analyzed and illustrated in Fig. (4.15). Results show that E_1 and E_3 exhibit an almost linear increase with increasing pressure, while E_2 and E_4 decrease almost linearly, with E_4 showing a relatively smaller decline. To facilitate the determination of these parameters at other pressures, a linear relationship between each modulus and the pressure is presented in Eq. (4.7). The constant coefficients in Eq. (4.7) have been determined for each specific E_k, as reported in Table (4.4). The dashed lines in Fig. (4.15) represent the anticipated values of E_k, thereby highlighting the accuracy of Eq. (4.7) in determining the elasticity moduli of the designed MPAM. This is further supported by the coefficient of determination of the proposed equation for each E_k, as reported in Table (4.5). This approach reduces the requirement for additional force-contraction empirical data at each distinct pressure. The resulting equation provides a practical means to estimate the values of the elastic moduli for a wide range of operating conditions.

$$E\ (P) = aP + b \tag{4.7}$$

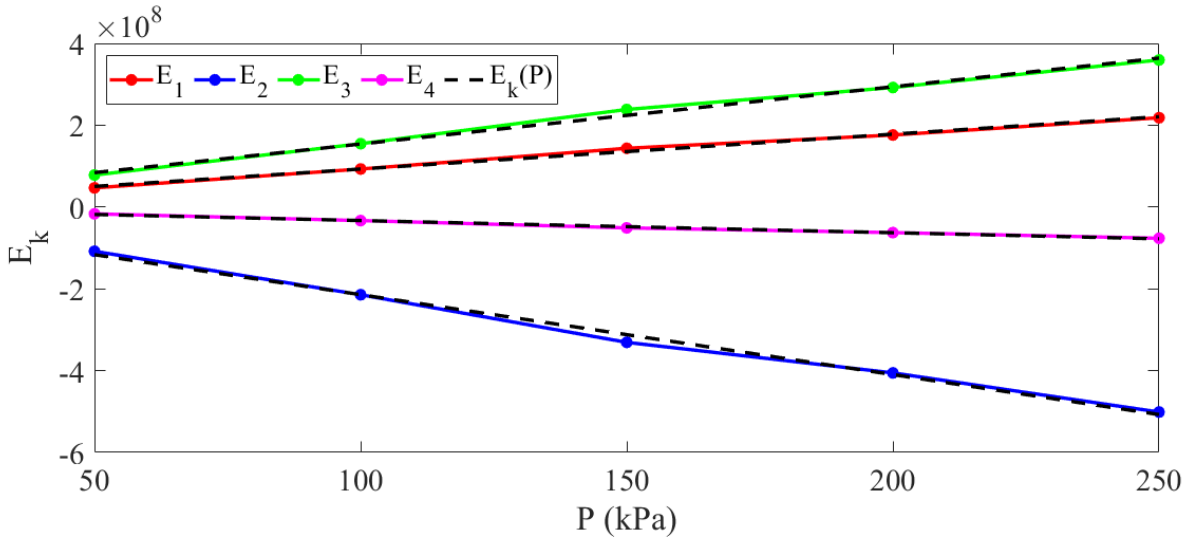

Figure 4.15: Variations in E_k with the inlet pressure ($MPAM_1$)

Table 4.4: The values of each constant utilized in Eq. (4.7) for E_k

	E_1	E_2	E_3	E_4
a	8.521e+05	-1.954e+06	1.4e+06	-2.977e+05
b	7.689e+06	-1.892e+07	1.46e+07	-3.333e+06

Table 4.5: Coefficient of determination of Eq. (4.7) for E_k

	E_1	E_2	E_3	E_4
R^2	0.9952	0.9950	0.9946	0.9938

The insufficiency of the first method, which focuses solely on the bladder material, in providing accurate results for the nonlinear correction term of MPAMs has led to the adoption of the second method to obtain the polynomial stress-strain function for $MPAM_2$. To accomplish this, the

hysteresis loops for $MPAM_2$ are studied, as shown in Fig. (4.16), and utilized to determine the average experimental forces at different inlet pressures. These forces are then used in the least square error minimization method, defined in Eq. (4.5). Fig. (4.17) presents a comparison between the theoretical and experimental forces at 200 kPa, indicating that a five-degree polynomial stress-strain function is required to accurately predict the nonlinear behaviour of $MPAM_2$ fabricated with a PDMS + Ecoflex30 bladder. The coefficients of determination of each force equation are also reported in Table (4.6), demonstrating that the 5-degree polynomial function exhibits the highest level of accuracy, surpassing even the 6-degree polynomial function. Furthermore, the elasticity moduli for each operating pressure are reported in Table (4.7).

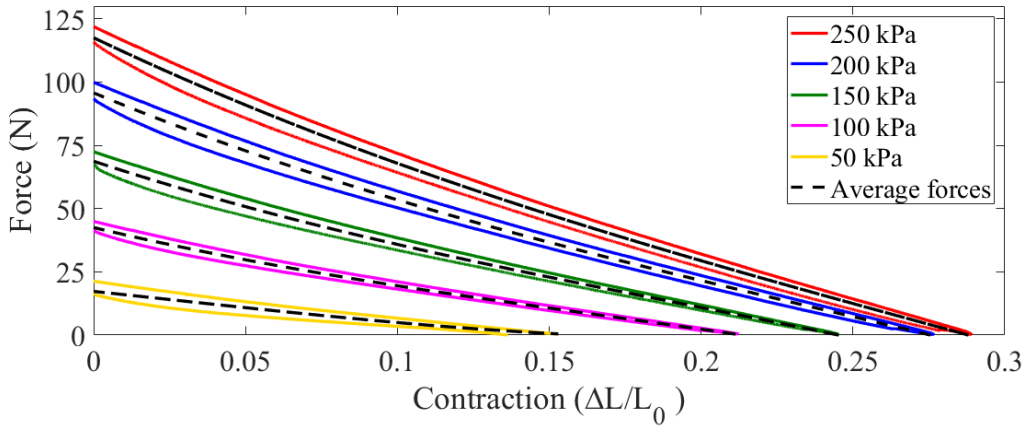

Figure 4.16: Force Vs. Contraction for $MPAM_2$

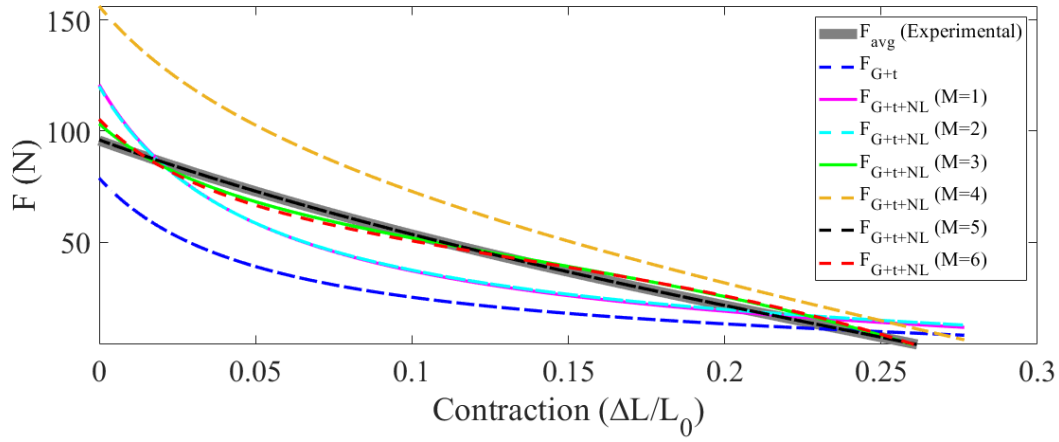

Figure 4.17: Comparison between the amounts of force calculated using different force equations and the average experimental force at 200 kPa ($MPAM_2$)

Table 4.6: Coefficient of determination (R^2) for each force equation at 200 kPa ($MPAM_2$)

Force model	F_{G+t}	F_{G+t+NL} (E_k of the MPAM, M=1)	F_{G+t+NL} (E_k of the MPAM, M=2)	F_{G+t+NL} (E_k of the MPAM, M=3)	F_{G+t+NL} (E_k of the MPAM, M=4)	F_{G+t+NL} (E_k of the MPAM, M=5)	F_{G+t+NL} (E_k of the MPAM, M=6)
R^2	0.8879	0.8815	0.8797	0.9858	0.9819	0.9935	0.9822

Table 4.7: E_k at each inlet pressure for $MPAM_2$

P (kPa)	**E_1 (Pa)**	**E_2 (Pa)**	**E_3 (Pa)**	**E_4 (Pa)**	**E_5 (Pa)**
50	-5.8122×10^4	7.5506×10^5	-1.9064×10^6	1.4114×10^6	-2.0814×10^5
100	2.1223×10^8	-6.4210×10^8	7.3562×10^8	-3.8947×10^8	8.3694×10^7
150	2.3075×10^8	-6.1615×10^8	5.9366×10^8	-2.5431×10^8	4.5917×10^7
200	2.6883×10^8	-6.6105×10^8	5.4863×10^8	-1.7853×10^8	2.1968×10^7
250	3.0780×10^8	-7.2566×10^8	5.5050×10^8	-1.4134×10^8	8.5317×10^6

In order to evaluate the accuracy of the modified force equation, the modified force equation with the integrated 5-degree polynomial function is used to predict the force output of $MPAM_2$, and the results are then compared to the average experimental forces. The comparison, as shown in Fig. (4.18), indicates that the modified force equation accurately predicts the average force output of the $MPAM_2$. It should be noted that the highest discrepancy between the theoretical and experimental data is observed at 50 kPa likely due to the absence of the effect of dead-band pressure in the theoretical model.

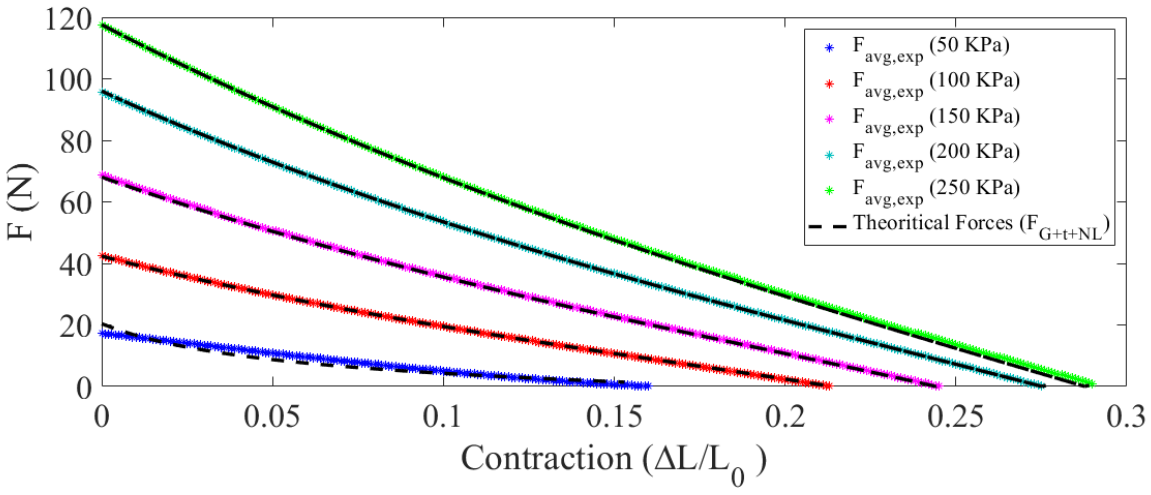

Figure 4.18: Average experimental force compared to the theoretical forces using the equation including the elasticity of $MPAM_2$

Furthermore, Fig. (4.19) displays the relationship between the elasticity modulus (E_k) and the inlet pressure, where the actual values are presented using circles. It is observed that between 50 kPa and 100 kPa of inlet pressure, there is a sharp increase or decrease in the E_k values. However, at pressures higher than 100 kPa, the values for E_k slightly change (saturation). This behaviour can be explained by the characteristics of the materials of the $MPAM_2$, and their underlying physical properties. PDMS and Ecoflex-30, as elastomers, exhibit nonlinear stress-strain relationships, and their mechanical properties are influenced by cross-linking, which refers to the formation of chemical bonds between polymer chains. Higher pressures induce a structural rearrangement and more efficient cross-linking. Consequently, the plateau after 100 kPa indicates a well-established cross-linking network where further pressure has minimal effect on the elasticity.

The phenomenological model presented in Eq. (4.8) is also proposed based on the trend observed in Fig. (4.19), capturing the variations in E_k with increasing pressure. This equation provides an estimation of E_k at various inlet pressures without requiring additional empirical data. Each line in Fig. (4.19) represents the predicted values of E_k using the proposed model, which are further validated by the high coefficients of determination reported in Table (4.8). The constants utilized in Eq. (4.8) are specific to each E_k, and their corresponding values are documented in Table (4.9).

$$E\ (P) = c(\exp(dP)) + w(\exp(zP)) \tag{4.8}$$

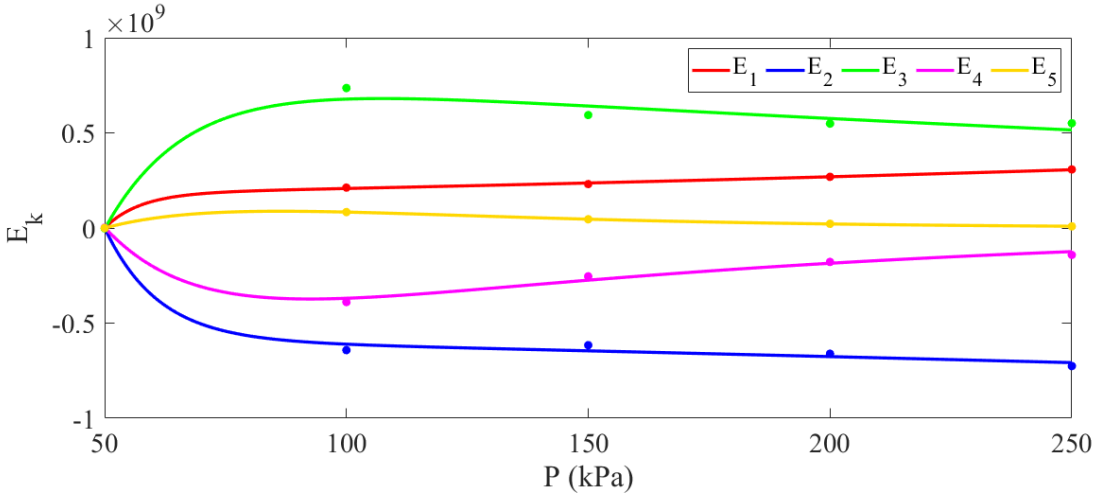

Figure 4.19: Variations in each E_k based on the inlet pressure ($MPAM_2$)

Table 4.8: Coefficients of determination for Eq. (4.8) and each E_k

	E_1	E_2	E_3	E_4	E_5
R^2	0.9990	0.9942	0.9861	0.9953	0.9997

Table 4.9: The values of each constant utilized in Eq. (4.8) for E_k

	E_1	E_2	E_3	E_4	E_5
c	1.605×10^{8}	-5.623×10^{8}	8.668×10^{8}	-7.968×10^{8}	6.334×10^{8}
d	0.002584	0.0009189	-0.002075	-0.00732	-0.01688
w	-5.843×10^{18}	7.14×10^{18}	-1.382×10^{19}	1.699×10^{20}	-2.218×10^{9}
z	-0.4838	-0.4644	-0.4719	-0.529	-0.04192

The polynomial stress-strain functions defined for each MPAM allow the derivation of nonlinear correction terms that consider the elastic behaviour of an MPAM. These correction terms can be

added to the force equation in order to improve its accuracy. The modified force equation is given as follows:

$$F_{th} = F_{G+t} + F_{br} + F_{NL} \tag{4.9}$$

It is noted that based on the optimization results and the comparison between the two optimization cases presented in Chapter 3, it has been concluded that neglecting the correction term regarding the energy stored in the braid (F_{br}) would not significantly affect the accuracy of the force equation. Thus, this term is excluded to achieve a simplified optimized design of the MPAM. F_{G+t} represents the force equation that accounts for the thickness of the bladder, as simplified in Eq. (3.16). The nonlinearity correction terms, F_{NL}, presented in Eq. (4.9) can be further simplified using the equations for V_{bl} and N, as shown below:

Knowing that $V_{bl} = \pi L(2Rt - t^2)$ and $N = \frac{Lcot\alpha}{2\pi R}$:

$$\begin{aligned} F_{NL} &= \frac{V_{bl}}{L}\sum_{k=1}^{M} E_k \left(\frac{L}{L_0} - 1\right)^k - \frac{tL^2}{2\pi N^2 R}\sum_{k=1}^{M} E_k \left(\frac{R}{R_0} - 1\right)^k \\ &= \pi(2Rt - t^2)\sum_{k=1}^{M} E_k \left(\frac{L}{L_0} - 1\right)^k - \frac{2\pi Rt}{cot^2(\alpha)}\sum_{k=1}^{M} E_k \left(\frac{R}{R_0} - 1\right)^k \end{aligned} \tag{4.10}$$

In which M and E_k are determined based on the material utilized for fabricating various components of the MPAM. In this thesis, two MPAMs are designed with bladders made of Ecoflex-50 and PDMS + Ecoflex-30. The nonlinear terms can be further simplified using the equation defined for the E_k values and also the polynomial functions established between the stress-strain relationships for each MPAM as:

$$\begin{aligned} F_{NL} &= \pi(2Rt - t^2)\sum_{k=1}^{4} (aP + b)_k \left(\frac{L}{L_0} - 1\right)^k \\ &\quad - \frac{2\pi Rt}{cot^2(\alpha)}\sum_{k=1}^{4} (aP + b)_k \left(\frac{R}{R_0} - 1\right)^k ;\ \text{MPAM}_1 \end{aligned} \tag{4.11}$$

$$F_{NL} = \pi(2Rt - t^2)\sum_{k=1}^{5}(c(exp(dP)) + w(exp(zP)))_k\left(\frac{L}{L_0} - 1\right)^k - \frac{2\pi Rt}{cot^2(\alpha)}\sum_{k=1}^{5}(c(exp(dP)) + w(exp(zP)))_k\left(\frac{R}{R_0} - 1\right)^k ;\ \text{MPAM}_2 \tag{4.12}$$

Based on the analysis conducted, it is evident that MPAM_1 and MPAM_2exhibit different nonlinear behaviours. The comparison of the two actuators indicates that MPAM_1 can be modeled using a four-degree polynomial stress-strain function, while MPAM_2 requires a higher degree polynomial to describe its nonlinear behaviour. This implies that MPAM_2 exhibits more pronounced nonlinearities compared to MPAM_1. Additionally, the elastic moduli of MPAM_1 demonstrate an almost linear relationship with the inlet pressure, indicating that the behaviour of this MPAM can be predicted relatively easily. However, in the case of MPAM_2, the elasticity moduli are exponential functions of the pressure. This makes it more challenging to accurately anticipate the behaviour of MPAM_2 unless certain simplifications are made, such as assuming constant moduli of elasticity for pressures above 100 kPa.

4.6.2. Friction Between the Components of the MPAM

When the MPAM is unloaded, it contracts, resulting in a decrease in length. When loading the muscle, it begins to expand, and its length increases. However, the force required to maintain the contraction at a particular length is less than the force required to maintain the expansion at the same length. This difference in force can be attributed to the hysteresis that exists in the muscle, which is caused by several factors, the most important of which is the frictional loss within the muscle. As described in section 2.3.3, it can be assumed that the static friction between the components of an MPAM only consists of the friction between the braid strands. In this thesis, two methods are proposed to consider the effects of friction on the force output of the MPAMs. In the first method, the theoretical friction force in Eq. (2.43) is used and in the second method, the friction factor in Eq. (2.44) is identified using the experimental data. A comparison is made between the accuracy of the resulting refined force equations to choose the most accurate force model that can accurately capture the force outputs of the MPAM with the minimum error.

4.6.2.1 Theoretical friction term

To account for the friction between the braid fibers of an MPAM, an equation was derived for the theoretical friction term as presented in Eq. (2.43) in Chapter 2. This friction term opposes the motion of the MPAM and must be added to the force equation during expansion, while subtracted from the force equation during contraction of the MPAM. By integrating this friction term with the previously defined force equation presented in Eq. (4.9), a modified force equation that can capture the nonlinear behaviour of the MPAM and predicts the hysteresis observed in the force-contraction loops is expressed as:

$$F_{th} = F_{G+t} + F_{NL} + F_F \text{ ; expansion} \qquad (4.13)$$

$$F_{th} = F_{G+t} + F_{NL} - F_F \text{ ; contraction}$$

The theoretical static friction (F_F) as presented in Eq. (2.43) is expressed as:

$$|F_F| = P \times (f_s) \times 2\pi R_0 L_0 \frac{cos\alpha_0}{\sqrt{1 - sin^2\alpha_0(1-\gamma)^2}} \times \frac{1}{1-\gamma} \times \frac{1}{0.69} \times \left(\frac{P(1-{\nu_s}^2)}{E_{br}}\right)^{1/3} \qquad (4.14)$$

where f_s is the friction factor for the braided strands and is typically reported in the literature to range between 0.15-0.25 for PET braid strands. Other parameters that are included in the modified force equation are the Poisson's ratio of PET braid, ν_s , which is known to be equal to 0.33, and the modulus of elasticity of the braid, E_{br} , which is typically around 2 GPa. The remaining parameters include the initial dimensional parameters ($L_0, t_0, R_0,$ and α_0) as well as the instantaneous parameters (L, R, t, and α). The initial parameters are known from the optimized design of each MPAM, while the instantaneous parameters are obtained as described below:

Knowing that $B_0 = B$ and $L = L_0 \pm \Delta L$ (where ΔL is subtracted from the initial length during contraction while being added to it during expansion), the braid angle can be determined at each state:

$$\frac{L_0}{sin\alpha_0} = \frac{L}{sin\alpha} \rightarrow \alpha = sin^{-1}\left(\frac{Lsin\alpha_0}{L_0}\right) \qquad (4.15)$$

To determine the amount of R after the actuator has been deformed, it is assumed that V_{bl} remains constant and the thickness of the bladder remains unchanged. With the initial dimensions of the MPAMs ($L_0 = 50$ mm; $t = 0.7$ mm; $R_0 = 3$ mm), the value of R can be calculated as follows:

$$V_{bl0} = V_{bl} \rightarrow \pi L_0(R_0^2 - (R_0 - t_0)^2) = \pi L(R^2 - (R - t_0)^2) \tag{4.16}$$

$$185.5 = L(R^2 - (R - 0.7)^2) \rightarrow R = \frac{185.5 + 0.49L}{1.4L}$$

To enhance the accuracy of the refined force model in predicting the force and contraction of the MPAM at each state, the optimized value of f_s is determined by minimizing the least square error between the predicted force value and the experimental force. The variations in the least square error with respect to changes in f_s are illustrated in Fig. (4.20), exhibiting a nonlinear increase in the error when f_s increases. This trend is presented for a pressure of 200 kPa, and similar results are observed for the other inlet pressure. Based on these findings, the value of f_s is set to 0.15 for the remainder of the calculations to improve the accuracy of the resulting force equation.

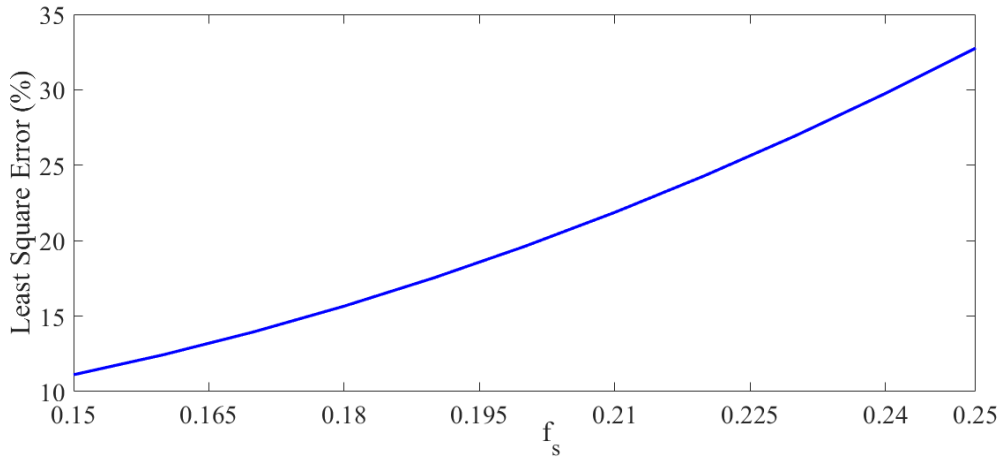

Figure 4.20: Variations in the Least Square Error between the theoretical and experimental forces with changes in f_s (P = 200 kPa)

The force generated by the MPAM at each contraction state and each pressure can be calculated by substituting the values obtained for each dimensional parameter from Eqs. (4.15) and (4.16), along with the optimized value for f_s and the constant values for ν_s and E_{br}, into the theoretical equation derived for calculating the friction between the braided strands in Eq. (4.14). By adding or subtracting the friction term from the total amount of force calculated previously as given in Eq. (4.13), one can predict the hysteresis force-contraction loops. The resulting theoretical values

calculated for the force are compared to the actual amounts of force produced by the MPAM under each pressure in Fig. (4.21). Results show a great agreement between the theoretical and experimental forces, particularly at higher contractions. The theoretical lines, represented by dashed lines, fall between the hysteresis loops at each pressure, indicating that the force equation overestimates the force during a contraction while underestimating it when the MPAM is being expanded to its initial length. This discrepancy arises from the inability of the force equation to fully account for the resistive force case by frictional loss within the muscle during contraction or the assisting effect of friction during expansion, particularly at lower contraction levels. It is important to note that uncertainties in material properties, simplifications in model assumptions, and variations in experimental conditions can also contribute to these slight deviations between the theoretical and experimental forces.

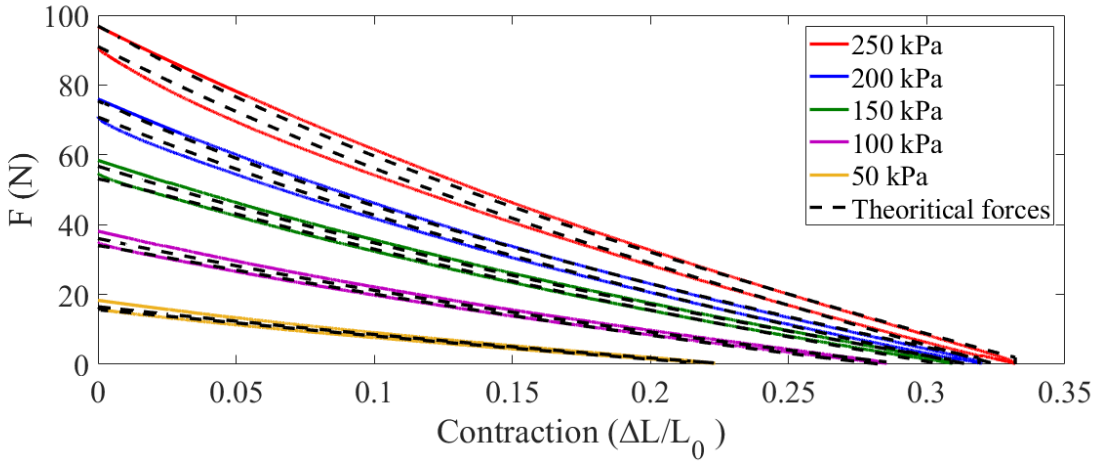

Figure 4.21: Comparison between the theoretical amounts of force obtained from Eq. (4.14) and the experimental forces ($MPAM_1$)

4.6.2.2 Empirical Coulomb Friction Term

An alternative approach to account for the effects of friction between the components of the MPAM on its force output is to derive an empirical friction force, as suggested in Eq. (2.44). While this method may be more straightforward compared to a complex theoretical friction term, it is purely experiment based and can only be performed when the experimental force-contraction data are available. The experimentally driven friction term is obtained by minimizing the error between the theoretical and experimental force values. The standard optimization formulation using the Coulomb friction term defined in Eq. (2.44) is given below:

Substituting $F_f = -K_f(F_{G+t} + F_{NL})sgn(V)$ in Eq. (4.13), find K_f to minimize:

$$\text{Least Sqare Error } = \sum_i (\frac{F_{th} - F_{exp}}{F_{exp}})^2 \ ; \tag{4.17}$$

Subjected to:

$$K_f \geq 0$$

It is worthwhile to note that the value of K_f is dependent on the inlet pressure, and as such, the optimization procedure outlined earlier needs to be repeated for each pressure in order to determine the appropriate values of K_f, as presented in Table (4.10). Fig. (4.22) compares the experimental forces with the theoretical forces obtained using the modified force equation, incorporating the empirical Coulomb friction term. The modified force equation accurately predicts the force generated by the MPAM at each inlet pressure and state of contraction. It is interesting to note that unlike the theoretically derived friction term, the dashed lines representing the predictive forces calculated using the force equation with the empirical friction term fall outside the hysteresis loops, specifically at higher pressures. This suggests that the equation including the empirical friction term underestimates the force during contraction and overestimates it during expansion. These discrepancies arise due to the limitations of the force equation in precisely capturing the resistive or assistive frictional forces. In contrast to the theoretical approach, the empirical Coulomb friction term yields a higher value for the friction force.

Table 4.10: Amounts of K_f at each pressure

	50 kPa	**100 kPa**	**150 kPa**	**200 kPa**	**250 kPa**
K_f	0.0905	0.0702	0.0711	0.0840	0.0778

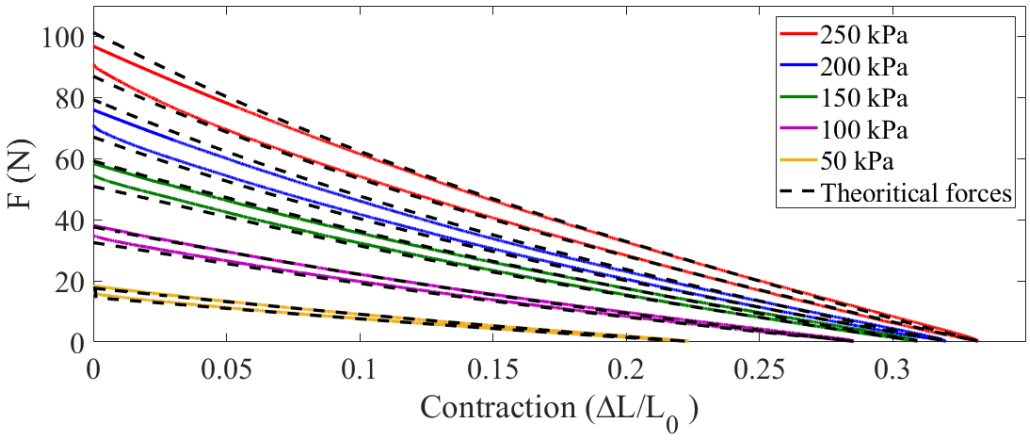

Figure 4.22: Comparison between the Force-Contraction relationship anticipated using the force model including the empirical friction term and the experimental results ($MPAM_1$)

4.6.2.3 Evaluation of the Friction Term for $MPAM_2$

A comparison is performed between the errors obtained from the two theoretical force models, including each friction term, in predicting the force generated by an MPAM. The results, as presented in Table (4.11), indicate that the modified force equation incorporating the theoretical correction term yields more accurate force predictions, exhibiting an average coefficient of determination (R^2) of 99.86% when compared to the experimental data.

Table 4.11: Coefficient of determination for each force equation at various inlet pressures for $MPAM_1$

P (kPa)	R^2 (Modified force with theoretical friction term)	R^2 (Modified force with empirical friction term)
50	0.998924	0.997336
100	0.999702	0.998904
150	0.999762	0.997403
200	0.999068	0.986835
250	0.998908	0.996886

Following the comparison of the two friction calculation methods, it is determined that the first method yields superior accuracy. Consequently, this method is selected to examine the friction in $MPAM_2$ and analyze the resulting hysteresis in its force-contraction loops. Accordingly, Eq. (4.18), which is the modified force equation considering the nonlinearities of the $MPAM_2$ and the friction between its components, is employed to compute the theoretical force as:

$$F = P\pi\left[R^2(2tan^2(\alpha)-1) + (2Rt - t^2) - 2tR(tan^2(\alpha))\right] \tag{4.18}$$
$$+ \pi(2Rt - t^2)\sum_{k=1}^{M} E_k\left(\frac{L}{L_0} - 1\right)^k - \frac{2\pi Rt}{cot^2(\alpha)}\sum_{k=1}^{M} E_k\left(\frac{R}{R_0} - 1\right)^k$$
$$\pm\ Pf_s\ 2\pi R_0 L_0 \frac{cos\alpha_0}{\sqrt{1 - sin^2\alpha_0(1-\gamma)^2}}\left(\frac{1}{1-\gamma}\right)\left(\frac{1}{0.69}\right)\left(\frac{P(1-{\nu_s}^2)}{E_{br}}\right)^{1/3}$$

Fig. (4.23) presents a comparison between the theoretical force calculated using Eq. (4.18) and the experimental force data for the $MPAM_2$. Results show that the theoretical model accurately predicts the experimental force generated by the $MPAM_2$. Furthermore, the lines representing the theoretical force fall within the experimental hysteresis loops, similar to the observations for $MPAM_1$ in Fig. (4.21). However, there is a notable discrepancy between the theoretical and experimental forces at the lowest pressure (50 kPa), which is likely due to the dead-band pressure which has not been accounted for in the theoretical force model, leading to inaccurate predictions at lower pressures. As discussed in the previous section, $MPAM_2$ exhibits a higher dead-band pressure compared to $MPAM_1$, thus generating initial force at a higher starting pressure. It is noted that as the pressure increases, the theoretical lines gradually approach the experimental forces. Additionally, at higher contractions, the theoretical and experimental lines closely align, demonstrating the high accuracy of the modified force equation in predicting the behaviour of an MPAM at higher pressures and contractions.

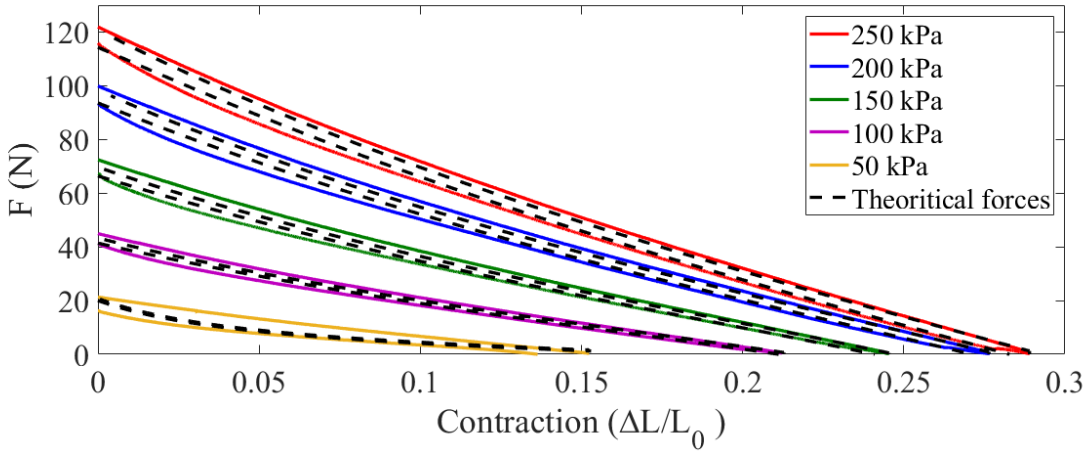

Figure 4.23: Theoretical and experimental values of the force vs. contraction for $MPAM_2$

4.7 Performance of the Proposed MPAMs

Table (4.12) presents a comprehensive comparison of the specifications and outputs between the proposed optimally designed MPAMs in the present research and previously designed and commercialized MPAMs. The results indicate that the optimized MPAMs, with their refined dimensions, are capable of generating significantly higher levels of blocked force compared with other MPAMs of similar size. In some cases, the proposed MPAMs produce twice as much blocked force as the other MPAMs with comparable dimensions. For example, $MPAM_1$ and $MPAM_2$ generate blocked forces that are respectively 14.2% and 23.8% greater than the force output of the commercially available MPAM from Festo® with the same bladder diameter. It is important to note that the developed MPAMs can theoretically produce a maximum blocked force of 238 N at an inlet pressure of 600 kPa, which is substantially higher than the maximum force output achieved by the existing MPAMs. These findings provide strong evidence of the success of the optimization procedure in maximizing the blocked force generated by an MPAM. Interestingly, although maximizing free contraction was not the primary objective of the optimization analysis, the developed MPAMs exhibit higher free contractions compared to most previous MPAMs. The optimized actuators achieve approximately 19%-23% greater free contraction than the MPAM from Festo®. This indicates that, in addition to higher force outputs, the proposed MPAMs, fabricated using cost-effective materials available in the market, are capable of producing large

displacements while maintaining a compact size suitable for a wide range of miniaturized robotic applications.

Additionally, the correction terms obtained from the hysteresis tests conducted on the fabricated samples have resulted in a modified force equation (Eq. (4.18)) for the MPAMs. This modified equation accurately predicts the force and contraction outputs of the actuators with a high degree of accuracy (nearly 99.8%). The modified force equation incorporates a correction term to account for the nonlinearities of the actuator, which needs to be determined specifically for each sample based on the moduli of elasticity of the MPAM and the material used for its fabrication, in addition to a friction term.

Table 4.12: Comparison between the performance of different MPAMs at P=300 kPa

Reference	**D (mm)**	**t (mm)**	**L (mm)**	**Materials**	**Blocked Force (N)**	**Free Contraction (%)**
[39]	9.525	1.587	152	Silicone rubber bladder, PET braid	40	4.6%
[38]	4.6	0.4	43.9	V330 elastomer bladder, PET braid	71	26.8 %
[2]	3	0.5	39.16	Silicone bladder; PET braid	60	44%
[36]	10	1.6	270	Latex bladder; PET braid	100	15%
Festo	6	---	30	---	105	10%
Present work ($MPAM_1$)	6	0.7	50	Ecoflex-50 bladder, PET braid	120	33.2%
Present work ($MPAM_2$)	6	0.7	50	PDMS +Ecoflex-30 bladder, PET braid	130	29%

4.8 Summary and Conclusion

This chapter provided a comprehensive overview of the fabrication process for the optimized MPAMs, along with a detailed description of the test setup and experimental procedure conducted during quasi-static tests to measure blocked force and free contraction. The comparison between the experimental results and theoretical data demonstrated the accuracy of the formulation and optimization process, yielding an overall error of less than 10%. Furthermore, the force and contraction outputs of the two MPAM samples, one utilizing a bladder made from Ecoflex-50 and the other incorporating a bladder made from a combination of PDMS and Ecoflex-30, were compared. It was revealed that while both samples exhibited nearly similar force outputs, the second sample displayed a slightly higher blocked force at higher pressures, while the first sample demonstrated significantly higher free contraction. Additionally, the hysteresis force-contraction curves obtained from loading and unloading the samples at various pressures were employed to derive correction terms that account for the nonlinear behaviour of the actuators and also the friction between their components. These correction terms contributed to the development of an enhanced force model capable of accurately anticipating the force and contraction outputs of the MPAM. Finally, we conducted a comparative analysis between the performance of the optimized MPAMs and previously designed MPAMs documented in the literature. The findings revealed that the force and contraction outputs of the proposed MPAMs were substantially higher than their counterparts with similar dimensions, highlighting the superior performance of the optimized MPAMs.

Chapter 5: Contributions, Conclusions, and Future Remarks

5.1 Major Contributions

The primary objective of this research thesis was to address the existing gap in the literature on the design optimization of miniaturized pneumatic artificial muscles (MPAMs) by maximizing their force output while maintaining their compact dimensions. To accomplish this, a formal optimization problem was formulated incorporating a simple blocked force model. The force model for MPAMs was further enhanced by integrating multiple correction terms, obtained from hysteresis curves, into the fundamental force equation. The major contributions of this thesis are summarized below:

I. Development of a formal optimization formulation for maximizing the force output of an MPAM while considering geometrical constraints and an accurate objective function that incorporates all key parameters affecting the force output of an MPAM.

II. Formulation of two distinct cases of optimization formulations: one including a correction term for the energy stored in the braided sleeving, and the other neglecting it, enabling the investigation of the significance of the braid term in enhancing the accuracy of the blocked force equation and optimization of MPAM outputs.

III. Design and fabrication of MPAMs with optimized parameters, resulting in notably superior force and free contraction compared to previously designed MPAMs of the same size and even commercially available MPAMs such as the one from Festo®.

IV. Fabrication of two customized bladders utilizing 3D-printed molds: one employing Ecoflex-50 and the other using PDMS + Ecoflex-30, allowing the study of bladder material effects on the MPAM's behaviour.

V. Establishment of a relationship between inlet pressure and the moduli of elasticity of each sample, enabling the study of their nonlinear behaviour under various pressures without relying on empirical data.

VI. Development of an improved force equation capable of accurately predicting the force generated by an MPAM at each contraction state and under varying pressures, considering the nonlinearities of the MPAM and the friction between its components.

5.2 Major Conclusions

The major conclusions derived from the present thesis are summarized as follows:

I. The comparison between the two optimization cases indicated that including the correction term for energy stored in the braid in the objective function and optimizing the dimensional parameters related to the braid strands did not significantly improve the results. Therefore, it was concluded that this term can be disregarded to achieve a simplified optimized design for the MPAM without requiring customized braided sleeving.

II. Quasi-static tests conducted on the actuators demonstrated that the derived objective function accurately predicted the force output of both MPAMs, exhibiting an overall error of less than 10% for each sample.

III. A comparison between the two MPAM samples revealed that the first sample (MPAM_1), utilizing an Ecoflex-50 bladder, exhibited a lower dead-band pressure, lower blocked force when the pressure was increased from 150 kPa, and significantly higher free contractions (approximately 1.5 times higher) compared to the second sample (MPAM_2) using a bladder made of PDMS + Ecofles-30. Furthermore, comparing the overall errors between simulated and experimental results for both MPAMs indicated that the behaviour of MPAM_1 was better predicted using the derived force equation.

IV. Due to the imperfections in the tubular silicone and limitations of the MTS machine, the maximum pressure was limited to 300 kPa, yielding a maximum blocked force of 120 N and 136 N for MPAM_1 and MPAM_2, respectively. However, the optimized design has the potential to produce a blocked force of nearly 240 N if the inlet pressure is increased to 600 kPa.

V. Comparing the blocked force and free contraction of the fabricated samples with previously designed MPAMs demonstrated that the optimization formulation successfully resulted in an optimized MPAM with maximized blocked force while maintaining compactness.

VI. Comparing various force equations proposed for MPAMs, incorporating various correction terms, revealed that a force equation accounting for the bladder's thickness, actuator's nonlinearities, and friction between the components yielded accurate predictions of the outputs of the MPAM, with almost 99.8% coefficient of determination.

VII. The nonlinear correction term derived from tensile tests conducted on the bladder material of the first MPAM did not significantly improve the force equation. Thus, it was concluded that the polynomial stress-strain relationship should consider the effects of the whole structure of the MPAM to accurately represent the nonlinear behaviour of the MPAMs.

VIII. A comparison of the two actuators demonstrated that $MPAM_1$ could be modelled with a four-degree polynomial stress-strain function, while $MPAM_2$ required a five-degree polynomial to describe its nonlinear behaviour. Additionally, the elastic moduli of $MPAM_1$ showed an almost linear relationship with the inlet pressure, indicating relatively easier predictability of this PAM's behaviour. Conversely, for $MPAM_2$ the elasticity moduli followed a second-order exponential function of the pressure, posing challenges in accurately anticipating its behaviour.

IX. Comparing the accuracy of the empirically and theoretically driven friction terms revealed that the theoretical method more accurately predicted the hysteresis observed in force-contraction loops.

5.3 Future Remarks

Although this research thesis has offered essential guidance for the design optimization and experimental characterization of MPAMs, there remain certain issues that merit further investigation in future studies.

I. Using the enhanced force model and the standard optimization formulation developed in this thesis, future studies could explore additional optimization variables and constraints to further improve the performance of MPAMs.

II. A wider range of materials, considering their mechanical properties, compatibility, and manufacturing feasibility can be investigated for fabricating MPAMs.

III. Although this thesis conducted quasi-static tests and validated the accuracy of the force equation, future work can expand experimental validation to dynamic scenarios and real-world applications. This may involve performing experiments under varying operating conditions, exploring different loading profiles, or investigating the MPAM's response in more complex environments.

IV. Future research can focus on developing robust control algorithms to precisely manipulate MPAMs for tasks requiring force modulation, trajectory tracking, or cooperative manipulations. Furthermore, investigating practical applications, such as robotic systems, prosthetics, or assistive devices, can provide valuable insights into the real-world implementation of the designed actuator.

V. The behaviour and performance of MPAMs in multi-actuator systems could be explored, which could involve studying interactions and coordination between multiple MPAMs.

References

[1] Davis, S; Tsagarakis, N; Canderle, J; and Caldwell, D. G. Enhanced Modelling and Performance in Braided Pneumatic Muscle Actuators, The International Journal of Robotics Research, Jul. 2004, vol. 22, No. 3, pp. 213–227, doi:10.1177/027836403128964908.

[2] Hocking, E. G; and Wereley, N. M. Analysis of nonlinear elastic behavior in miniature pneumatic artificial muscles, Smart Material and Structures, Jan. 2013, vol. 22, no. 1, doi: 10.1088/0964-1726/22/1/014016.

[3] Caldwell, D. G; Medrano-Cerda, G. A; and Goodwin, M. Control of Pneumatic Muscle Actuators, IEEE Control Systems, 1995, vol. 15, no. 1, pp. 40–48, doi:10.1109/37.341863.

[4] Kalita, B; Leonessa, A; and Dwivedy, S. K. A Review on the Development of Pneumatic Artificial Muscle Actuators: Force Model and Application, Actuators, Oct. 01, 2022, vol. 11, no. 10. MDPI, doi: 10.3390/act11100288.

[5] Pierce, R. C. Expansible Cover, United States Patent 2041950, 26 May, 1936.

[6] Pierce, R. C. Expansible Cover, United States Patent 2211478, 13 August, 1940.

[7] De Haven, H. Tensioning Device for Producing a Linear Pull. United States Patent 248308827, September 1949.

[8] Galyord, R. H. Fluid Actuated Motor System and Stroking Device. United States Patent 284412622, July 1958.

[9] Schulte, H. F. The characteristics of the McKibben artificial muscle, In Application of External Power in Prosthetics and Orthetics, 1962, pp. 94-115.

[10] McKibben, J.L. Artificial Muscle, 1957. Available online: (https://cyberneticzoo.com/). [Accessed: 22, Dec, 2022]

[11] T. Takagi, Pneumatic Actuator for Manipulator. United States Patent, 46152607, October 1986.

[12] Bergemann, D; Lorenz, B; and Thallemer, A. Festo AG & Co., United States Patent, 6349746 B1, 26 February, 2002.

[13] Mižáková, J; Pitel, J; and Tóthová, M. Pneumatic artificial muscle as actuator in mechatronic system, Applied Mechanics and Materials, vol. 460, pp. 81–90, 2014, doi: 10.4028/www.scientific.net/AMM.460.81.

[14] Wang, Y and Xu, Q. Design and testing of a soft parallel robot based on pneumatic artificial muscles for wrist rehabilitation, Scientific Reports, Dec. 2021, vol. 11, no. 1, doi: 10.1038/s41598-020-80411-0.

[15] Zhong, J. U. N; Zhao, D. He, C; Zhu, Y. U. E; and Zhang, Q. A Rehabilitation Robot Driven By Pneumatic Artificial Muscles, Journal of Mechanics in Medicine and Biology, Nov. 2020, vol. 20, no. 9, doi: 10.1142/S0219519420400084.

[16] Magnetti Gisolo, S; Muscolo, G. G; Paterna, M; De Benedictis, C; and Ferraresi, C. Feasibility study of a passive pneumatic exoskeleton for upper limbs based on a mckibben artificial muscle, in Mechanisms and Machine Science, Springer Science and Business Media B.V., 2021, pp. 208–217. doi: 10.1007/978-3-030-75259-0_23.

[17] Kalita, B; and Dwivedy, S. K. Nonlinear dynamic response of pneumatic artificial muscle: A theoretical and experimental study, International Journal of Nonlinear Mechanics, Oct. 2020, vol. 125, doi: 10.1016/j.ijnonlinmec.2020.103544.

[18] Choi, H. S; Lee, C. H; and Baek, Y. S. Design and Validation of a Two-Degree-of-Freedom Powered Ankle-Foot Orthosis with Two Pneumatic Artificial Muscles, *Mechatronics*, Dec. 2020, vol. 72, doi: 10.1016/j.mechatronics.2020.102469.

[19] Tjahyono, A. P; Aw, K. C; Devaraj, H; Surendra, W; Haemmerle, E; and Travas-Sejdic, J. A five-fingered hand exoskeleton driven by pneumatic artificial muscles with novel polypyrrole sensors, Industrial Robot, 2013, vol. 40, no. 3, pp. 251–260, doi: 10.1108/01439911311309951.

[20] Chakravarthy, S; Aditya, K; and Ghosal, A. Experimental characterization and control of miniaturized pneumatic artificial muscle, Journal of Medical Devices, Transactions of the ASME, 2014, vol. 8, no. 4, doi: 10.1115/1.4028420.

[21] De Volder, M; Moers, A. J. M; and Reynaerts, D. Fabrication and control of miniature McKibben actuators, Sensors and Actuators: A Physical, 2011, vol. 166, no. 1, pp. 111–116, doi: https://doi.org/10.1016/j.sna.2011.01.002.

[22] Ashwin, K.P; Jose, D; and Ghosal, A. Modeling and analysis of a flexible end-effector for actuating endoscopic catheters, Mar. 2015. doi: 10.6567/IFToMM.14TH.WC.OS13.029.

[23] Li, H; Kawashima, K; Tadano, K; Ganguly, S; and Nakano, S. Achieving Haptic Perception in Forceps' Manipulator Using Pneumatic Artificial Muscle, IEEE/ASME Transactions on Mechatronics, 2013, vol. 18, no. 1, pp. 74–85, doi:10.1109/TMECH.2011.2163415.

[24] Davis, S; and Caldwell, D. G; Braid effects on contractile range and friction Modeling in pneumatic muscle actuators, International Journal of Robotics Research, Apr. 2006, vol. 25, no. 4, pp. 359–369, doi: 10.1177/0278364906063227.

[25] Ashwin, K. P; and Ghosal, A. A Survey on Static Modeling of Miniaturized Pneumatic Artificial Muscles with New Model and Experimental Results, Applied Mechanics Reviews, Oct 2018, vol. 70, no. 4, doi: 10.1115/1.4041660.

[26] Tondu, B; Ippolito, S; Guiochet, J; and Daidie, A. A Seven-degrees-of-freedom robot-arm driven by pneumatic artificial muscles for humanoid robots, International Journal of Robotics Research, Apr. 2005, vol. 24, no. 4, pp. 257–274, doi: 10.1177/0278364905052437.

[27] Inoue, K. Rubbertuators and applications for robots, Proceedings of the 4th International Symposium on Robotics Research, Cambridge, MA, pp. 215-222, 1988.

[28] Fluidic Muscle DMSP, Festo, Available Online: www.festo.com. [Accessed: July 12, 2022].

[29] Le, H. M; Do, T. N; and Phee, S. J. A survey on actuators-driven surgical robots, Sensors and Actuators: A Phys, 2016, vol. 247, pp. 323–354, doi:https://doi.org/10.1016/j.sna.2016.06.010.

[30] Moers, A; De Volder, M; Reynaerts, D. Integrated high pressure microhydraulic actuation and control for surgical instruments, Biomedical Microdevices, 2012, vol. 13, no. 4, pp. 699-708, doi: 10.1007/s10544-012-9650-y.

[31] Noritsugu, T; and Tanaka, T. Application of rubber artificial muscle manipulator as a rehabilitation robot, IEEE/ASME Transactions on Mechatronics, 1997, vol. 2, no. 4, pp. 259–267, doi: 10.1109/3516.653050.

[32] Jamwal, P. K; Xie, S. Q; Hussain, S; and Parsons, J. G. An Adaptive Wearable Parallel Robot for the Treatment of Ankle Injuries, IEEE/ASME Transactions on Mechatronics, 2014, vol. 19, no. 1, pp. 64–75, 2014, doi: 10.1109/TMECH.2012.2219065.

[33] Gentry, M. F; and Wereley, N. M. Effects of Braid Angle on Pneumatic Artificial Muscle Actuator Performance, 2008. Available Online: https://proceedings.asmedigitalcollection.asme.org

[34] Davis, S; Canderle, J; Artrit, P; Tsagarakis, N; and Caldwell, D. G. Enhanced dynamic performance in pneumatic muscle actuators, in Proceedings 2002 IEEE International Conference on Robotics and Automation (Cat. No.02CH37292), 2002, pp. 2836–2841 vol.3. doi: 10.1109/ROBOT.2002.1013662.

[35] Garbulinski, J; Balasankula, S. C; and Wereley, N. M. Characterization and analysis of extensile fluidic artificial muscles, Actuators, Feb. 2021, vol. 10, no. 2, pp. 1–26, doi:10.3390/act10020026.

[36] Pillsbury, T. E; Wereley, N. M; and Guan, Q. Comparison of contractile and extensile pneumatic artificial muscles, Smart Materials and Structures, Aug 2017, vol. 26, no. 9, doi: 10.1088/1361-665X/aa7257.

[37] Skeletal Muscle Contraction, Lecturio, Available Online: https://app.lecturio.com/#/article/3898?return=%23%2Fwelcome%3Ffv%3D1, [Accessed: 17 February 2023].

[38] Wang, G.N; Wereley, M; and Pillsbury, T. Non-linear quasi-static model of pneumatic artificial muscle actuators, Journal of Intelligent Material Systems and Structures, Mar. 2015, vol. 26, no. 5, pp. 541–553, doi: 10.1177/1045389X14533430.

[39] Kothera, C. S; Jangid, M; Sirohi, J; and Wereley, N. M. Experimental characterization and static Modeling of McKibben actuators, Journal of Mechanical Design, Transactions of the ASME, Sep. 2009, vol. 131, no. 9, pp. 0910101–09101010, doi: 10.1115/1.3158982.

[40] Li, X. A; Sun, K; Guo, C; Liu, T; and Liu, H. Enhanced static modeling of commercial pneumatic artificial muscles, Assembly Automation, May 2020, vol. 40, no. 3, pp. 407–417, doi: 10.1108/AA-04-2019-0060.

[41] Chou, C.P; and Hannaford, B; Measurement and modeling of McKibben pneumatic artificial muscles, IEEE Transactions on Robotics and Automation, 1996, vol. 12, no. 1, pp. 90–102, doi: 10.1109/70.481753.

[42] Ganguly, S; Garg, A; Pasricha, A; and Dwivedy, S. K. Control of pneumatic artificial muscle system through experimental modelling, Mechatronics, 2012, vol. 22, no. 8, pp. 1135–1147, doi: https://doi.org/10.1016/j.mechatronics.2012.09.010.

[43] Park, Y. L; and Wood, R. J. Smart pneumatic artificial muscle actuator with embedded microfluidic sensing, in Proceedings of IEEE Sensors, IEEE Computer Society, 2013. doi: 10.1109/ICSENS.2013.6688298.

[44] Wakimoto, S; Misumi, J; and Suzumori, K. New concept and fundamental experiments of a smart pneumatic artificial muscle with a conductive fiber, Sensors and Actuators: A Physical, Oct. 2016, vol. 250, pp. 48–54, doi: 10.1016/j.sna.2016.08.004.

[45] Kanno, R; Watanabe, S; Shimizu, K; and Shintake, J. Self-Sensing McKibben Artificial Muscles Embedded with Dielectric Elastomer Sensor, IEEE Robotics Automation Letter, Oct. 2021, vol. 6, no. 4, pp. 6274–6280, doi: 10.1109/LRA.2021.3093276.

[46] Fu, C; Wang, K; Tang, W; Nilghaz, A; Hurren, Ch; Wang, X; Xu, W; Su, B; Xia, Zh; Multi-sensorized pneumatic artificial muscle yarns, Chemical Engineering Journal, Oct. 2022, vol. 446, doi: 10.1016/j.cej.2022.137241

[47] Do Rosario Carvalho, A. D; Karanth P, N; and Desai, V. Design and characterization of a pneumatic muscle actuator with novel end-fittings for medical assistive applications, Sensors and Actuators A: Physical, Nov. 2021, vol. 331, doi: 10.1016/j.sna.2021.112877.

[48] Lathrop, B; Ourak, M; and Poorten, E.V. Miniature Pneumatic Artificial Muscles for Use in Surgical Devices, ACTUATOR, *International Conference and Exhibition on New Actuator Systems and Applications*, 2022.

[49] Markus, A.T; Sobczyk, M.R; and Perondi, E.A. Modeling, Control, and Simulation of a 3-Degree of Freedom Mechanism Actuated by Pneumatic Artificial Muscles for Upper Limb Prosthesis Application, *Journal of Mechanisms and Robotics*, Feb. 2022, vol. 15.

[50] Ashwin, K.P; and Ghosal, A. Static Modeling of Miniaturized Pneumatic Artificial Muscles, Kinematic Analysis, and Experiments on an Endoscopic End-Effector, *IEEE/ASME Transactions on mechatronics*, Aug. 2019, vol. 24.

[51] Tadano, K; Akai, M; Kadota, K; and Kawashima, K. Development of grip amplified glove using bi-articular mechanism with pneumatic artificial rubber muscle, in Proceedings - IEEE International Conference on Robotics and Automation, 2010, pp. 2363–2368. doi: 10.1109/ROBOT.2010.5509393.

[52] Vashisth, A; Zhu, B; Wimmer, B. M; Bakis, C. E; and Rahn, C. D. Evaluation of Millimeter-Size Fluidic Flexible Matrix Composite Tubes, 2013. Available online: (http://asmedigitalcollection.asme.org/SMASIS/proceedings-pdf/SMASIS2013/56048/V002T06A029/4459446/v002t06a029-smasis2013-3344.pdf)

[53] Doumit M; and Leclair, J. Development and testing of stiffness model for pneumatic artificial muscle, International Journal of Mechanical Science, Jan. 2017, vol. 120, pp. 30–41, doi: 10.1016/j.ijmecsci.2016.11.015.

[54] Salahuddin, B; Warren, H; and Spinks, G. M. A comprehensive test method for measuring actuation performance of McKibben artificial muscles, Smart Materials and Structures, Apr. 2021, vol. 30, no. 4, doi: 10.1088/1361-665X/abea01.

[55] Pillsbury, T. E; Kothera, C. S; and Wereley, N. M. Effect of bladder wall thickness on miniature pneumatic artificial muscle performance, Bioinspiration & Biomimetics, Sep. 2015, vol. 10, no. 5, doi: 10.1088/1748-3190/10/5/055006.

[56] Joe, S; Totaro, M; Wang, H; and Beccai, L. Development of the ultralight hybrid pneumatic artificial muscle: Modelling and optimization, PLoS One, Apr 2021, vol. 16, no. 4 doi: 10.1371/journal.pone.0250325.

[57] Sangian, D; Naficy, S; Spinks, G. M; and Tondu, B. The effect of geometry and material properties on the performance of a small hydraulic McKibben muscle system, Sensors and Actuators A: Physical, Oct. 2015, vol. 234, pp. 150–157, doi: 10.1016/j.sna.2015.08.025.

[58] Solano, B; and Rotinat-Libersa, C. Compact and lightweight hydraulic actuation system for high performance millimeter scale robotic applications: Modeling and experiments, Journal of Intelligent Material Systems and Structures, Sep. 2011, vol. 22, no. 13, pp. 1479–1487. doi: 10.1177/1045389X11418860.

[59] Yang, H. D; Greczek, B. T; and Asbeck, A. T. Modeling and analysis of a high-displacement pneumatic artificial muscle with integrated sensing, Frontiers Robotics AI, Jan. 2019, vol. 6, doi: 10.3389/frobt.2018.00136.

[60] Tomori, H; Sato, Y; Ando, Sh. Cyclic Failure Testing of Straight-Fiber Pneumatic Artificial Muscles for Optimizing Durability, in Proceedings of IECON 2019-45th Annual Conference of the IEEE Industrial Electronics Society : Convention Center, Lisbon, Portugal, 14-17 October, 2019.

[61] Xiao, W; Hu, D; Chen, W; Yang, G; and Han, X. Design, Characterization and Optimization of Multi-directional Bending Pneumatic Artificial Muscles, Journal of Bionic Engineering, Nov. 2021, vol. 18, no. 6, pp. 1358–1368, doi: 10.1007/s42235-021-00077-w.

[62] Diteesawat, R. S; Helps, T; Taghavi, M; and Rossiter, J. Characteristic Analysis and Design Optimization of Bubble Artificial Muscles, Soft Robotics, Apr. 2021, vol. 8, no. 2, pp. 186–199, doi: 10.1089/soro.2019.0157.

[63] Lathrop, R; Ourak, M; Deprest, J; and Poorten, E.V. Concentric Dual-Chamber Pneumatic Artificial Muscles: Miniature Actuators Designed for Use in Minimally Invasive Surgical Instruments, *Journal of Medical Robotics Research*, 2022, vol. 7, nos. 2 & 3, doi: 10.1142/S2424905X22410070.

[64] Kwon, J; and Yoon, S. J; and Park, Y.L. Flat Inflatable Artificial Muscles with Large Stroke and Adjustable Force-Length Relations, *IEEE Transactions on Robotics*, Jun. 2020, vol. 36, no.3.

[65] Kim, W; Park, H; and Kim, J. Compact Flat Fabric Pneumatic Artificial Muscle (ffPAM) for Soft Wearable Robotic Devices, *IEEE Robotics and Automation Letters*, Apr. 2021, vol. 6, no. 2.

[66] Faudzi, A. A. M; Endo, G; Kurumaya, S; and Suzumori, K; Long-Legged Hexapod Giacometti Robot Using Thin Soft McKibben Actuator, IEEE Robotics and Automation Letter, Jan. 2018, vol. 3, no. 1, pp. 100–107, doi: 10.1109/LRA.2017.2734244.

[67] Kurumaya, S; Suzumori, K; Nabae, H; and Wakimoto, S. Musculoskeletal lower-limb robot driven by multifilament muscles, ROBOMECH Journal, Dec. 2016, vol. 3, no. 1, doi: 10.1186/s40648-016-0061-3.

[68] Schulte, Jr, H. F; Adamski, D.F; Pearson, J.R. Characteristics of the Braided Fluid Actuator, The University of Michigan, Department of Physical Medicine and Rehabilitation Orthetics Research Project, Technical Report No. 5, Nov. 1961.

[69] Ping Chou, Ch; and Hannaford, B. Static and dynamic characteristics of McKibben pneumatic artificial muscles, Proceedings of the 1994 IEEE International Conference on Robotics and Automation, San Diego, CA, USA, 1994, pp. 281-286 vol.1, doi: 10.1109/ROBOT.1994.350977.

[70] Ferraresi, C; Franco, W; and Bertetto, A. M. Flexible Pneumatic Actuators: A Comparison between The McKibben and the Straight Fibres Muscles, Journal of Robotics and Mechatronics, Feb. 2001, vol. 13, no. 1, pp. 56–63, doi: 10.20965/jrm.2001.p0056.

[71] Tondu, B. Modeling and Control of McKibben Artificial Muscle Robot Actuators, IEEE Control Systems, May. 2000, vol. 20, no. 2, pp. 15-38, doi: 10.1109/37.833638.

[72] Woods, B. K. S; Kothera, C. S; and Wereley, N. M. Wind tunnel testing of a helicopter rotor trailing edge flap actuated via Pneumatic Artificial Muscles, Journal of Intelligent Material Systems and Structures, Sep. 2011, vol. 22, no. 13, pp. 1513–1528. doi: 10.1177/1045389X11424216.

[73] Tondu, B. Modelling of the McKibben artificial muscle: A review, Journal of Intelligent Material Systems and Structures, Feb. 2012, vol. 23, no. 3, pp. 225–253, doi: 10.1177/1045389X11435435.

[74] Ball, E; and Garcia, E. Effects of bladder geometry in pneumatic artificial muscles, Journal of Medical Devices, Transactions of the ASME, Dec. 2016, vol. 10, no. 4, doi: 10.1115/1.4033325.

[75] Wang, Q.J; and Zhu, D. Hertz Theory: Contact of Spherical Surfaces. In Encyclopedia of Tribology, Springer, Boston, MA, 2013, https://doi.org/10.1007/978-0-387-92897-5_492.

[76] Tu, Q; Wang, Y; Yue, D; and Dwomoh, F. A. Analysis on the Impact Factors for the Pulling Force of the McKibben Pneumatic Artificial Muscle by a FEM Model, Journal of Robotics, 2020, vol. 2020, doi: 10.1155/2020/4681796.

[77] Arora, J.S. Introduction to Optimum Design, Elsevier, fourth edition, 2017, doi:https://doi.org/10.1016/C2013-0-15344-5.

[78] Ecoflex series, Smooth-on, Available Online: https://www.smoothon.com/products/ecoflex-00-30/, [Accessed: 22 May, 2023].

[79] Kumar, V; Pallapa, M; Rezai, P; Selvagnapathy, P.R. Polymers, Materials Science and Material Engineering, Elsevier, doi:https://doi.org/10.1016/B978-0-12-803581-8.00522-1.